UC San Diego

UC San Diego Electronic Theses and Dissertations

Title

Microstructurally Controlled Composites with Optimal Elastodynamic Properties

Permalink

https://escholarship.org/uc/item/9gw5w8tq

Author

Sadeghi, Hossein

Publication Date

2016

Peer reviewed|Thesis/dissertation

eScholarship.org Powered by the California Digital Library
University of California

UNIVERSITY OF CALIFORNIA, SAN DIEGO

Microstructurally Controlled Composites with Optimal Elastodynamic Properties

A Dissertation submitted in partial satisfaction of the requirements for the degree of

Doctor of Philosophy

in

Engineering Sciences (Applied Mechanics)

by

Hossein Sadeghi

Committee in charge:

Professor Sia Nemat-Nasser, Chair
Professor Hyonny Kim
Professor Francesco Lanza Di Scalea
Professor Xanthippi Markenscoff
Professor Vitali F. Nesterenko

2016

Copyright ©

Hossein Sadeghi, 2016

All rights reserved.

The Dissertation of Hossein Sadeghi is approved, and it is acceptable in quality and form for publication on microfilm and electronically:

_____

_____

_____

_____

_____

Chair

University of California, San Diego

2016

Dedication

To my family.

To all who supported me through my life.

Table of Contents

List of Figures

List of Tables

Acknowledgements

I would like to express my deepest appreciation to my advisor, Professor Sia Nemat-Nasser, for his great support and inspiration. Without his astute advice and invaluable guidance this work would not have been possible. I am also grateful to Dr. Ankit Srivastava, Dr. Alireza V. Amirkhizi, and Dr. Kristin Holzworth for their collaboration and advice. I would also like to thank Mr. Jon Isaac, whose experience and insight into experimental methods was a great help in conducting my experiments. I'm also thankful to Mrs. Lauri Jacobs-Cohantz for her help during my study at UCSD's Center of Excellence for Advanced Materials (CEAM).

Chapter 4, in part, is reprint of the material as it appears in "Phononic layered composites for stress-wave attenuation", Mechanics Research Communication, 2015, S. Nemat-Nasser, H. Sadeghi, A.V. Amirkhizi, and A. Srivastava, published by Elsevier. The dissertation author was the primary investigator of this paper.

I would like to acknowledge that this work has been supported by DARPA Grant RDECOM W91CRB-10-1-0006 to the University of California, San Diego.

VITA

2008 Bachelor of Science in Mechanical Engineering, Sharif University of Technology, Tehran, Iran

2010 Master of Science in Mechanical Engineering, Sharif University of Technology, Tehran, Iran

2016 Doctor of Philosophy in Engineering Sciences (Applied Mechanics), University of California, San Diego

PUBLICATIONS

JOURNALS

S. Nemat-Nasser, H. Sadeghi, A.V. Amirkhizi, A. Srivastava, Phononic layered composites for stress-wave attenuation, Mechanics Research Communication 68, 65-69 (2015)

PROCEEDINGS

H. Sadeghi, S. Nemat-Nasser, Design optimization of layered periodic composites for a desired elastodynamic response, Proceeding of SPIE 9438, 94380T-1 (2015)

H. Sadeghi, S. Nemat-Nasser, Optimal design of periodic layered composites for mitigation of impact-induced shock waves, Proceeding of SEM Annual (2015)

H. Sadeghi, A. Srivastava, S. Nemat-Nasser, Acoustic impedance matching using dynamic homogenization of periodic composites, Proceeding of SPIE 8689, 86891A (2013)

H. Sadeghi, A. Srivastava, S Nemat-Nasser, Non-reflective and highly dissipative acoustic metamaterials, Proceeding of ASME IMECE 62513, V014T15A044 (2013)

H. Sadeghi, A. Srivastava, R. Griswold, S. Nemat-Nasser, Temperature tuning of band-structure of 1-D elastic periodic composites, Proceeding of SPIE 8342, 834220 (2012)

H. Sadeghi, A. Srivastava, R. Griswold, S. Nemat-Nasser, Elastic wave propagation in two dimensional periodic composites, Proceeding of ASME IMECE 64549, 945-946 (2011)

ABSTRACT OF THE DISSERTATION

Microstructurally Controlled Composites with Optimal Elastodynamic Properties

by

Hossein Sadeghi

Doctor of Philosophy in Engineering Sciences (Applied Mechanics)

University of California, San Diego, 2016

Professor Sia Nemat-Nasser, Chair

Periodic composites (PCs) are artificial materials with specially designed microstructure to manage stress waves. The objective of this dissertation is to study various techniques for microstructural design of PCs for a desired elastodynamic response. A mixed variational formulation is studied for band structure calculation of

PCs. Dynamic homogenization is studied for calculation of the frequency dependent effective properties of PCs. Optimization techniques are used together with mixed variational formulation and dynamic homogenization to make a computational platform for microstructural design of PCs. Several PCs are designed and fabricated, and various tests are performed for experimental verification.

First, band-gap in one- and two-dimensional PCs is investigated experimentally. Mixed variational formulation is used to design samples with band-gaps at frequencies convenient to conduct experiment. Samples are fabricated and their transmission coefficient is measured. Experimental data are compared with theoretical results for evaluation of the band structure. Also, using constituent materials with temperature dependent material properties, it is shown that band structure of PCs can be tuned by changing the ambient temperature. Furthermore, dynamic homogenization is used to design a one-dimensional PC for acoustic impedance matching. As a result, the reflection of stress waves at the interface of two impedance matched media becomes zero. Samples are fabricated and ultrasound tests are performed to measure the reflection coefficient for experimental verification. In addition, a one-dimensional PC with metamaterial response is designed to achieve a composite with both high stiffness-to-density ratio and high attenuation at low frequency regime. Samples are fabricated and the attenuation coefficient is measured for experimental verification.

Moreover, optimal design of PCs for shock wave mitigation is investigated. A genetic algorithm is used to design the microstructure of a one-dimensional PC for maximum band-gap bandwidth. To verify the theoretical calculation, samples are fabricated and Hopkinson bar experiments are performed. In addition, negative refraction

in two-dimensional PCs is investigated. Equifrequency surfaces of a two-dimensional PC are calculated together with vectors of group velocity. Dynamic homogenization is used to find overall elastodynamic properties of the two-dimensional PC. Energy refraction at the interface of a homogenous half-space and the two-dimensional PC is studied.

Chapter 1

Introduction

Periodic composites (PCs) are artificial materials with specially designed microstructure to control stress waves. PCs exhibit band-gaps, where propagation of stress waves is prohibited. This feature can be used to design acoustic filters, noise insulators, and vibrationless environments. In addition, through microstructural design, PCs can demonstrate metamaterial behavior, i.e. negative effective density and/or negative effective stiffness, at certain frequency ranges [1, 2, 3]. Such features make PCs strong candidates for design of structures with extraordinary elastic and dynamic response. The objective of this dissertation is to study various techniques for microstructural design of PCs for a desired elastodynamic response. A mixed variational formulation is studied to calculate the band structure of one-, two-, and three-dimensional PCs. In addition, dynamic homogenization is studied for calculation of the frequency dependent effective material properties of PCs. Optimization techniques are used together with mixed variational formulation and dynamic homogenization to make a computational platform for microstructural design of PCs. Several PCs are designed for (i) stress waves filtering, (ii) acoustic impedance matching, (iii) maximizing the

attenuation, and (iv) shock wave mitigation. Samples are fabricated and various tests are performed for experimental verification of the computational platform.

1.1. Band-gap

Propagation of stress waves in PCs is prohibited within band-gaps, where incoming stress waves get effectively reflected. The first study on analysis of stress wave propagation in PCs is done by Rytov [4]. He developed an analytical solution for band structure calculation of one-dimensional periodic composites. Applying the Bloch boundary conditions, he derived the dispersion equation and showed that in certain frequency ranges the propagation of the stress waves is forbidden. A mixed variational method, originally developed by Nemat-Nasser [5], was developed in 1970's for analysis of stress wave propagation in PCs [6, 7, 8, 9, 10, 11]. Using this method, band structure of one-, two-, and three-dimensional periodic elastic composites was calculated with high accuracy. The power of this method is due to independent variation of displacements and stresses within the composite. As a result, the continuity of tractions and displacements at the interface of the matrix and inhomogeneities are satisfied automatically. For illustration, they studied waves propagating normal to the layers in one-dimensional PCs and normal to the fibers in fiber reinforced composites [8]. Nemat-Nasser and Minagawa [8] presented explicit formulation for calculation of eigenfrequencies and eigenfunctions of three-dimensional periodic composites with cuboidal and ellipsoidal inclusions. They showed that mixed variational method is more accurate and faster than Rayleigh quotient in predicting the band structure.

Kushwaha et al. [12, 13] developed plane wave expansion (PWE) method for band structure calculation of PCs. In this method, the displacement is replaced by its Fourier series expansion which satisfies the Bloch boundary conditions. Due to periodicity, the density, and longitudinal and shear wave speeds in the composite are represented by their Fourier series expansions as well. Substituting the displacement and material properties with their Fourier series expansion, the equation of motion is reduced to an eigenvalue problem which can be solved to find the band structure. Vasseur et al. [14] used PWE to calculate the band structure of two-dimensional periodic arrays of solid cylindrical inclusions in a solid matrix. In order to verify the theoretical calculations, they presented experimental transmission results through a finite slab of the periodic composite. They showed that the experimentally observed band-gaps match the theoretical predictions. Although PWE has been used successfully in predicting band structure of PCs in several cases, it has convergence problem when dealing with systems of either very high or very low filling ratios, or of large elastic mismatch [15].

Multiple scattering technique (MST) was developed for band structure calculation of PCs to overcome the limitations of PWE method [16, 17, 15]. In this method, the displacements in each inhomogeneity (scatterer) are considered to be the summation of displacements of (1) the incoming waves from all the other scatterers and (2) the outgoing (scattered) waves. Applying the continuity of the displacements and tractions at the interface of each scatterer and the matrix, a relation between the coefficients of incoming and outgoing waves for each scatterer is found. Imposing the Bloch boundary conditions, the equations reduce to an eigenvalue problem which can be solved for eigenmodes and eigenfunctions. Kafesaki and Economou [16] presented multiple

scattering formulations for wave propagation in three-dimensional periodic composites. They considered acoustic wave propagation in a periodic composite consisting of solid spheres in a fluid host and calculated the dispersion curve and showed that PWE method can not describe the composites with fluid matrix accurately. Mei et al. [15] presented MST for elastic wave propagation in two-dimensional PCs. They calculated the band structure for two-dimensional PCs with cylindrical solid inclusion in fluid matrix and studied the convergence of the solution. They also observed that PWE can not describe the response of PCs with fluid matrix accurately. Ke et al. [18] used MST to calculate the equifrequency surface (EFS) of a two-dimensional PC made of triangular arrays of rods in a liquid host. Using EFS they predicted negative refraction for all angles of incident acoustic waves over the second mode. To demonstrate the negative refraction behavior, they measured wave propagation through a finite slab of PC and verified their theoretical through experiment.

1.2. Metamaterials

Acoustic/elastic metamaterials are specially designed PCs with overall negative elastodynamic properties [1, 2, 3, 19]. Such extraordinary features are due to local resonance inside the composite at certain frequencies. Liu et al. [1] designed a three-dimensional metamaterial and showed that near the resonance frequencies, the metamaterial behaves like a medium with effective negative stiffness. Their experimental results show that at the resonance frequencies the transmission coefficient is very small due to attenuation induced by local resonance. Li and Chan [2] showed the existence of acoustic metamaterials in which both the effective density and bulk modulus are

simultaneously negative. They realized that double negativity in acoustic metamaterials is a consequence of local resonance. Fang et al. [3] reported a class of ultrasonic metamaterials consisting of an array of subwavelength Helmholtz resonators with designed acoustic inductance and capacitance. These materials have an effective dynamic modulus with negative values near the resonance frequency. They showed experimentally that these metamaterials can convey acoustic waves with a group velocity antiparallel to phase velocity. Fokin et al. [20] developed a method to extract effective material properties from experimentally measured reflection and transmission coefficients. They used this method to analyze various acoustic metamaterials and observed negative effective properties at some frequencies.

Microstructure of acoustic/elastic metamaterials can also be designed to achieve negative energy refraction [21, 22]. Li et al. [23] used the multiple scattering technique and studied the negative refraction imaging in two-dimensional PCs. They showed that localized resonance mechanism brings on a group of flat single-mode bands in low frequency region which provides two equivalent frequency surfaces close to circular. Croenne et al. [24] presented experimental evidence of negative refraction of longitudinal waves in two-dimensional PCs with a solid matrix. They made a PC of triangular arrangements of steel rods embedded in epoxy and carried out an experiment on a prism-shaped PC inside an epoxy block and observed negative refraction experimentally. Nemat-Nasser [25, 26] studied the anti-plane shear wave propagation in one- and two-dimensional PCs using a mixed variational formulation. He showed that negative energy refraction can be accompanied by positive phase-velocity refraction, and positive energy refraction can be accompanied by negative phase-velocity refraction.

The attenuation of stress waves in metamaterials is large near the resonance frequencies. Ho et al. [27] used several locally resonant materials with different resonance frequencies and showed that each layer vibrates like an independent unit. Their results show significant drop in transmission coefficient at resonance frequencies. Cheng et al. [28] designed a one-dimensional ultrasonic metamaterial with both effective density and effective bulk modulus simultaneously negative. They found the transmission coefficient using acoustic transmission line method (ATLM), finite element method, and experimental measurement and observed a substantial drop in transmission spectrum around the resonance frequency. Wang et al. [29] studied the propagation of longitudinal and transverse elastic waves in locally resonance one-dimensional metamaterials. They showed that locally resonant one-dimensional PCs can be designed to show band-gap at frequencies around a few hundreds of Hertz. Nemat-Nasser and Srivastava [30] showed that three-phase, one-dimensional periodic composites with a heavy central layer and compliant coating embedded in a polymer matrix can be designed to show negative effective density and stiffness over the second mode. These studies suggest the possibility of using metamaterials to design structural composites with tunable attenuation.

1.3. Dynamic homogenization

Due to interesting behavior of PCs, there has been growing interest to develop techniques to calculate their overall elastodynamic properties [31, 32, 33, 34, 35, 36, 37]. Willis [38] developed a homogenization method based on an ensemble averaging technique of Bloch reduced form of wave propagation in PCs. He showed that the mean stress is coupled not only to the mean strain, but also to the mean velocity. Likewise, the

mean momentum is coupled not only to the mean velocity, but also to the mean strain. Nasser et al. [39] developed a homogenization method based on integration of field variables to calculate effective dynamic properties for Bloch waves in one-dimensional PCs. They showed that the resulting effective parameters satisfy the overall field equations and yield the exact dispersion relation. Nemat-Nasser and Srivastava [40] presented a homogenization method for one-dimensional composites based on micromechanical considerations. They provided explicit expressions for the effective dynamic properties of one-dimensional PCs and systematically deduced the overall constitutive relations for the homogenized elastic solid. Nemat- Srivastava and Nemat-Nasser [41] developed a method for homogenization of three-dimensional PCs. They provided explicit expressions to calculate the effective elastodynamic parameters for three-dimensional periodic elastic composites. Nemat-Nasser and Srivastava [42] used a dynamic homogenization to study the effective properties of layered metamaterials. They observed that near the resonance frequency both the effective compliance and density become singular and they can achieve negative values, simultaneously. Antonakakis et al. [33] developed an asymptotic based homogenization technique for two-dimensional periodic composites which is valid at high frequencies. They compared their calculations with finite element simulations and observed that the periodic composites can exhibit high anisotropy at certain frequency ranges. Torrent et al. [19] developed a method to calculate the frequency dependent effective properties of two-dimensional periodic composites at low frequency limit. They observed that the effective mass density and stiffness tensor are in general anisotropic, and can become singular and achieve negative values at certain frequency ranges. Due to recent advances in transformational acoustics,

which makes acoustic cloaking achievable [43], dynamic homogenization has become a useful tool for microstructural design of the cloak [44]; which demands further understanding of these techniques.

1.4. Organization of chapters

The manuscript is organized in the following manner. In chapter 2, theoretical framework for analysis of stress wave propagation in PCs is studied. A mixed variational method is studied for calculation of band structure of one-, two-, and three-dimensional PCs. A dynamic homogenization is studied which allows for evaluation of effective elastodynamic properties of PCs. In addition, transfer matrix method is considered to find the exact solution for reflection and transmission coefficients at the interfaces of a one-dimensional PC sandwiched by two homogenous half-spaces.

In chapter 3, band-gap in one-dimensional and two-dimensional PCs is investigated experimentally. Mixed variational formulation is used to design samples with band-gaps at frequencies convenient to conduct experiment. Samples are fabricated and their transmission coefficient is measured for verification of the theoretical band structure. In addition, tuning the band structure of periodic composites with change in ambient temperature is studied. A one-dimensional PC with constituent materials which have temperature dependent material properties is fabricated. Ultrasound measurements are performed at different temperatures and transmission coefficient are measured and compared with theoretical results for verification.

In chapter 4, dynamic homogenization is used for microstructural design of one-dimensional PCs for acoustic impedance matching. As a result, the reflection of stress waves at the interface of the two impedance matched media becomes zero. Ultrasonic measurements and finite element simulation are performed to find the reflection coefficient for verification. Furthermore, a one-dimensional metamaterial is designed for stress wave attenuation in sonic range of frequency. The aim is to design the microstructure of the metamaterial to achieve both high attenuation coefficient and high in-plane stiffness-to-density ratio. To verify the theoretical calculation, laboratory samples are fabricated and the attenuation coefficients are measured.

In chapter 5, design optimization of PCs for a desired elastodynamic response is studied. Optimal design of one-, two-, and three-dimensional PCs with maximum band-gap bandwidth is studied. In addition, optimal design of PCs for shock wave mitigation is investigated. To verify the theoretical calculation, samples are fabricated and Hopkinson bar experiments are performed. Furthermore, optimal design of one-dimensional PCs for minimum reflection and maximum attenuation is investigated. Samples are fabricated and ultrasound tests are performed to measure the reflection and attenuation coefficients for evaluation of the theoretical results.

In chapter 6, negative refraction in two-dimensional PCs is investigated. Mixed variational formulation is used to find the equifrequency surfaces of a two-dimensional PC together with vectors of group velocity. Dynamic homogenization is used to calculate frequency-dependent overall elastodynamic properties of the PC. Numerical results are presented and energy refraction at the interface of a homogenous half-space and the PC is studied.

Chapter 2

Stress wave propagation in periodic composites

In this chapter, the theoretical framework for analysis of stress wave propagation in PCs is studied. A mixed variational method is used for band structure calculation of one-, two-, and three-dimensional PCs. Dynamic homogenization is studied for calculation of effective elastodynamic properties of one- and two-dimensional PCs. In addition, transfer matrix method is studied to provide an exact solution for calculating the reflection and transmission coefficients at the interfaces of a one-dimensional composite sandwiched by two homogenous half-spaces.

2.1. Mixed variational method

Mixed variation formulation provides an approximate solution for analysis of stress wave propagation in one-, two-, and three-dimensional PCs [6, 9]. In this method stress and displacement components can vary independently in order to satisfy the

continuity of displacements and tractions at the interfaces of the matrix and inhomogeneities.

2.1.1. One-dimensional periodic composites

Consider wave propagation in a one-dimensional elastic composite made of infinite number of identical repeated unit cells. Figure 2-1, shows a typical unit cell of a two-phase, one-dimensional PC. The periodicity condition can be expressed as

$$\rho(x + m'a) = \rho(x)$$
$$E(x + m'a) = E(x) \tag{2.1}$$

where ρ, E, a, and m' are the density, Young's modulus, unit cell size, and an integer, respectively. The equation of motion can be expressed as

$$\rho(x)\frac{\partial^2}{\partial t^2}u(x,t) = \frac{\partial}{\partial x}\sigma(x,t) \tag{2.2}$$

where σ and u are stress and displacement, respectively. For one-dimensional linear elastic materials the constitutive equation is given by

$$\sigma(x,t) = E(x)\varepsilon(x,t) \tag{2.3}$$

where ε is the strain which can be written as

$$\varepsilon(x,t) = \frac{\partial}{\partial x}u(x,t) \tag{2.4}$$

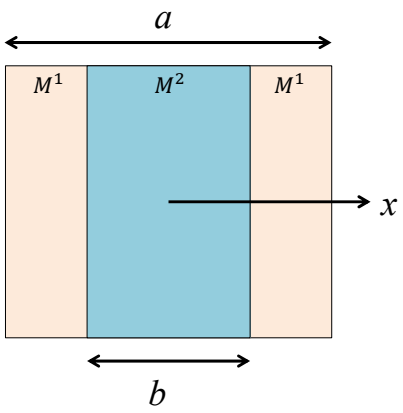

Figure 2-1: Unit cell of a one-dimensional periodic composite

For a periodic medium the solution of equation of motion (2.2) has periodic coefficients which can be expressed as

$$g(x+a) = g(x)e^{iqa} \tag{2.5}$$

where q and g are the overall wave number and any of the field variables, respectively. The Bloch boundary conditions for a unit cell can be expressed as

$$\begin{aligned} u\left(\frac{a}{2}\right) &= u\left(-\frac{a}{2}\right)e^{iqa} \\ \sigma\left(\frac{a}{2}\right) &= \sigma\left(-\frac{a}{2}\right)e^{iqa} \end{aligned} \tag{2.6}$$

It can be shown that the eigenvalues of the problem can be found by rendering the following functional stationary [5]

$$\lambda_N = \frac{\langle \sigma, \partial u/\partial x \rangle + \langle \partial u/\partial x, \sigma \rangle - \langle D\sigma, \sigma \rangle}{\langle \rho u, u \rangle} \tag{2.7}$$

where

$$\langle gu_j, v_j \rangle = \int_{\Omega} g u_j v_j^* d\Omega \tag{2.8}$$

where * denotes the complex conjugate, and $D = 1/E$ is the compliance. Here, the stress and displacement fields are varied independently in the following forms

$$\bar{u} = \sum_{\alpha=-M}^{M} U^{(\alpha)} f^{(\alpha)}(\mathbf{x}) \tag{2.9}$$

$$\bar{\sigma} = \sum_{\alpha=-M}^{M} S^{(\alpha)} f^{(\alpha)}(\mathbf{x}) \tag{2.10}$$

where $f^{(\alpha)} = e^{i(Q+2\alpha\pi)x/a}$, in which $Q = qa$ is the normalized wave number, and $U^{(\alpha)}$ and $S^{(\alpha)}$ are unknown Fourier coefficients. Minimizing the functional in equation (2.7) with respect to unknown coefficients $U^{(\alpha)}$ and $S^{(\alpha)}$, we get the following linear system of equations

$$\langle \frac{\partial \bar{\sigma}}{\partial x} + \lambda_N \rho \bar{u}, f^{(\alpha)} \rangle = 0 \tag{2.11}$$

$$\langle D\bar{\sigma} - \frac{\partial \bar{u}}{\partial x}, f^{(\alpha)} \rangle = 0 \tag{2.12}$$

which can be written in matrix form as

$$\begin{aligned} \boldsymbol{H}^* \boldsymbol{U} + \boldsymbol{\Phi} \boldsymbol{S} &= \mathbf{0} \\ \boldsymbol{\Omega} \boldsymbol{U} + \boldsymbol{H} \boldsymbol{S} &= 0 \end{aligned} \tag{2.13}$$

where the $\boldsymbol{U}$ and $\boldsymbol{S}$ are vectors of unknown coefficients

$$\begin{aligned} \boldsymbol{U} &= \{U_{-N}, U_{-N+1}, \dots, U_0, \dots, U_N\}^T \\ \boldsymbol{S} &= \{S_{-N}, S_{-N+1}, \dots, S_0, \dots, S_N\}^T \end{aligned} \tag{2.14}$$

The explicit form of the coefficient matrices $\boldsymbol{\Omega}$, $\boldsymbol{\Phi}$, and $\boldsymbol{H}$ are given in Appendix 2A. The characteristic equation for linear system of equations (2.13) can be found as

$$\det[\boldsymbol{H}^{*} - \boldsymbol{\Phi}\boldsymbol{H}^{-1}\boldsymbol{\Omega}]=0 \tag{2.15}$$

The solutions of this equation give the eigenfrequencies and eigenvectors of the composite.

2.1.2. Two-dimensional periodic composites

Consider a two-dimensional periodic composite with elliptical fibers with a unit cell shown in Figure 2-2. For a unit cell with the edges defined by $\boldsymbol{I}^{\beta}$ $(\beta = 1, 2)$, the periodicity condition can be expressed as

$$C_{jkmn}(\boldsymbol{x}) = C_{jkmn}\left(\boldsymbol{x} + m'\boldsymbol{I}^{\beta}\right) \tag{2.16}$$

$$\rho(\boldsymbol{x}) = \rho\left(\boldsymbol{x} + m'\boldsymbol{I}^{\beta}\right) \tag{2.17}$$

where $\boldsymbol{x}$ is the position vector with components $x_j, (j = 1, 2)$, and $C_{jkmn}(\mathbf{x})$, $(j, k, m, n = 1, 2)$, are the components of the elasticity tensor.

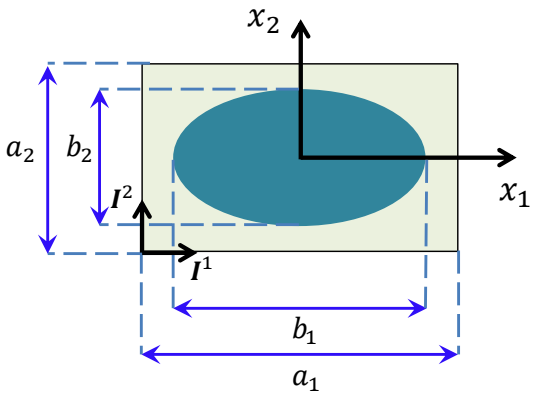

Figure 2-2: Unit cell of a two-dimensional periodic composite with elliptical inclusions

The field quantities for a harmonic wave with frequency ω ($\lambda = \omega^2$) are proportional to $e^{\pm i\omega t}$ and the field equations can be represented as

$$\sigma_{jk,k} + \lambda\rho u_j = 0 \tag{2.18}$$

where σ_{jk} and u_j are components of stress tensor and displacement vector, respectively. The constitutive relation can be written as

$$\sigma_{jk} = C_{jkmn}u_{m,n} \tag{2.19}$$

For harmonic waves with wave vector $\boldsymbol{q} = q_i\boldsymbol{e}_i$ ($i = 1, 2$), where $\boldsymbol{e}_i$ is the unit vector along x_i-direction, the Bloch boundary conditions have the following form

$$u_j(\boldsymbol{x} + \boldsymbol{l}^\beta) = u_j(\boldsymbol{x})e^{i\boldsymbol{q}.\boldsymbol{l}^\beta} \tag{2.20}$$

$$t_j(\boldsymbol{x} + \boldsymbol{l}^\beta) = -t_j(\boldsymbol{x})e^{i\boldsymbol{q}.\boldsymbol{l}^\beta} \tag{2.21}$$

where $\boldsymbol{t}$ is the traction vector. It can be shown that the eigenvalues of the problem can be found by rendering the following functional stationary [8]

$$\lambda_N = \frac{\langle\sigma_{jk}, u_{j,k}\rangle + \langle u_{j,k}, \sigma_{jk}\rangle - \langle D_{jkmn}\sigma_{jk}, \sigma_{mn}\rangle}{\langle\rho u_j, u_j\rangle} \tag{2.22}$$

where D_{jkmn} represents the components of the elastic compliance tensor. Consider the following expressions for the solution of the field equations (2.18)

$$\bar{u}_j = \sum_{\alpha,\beta=-M}^{M} U_i^{(\alpha\beta)} f^{(\alpha\beta)}(\mathbf{x}) \tag{2.23}$$

$$\bar{\sigma}_{jk} = \sum_{\alpha,\beta=-M}^{M} S_{jk}^{(\alpha\beta)} f^{(\alpha\beta)}(\mathbf{x}) \tag{2.24}$$

where $f^{(\alpha\beta)}(\mathbf{x})$ $(\alpha, \beta = -M, \dots, M)$ are a sequence of orthogonal, continuous, and continuously differentiable function which satisfy the Bloch boundary conditions (2.20) and (2.21). Substituting equations (2.23) and (2.24) into equation (2.22) and setting the derivatives of λ_N with respect to the unknown coefficients, $U_i^{(\alpha\beta)}$ and $S_{jk}^{(\alpha\beta)}$, equal to zero, the following set of linear homogenous equations can be obtained

$$\langle \bar{\sigma}_{jk,k} + \lambda_N \rho \bar{u}_j, f^{(\alpha\beta)} \rangle = 0 \tag{2.25}$$

$$\langle D_{jkmn} \bar{\sigma}_{mn} - \bar{u}_{j,k}, f^{(\alpha\beta)} \rangle = 0 \tag{2.26}$$

For two-dimensional PCs the approximating function can be chosen to be

$$f^{(\alpha\beta)} = e^{i[(Q_1 + 2\pi\alpha)\frac{x_1}{a_1} + (Q_2 + 2\pi\beta)\frac{x_2}{a_2}} \tag{2.27}$$

where a_1 and a_2 are the dimensions of the unit cell along the x_1- and x_2-axis (see Figure 2-2), and $Q_1 = q_1 a_1$ and $Q_2 = q_2 a_2$ are the normalized wave numbers along x_1- and x_2-directions, respectively. Substituting this relation for $f^{(\alpha\beta)}$ in equations (2.25) and (2.26), we find a matrix equations in the same form as given in equations (2.13) where **U** and **S** are the vectors of the unknown coefficients in the approximate expressions for the displacement vector and the stress tensor components, respectively; which can be expressed as $\mathbf{U} = \{\mathbf{U_1},\ \mathbf{U_2}\}^T$ with components $U_i^{(\alpha\beta)}(\ i = 1, 2),\ \alpha, \beta = 0, \pm 1, \dots, \pm M$; and $\mathbf{S} = \{\mathbf{S_{11}},\ \mathbf{S_{12}}, \mathbf{S_{22}}\}^T$ with components $S_{jk}^{(\alpha\beta)}$ $(j, k = 1,2)$. The explicit expression for the coefficient matrices **Ω**, **H**, and **Φ** are given in Appendix 2B. For nontrivial solution of

this system of equations, the determinant of the coefficients matrix in equation (2.15) should be set equal zero which gives the dispersion equation for a two-dimensional periodic composite.

2.1.3. Three-dimensional periodic composites

Consider a unit cell of a three-dimensional periodic composite with ellipsoidal inclusion as shown in Figure 2-3. For a unit cell with the edges defined by $\boldsymbol{I}^{\beta}$ ($\beta = 1, 2, 3$), the periodicity condition can be given by equations (2.16) and (2.17) with $j, k, m, n = 1, 2, 3$. Similarly, the field equations, constitutive relations, and Bloch boundary conditions can be given by equations (2.18), (2.19), (2.20), and (2.21), respectively. It can be shown that the eigenvalues of the problem can be found by rendering the functional in equation (2.22) stationary. The approximate solution for stress and displacement components are assumed in the following form

$$\bar{u}_j = \sum_{\alpha,\beta,\gamma=-M}^{M} U_i^{(\alpha\beta\gamma)} f^{(\alpha\beta\gamma)}(\mathbf{x}) \tag{2.28}$$

$$\bar{\sigma}_{jk} = \sum_{\alpha,\beta\gamma=-M}^{M} S_{jk}^{(\alpha\beta\gamma)} f^{(\alpha\beta\gamma)}(\mathbf{x}) \tag{2.29}$$

where

$$f^{(\alpha\beta\gamma)} = e^{i[(Q_1+2\pi\alpha)\frac{x_1}{a_1}+(Q_2+2\pi\beta)\frac{x_2}{a_2}+(Q_3+2\pi\gamma)\frac{x_3}{a_3}]} \tag{2.30}$$

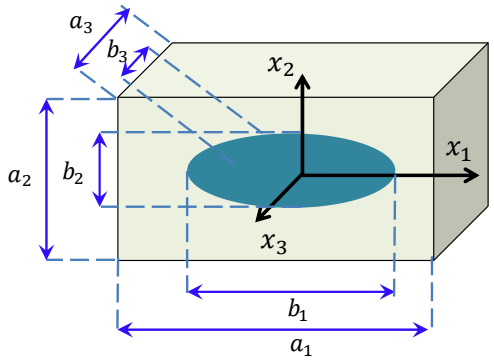

Figure 2-3: Unit cell of a three-dimensional periodic composite with ellipsoidal inclusion

where a_i and Q_i (i=1..3) are the length of the unit cell side and normalized wave number along the x_i-direction, respectively. Following the same procedure as for the two-dimensional PCs, the characteristic equation (2.15) can be solved to get the dispersion equation of the PC, where the coefficient matrices $\mathbf{\Omega}, \mathbf{H}$, and $\mathbf{\Phi}$ are given in Appendix 2C.

2.2. Transfer matrix method

2.2.1. Band structure calculation

Transfer matrix method provides exact solution for calculating the band structure of one-dimensional PCs [45]. Consider wave propagation in a one-dimensional PC made of infinite number of identical repeated unit cells with a unit cell shown in Figure 2-4. In this Figure, $E^{(j)}, \rho^{(j)}$, and $d^{(j)}$ are the elastic modulus, density, and thickness of j-th layer, respectively. The general solution for equation of motion in each layer can be expressed as the superposition of two longitudinal waves traveling in opposite directions

$$u(x,t) = [A_+^{(j)} e^{ik^{(j)}x} + A_-^{(j)} e^{-ik^{(j)}x}]e^{-i\omega t} \tag{2.31}$$

where $k^{(j)} = \omega/c^{(j)}$, $c^{(j)}$, $A_+^{(j)}$ and $A_-^{(j)}$ are the wave number in j-th layer, the longitudinal wave velocity, the amplitude of the waves traveling in positive and negative x-direction in j-th layer, respectively. The displacement and stress in the j-th layer can be expressed as

$$\begin{bmatrix} u(x) \\ \sigma(x) \end{bmatrix} = \mathbf{B}_j \begin{bmatrix} A_+^{(j)} e^{ik^{(j)}x} \\ A_-^{(j)} e^{-ik^{(j)}x} \end{bmatrix} \tag{2.32}$$

where

$$\mathbf{B}_j = \begin{bmatrix} 1 & 1 \\ iZ^{(j)} & -iZ^{(j)} \end{bmatrix} \tag{2.33}$$

where $Z^{(j)} = \rho^{(j)} c^{(j)^2} k^{(j)}$. Let x^{jL} and x^{jR} denote the left and right boundaries of j-th layer in the unit cell, respectively. Considering the relation $x^{jR} = x^{jL} + d^{(j)}$ and setting $\mathbf{D}_j\left(d^{(j)}\right) = \text{diag}[e^{\left(ik^{(j)}d^{(j)}\right)}, e^{\left(-ik^{(j)}d^{(j)}\right)}]$, equation (2.32) can be written as

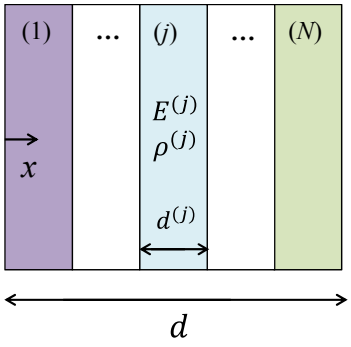

Figure 2-4: Unit cell of a one-dimensional periodic composite

$$\begin{bmatrix} u(x^{jR}) \\ \sigma(x^{jR}) \end{bmatrix} = \mathrm{T}_j \begin{bmatrix} u(x^{jL}) \\ \sigma(x^{jL}) \end{bmatrix} \tag{2.34}$$

where $\mathbf{T}_j = \mathbf{B}_j \mathbf{D}_j\left(d^{(j)}\right)\mathbf{B}_j^{-1}$ is the transfer matrix for *j*-th layer which can be expressed as

$$\mathbf{T}_j = \begin{bmatrix} \cos(k^{(j)}d^{(j)}) & \sin\left(k^{(j)}d^{(j)}\right)/Z^{(j)} \\ -Z^{(j)}\sin(k^{(j)}d^{(j)}) & \cos(k^{(j)}d^{(j)}) \end{bmatrix} \tag{2.35}$$

Applying the continuity of displacement and stress between each two adjacent layers, the displacement and stress at the left boundary of the first layer in the unit cell are related to those at the right boundary of the *N*-th layer by

$$\begin{bmatrix} u(x^{NR}) \\ \sigma(x^{NR}) \end{bmatrix} = \mathbf{T} \begin{bmatrix} u(x^{1L}) \\ \sigma(x^{1L}) \end{bmatrix} \tag{2.36}$$

where $\mathbf{T} = \mathbf{T}_N \mathbf{T}_{N-1} \ldots \mathbf{T}_1$ is the cumulative transfer matrix of the unit cell. For Bloch type waves the displacement and stress at a given point of the unit cell are related to the corresponding point in the adjacent unit cell by

$$\mathbf{y}(x + d) = e^{ikd}\mathbf{y}(x) \tag{2.37}$$

where $\mathbf{y}(x) = \begin{bmatrix} u(x) \\ \sigma(x) \end{bmatrix}$ and k is the Bloch-wave number. Equations (2.36) and (2.37) lead to the following eigenvalue problem

$$\mathbf{T}(\omega)\mathbf{y}(x^{1L}) = \lambda\mathbf{y}(x^{1L}) \tag{2.38}$$

where $\lambda = \exp(ikd)$ is the eigenvalue and $\mathbf{y}(x^{1L})$ is the eigenvector. Solutions of this equation give the band structure for longitudinal wave propagation in an infinite one-dimensional PC.

2.2.2. Finite one-dimensional periodic composites

Transfer matrix method provides a solution for calculating the reflection and transmission coefficients at the interfaces of a one-dimensional composite sandwiched by two homogenous half-spaces. Consider *m* unit cells of a one-dimensional composite each made of *N* individual layers sandwiched by two homogenous half-spaces, as shown in Figure 2-5. Assume there is an incoming harmonic wave with amplitude $A_+^{(0)}$ moving toward positive *x*-direction, and a reflected wave moving backward with amplitude $A_-^{(0)}$ in the incident medium. The displacement in the incident medium, M_0, can be expressed as

$$u(x,t) = [A_+^{(0)} e^{ik^{(0)}x} + A_-^{(0)} e^{-ik^{(0)}x}] e^{-i\omega t} \tag{2.39}$$

The displacement in each layer of the composite can be given by equation (2.31) and the displacement in the transmission medium, M_{m+1}, can be given by

$$u(x,t) = A_+^{(m+1)} e^{i(k^{(m+1)}x - \omega t)} \tag{2.40}$$

The field variables at the left boundary of the first layer in the first unit cell of the composite are related to those at the right boundary of the *N*-th layer in the *m*-th unit cell by

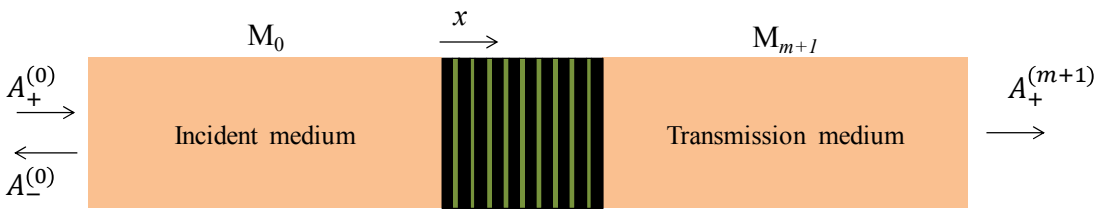

Figure 2-5: A finite one-dimensional periodic composite sandwiched by two homogenous half-spaces

$$\begin{bmatrix} u(x^{NR,m}) \\ \sigma(x^{NR,m}) \end{bmatrix} = \mathbf{T}^m \begin{bmatrix} u(x^{1L,1}) \\ \sigma(x^{1L,1}) \end{bmatrix} \tag{2.41}$$

Applying the continuity of displacement and stress at the interfaces of the composite with M_0 and M_{m+1}, the following relation can be found

$$\begin{bmatrix} A_+^{(m+1)} \\ 0 \end{bmatrix} = \mathbf{K} \begin{bmatrix} A_+^{(0)} \\ A_-^{(0)} \end{bmatrix} \tag{2.42}$$

where $\mathbf{K} = \mathbf{L}^{(m)^{-1}}(D)\mathbf{B}^{(m+1)^{-1}}\mathbf{T}\mathbf{B}^{(0)}$, in which the matrices $\mathbf{L}^{(j)}$ and $\mathbf{B}^{(j)}$ are given by

$$\mathbf{L}^{(j)}(x) = \begin{bmatrix} \exp(ik^{(j)}x) & 0 \\ 0 & \exp(-ik^{(j)}x) \end{bmatrix} \tag{2.43}$$

$$\mathbf{B}^{(j)} = \begin{bmatrix} 1 & 1 \\ iZ^{(j)} & -iZ^{(j)} \end{bmatrix} \tag{2.44}$$

Solving for the reflection coefficient, *R*, and the transmission coefficients, *T*, we find

$$R = \frac{A_-^{(0)}}{A_+^{(0)}} = -\frac{\mathbf{K}_{21}}{\mathbf{K}_{22}} \tag{2.45}$$

$$T = \frac{A_+^{(m+1)}}{A_+^{(0)}} = \mathbf{K}_{11} - \frac{\mathbf{K}_{12}\mathbf{K}_{21}}{\mathbf{K}_{22}} \tag{2.46}$$

In the absence of viscous dissipation, energy is conserved and the following relation holds

$$RR^* + TT^* = 1 \tag{2.47}$$

which means the energy of the incident wave is either reflected or transmitted to the transmission bar.

2.3. Dynamic homogenization

2.3.1. One-dimensional periodic composites

2.3.1.1. Field variables averaging

Effective elastodynamic properties of one-dimensional PCs can be calculated through homogenization by integration of field variables [39]. Consider Bloch waves in an infinite layered elastic composite made of identical repeated unit cells $\Omega = \{x: 0 \leq x < d\}$. For harmonic waves with wave number q and frequency ω, the field variables can be expressed as

$$\begin{gathered}\sigma(x,t) = \Sigma(x)exp[i(qx-\omega t)], \quad \varepsilon(x,t) = E(x)exp[i(qx-\omega t)] \\ u(x,t) = U(x)exp[i(qx-\omega t)], \quad \dot{u}(x,t) = \dot{U}(x)exp[i(qx-\omega t)] \\ p(x,t) = P(x)exp[i(qx-\omega t)]\end{gathered} \tag{2.48}$$

where the variables p and $\dot{u}$ are linear momentum and velocity, respectively; while $\Sigma(x)$, $E(x)$, $P(x)$, $U(x)$, and $\dot{U}(x)$ represent periodic parts of stress, strain, linear momentum, displacement, and velocity, respectively. The conservation and kinetic relations are given by equations (2.2) and (2.4) and the linear momentum-velocity relation can be given by $p = \rho(x)\dot{u}$. Multiplying equations (2.2) and (2.4) by e^{-iqX} and using equations (2.48) to replace for the field variables we get the following expressions

$$\begin{gathered}\nabla\left(\Sigma(x)e^{iq(x-X)}\right) + i\omega P(x)e^{iq(x-X)} = 0 \\ \nabla\left(\dot{U}(x)e^{iq(x-X)}\right) + i\omega E(x)e^{iq(x-X)} = 0\end{gathered} \tag{2.49}$$

where $\nabla = \frac{\partial}{\partial x} + iq$. Consider the change of variable $y = x - X$ to obtain

$$\nabla_y\left(\Sigma(X+y)e^{iqy}\right)+i\omega P(X+y)e^{iqy}=0$$
$$\nabla_y\left(\dot{U}(X+y)e^{iqy}\right)+i\omega E(X+y)e^{iqy}=0 \tag{2.50}$$

Average the above equations with respect to X over the unit cell to get

$$\nabla_y\left(\bar{\Sigma}e^{iqy}\right)+i\omega\bar{P}e^{iqy}=0$$
$$\nabla_y\left(\bar{\dot{U}}e^{iqy}\right)+i\omega\bar{E}e^{iqy}=0 \tag{2.51}$$

where any of the barred quantities are defined by

$$\bar{G}=\frac{1}{a}\int_{-a/2}^{a/2}G(X)dX \tag{2.52}$$

Define the mean constitutive relations as

$$\bar{E}=D_{eff}\bar{\Sigma},\quad \bar{P}=\rho_{eff}\bar{\dot{U}} \tag{2.53}$$

The averaged field quantities $\bar{\Sigma}$, $\bar{E}$, $\bar{P}$, and $\bar{\dot{U}}$ are used in equations (2.53) to calculate the effective compliance, D_{eff}, and effective desnity, ρ_{eff}. Note that the overall field variables defined by (2.52) satisfy the overall field equations as is ensured by equations (2.51), from which we have

$$\bar{\Sigma}+\frac{\omega}{q}\bar{P}=0,\qquad \bar{\dot{U}}+\frac{\omega}{q}\bar{E}=0 \tag{2.54}$$

In order to have nontrivial solution for four linear and homogenous equations (2.53) and (2.54) we must have

$$\frac{1}{D_{eff}\rho_{eff}}=\left(\frac{\omega}{q}\right)^2 \tag{2.55}$$

which satisfies the dispersion relation.

2.3.1.2. Micromechanical method

The effective elastodynamic properties of one-dimensional PCs can be calculated through micromechanical modeling of a unit cell [40]. The solution to equation of motion for a one-dimensional composite can be expressed as sum of the volume average and a disturbance field due to the heterogeneities in the unit cell as

$$\hat{\phi} = \phi^0 + \phi^d \tag{2.56}$$

where $\hat{\phi}$ represents any of the field variables, stress ($\hat{\sigma}$), strain ($\hat{\varepsilon}$), momentum ($\hat{p}$) or velocity ($\hat{\dot{u}}$). For Bloch type waves the field variables can be written as

$$\hat{\phi}(x,t) = Re[\phi(x)\, exp[i(qx - \omega t)]] \tag{2.57}$$

where ϕ represents the periodic parts of the field variables ($\sigma, \varepsilon, p, \dot{u}$). The local conservation and kinetic relations can be written in the following form

$$\begin{aligned} \widetilde{\nabla}.\sigma &= -i\omega p \\ \widetilde{\nabla}\dot{u} &= -i\omega\varepsilon \end{aligned} \tag{2.58}$$

where $\widetilde{\nabla} \rightarrow \nabla + iq$. The local constitutive relations can be expressed as

$$\begin{aligned} \varepsilon &= D(x)\sigma \\ p &= \rho(x)\dot{u} \end{aligned} \tag{2.59}$$

The heterogeneous unit cell is replaced by a homogenous one with uniform density ρ^0 and compliance D^0. Eigenstress, $\Sigma(x)$, and eigenvelocity, $\dot{U}(x)$, are introduced such that the pointwise values of the field variables are the same as the original heterogeneous solid. Therefore, the consistency conditions can be expressed as

$$\varepsilon(x) = D(x)\sigma(x) = D^0(\sigma(x) - \Sigma(x))$$
$$p(x) = \rho(x)\dot{u}(x) = \rho^0(\dot{u}(x) - \dot{U}(x)) \tag{2.60}$$

Averaging the consistency conditions (2.87) we obtain

$$\langle\varepsilon\rangle = D^0[\langle\sigma\rangle - \langle\Sigma\rangle]$$
$$\langle p\rangle = \rho^0\left[\langle\dot{u}\rangle - \langle\dot{U}\rangle\right] \tag{2.61}$$

Using equations (2.58) and (2.60) we have

$$\nabla^2\sigma + \nu^2\sigma = \nu^2\Sigma - \frac{\nu^2}{i\omega D^0}\nabla\dot{U}$$
$$\nabla^2\dot{u} + \nu^2\dot{u} = \nu^2\dot{U} - \frac{\nu^2}{i\omega\rho^0}\nabla\Sigma \tag{2.62}$$

where $\nu^2 = \omega^2\rho^0 D^0$. Since the field variables, ϕ, are periodic they can be written in terms of Fourier series

$$\phi(x) = \langle\phi\rangle + \phi^p = \langle\phi\rangle + \sum_{\xi\neq 0}\phi(\xi)e^{i\xi x}$$
$$\langle\phi\rangle = \frac{1}{\Omega}\int_\Omega \phi(x)dx$$
$$\phi(\xi) = \tfrac{1}{\Omega}\textstyle\int_\Omega\ \phi(x)e^{-i\xi x}dA \tag{2.63}$$
$$\xi = \mp\frac{2n\pi}{a}, \qquad n \neq 0$$

where $\langle\phi\rangle$ is the averaged value of the field variables over the unit cell and ϕ^p is the local deviations from the average value. From equations (2.62) the Fourier coefficients for stress and velocity fields are obtained

$$\sigma(\xi) = \frac{\nu^2}{\nu^2 - (\xi+q)^2}\Sigma(\xi) - \frac{\nu^2(\xi+q)}{\omega D^0(\nu^2-(\xi+q)^2)}\dot{U}(\xi)$$
$$\dot{u}(\xi) = \frac{\nu^2}{\nu^2 - (\xi+q)^2}\dot{U}(\xi) - \frac{\nu^2(\xi+q)}{\omega \rho^0(\nu^2-(\xi+q)^2)}\Sigma(\xi) \tag{2.64}$$

Therefore, the stress and velocity fields can be expressed as

$$\dot{u}(x) = \langle\dot{u}\rangle + \sum_{\xi\neq 0} e^{i\xi x}\left[A(\xi)\frac{1}{\Omega}\int_\Omega \Sigma(y)e^{-i\xi y}dy + \frac{B(\xi)}{\omega\rho^0}\frac{1}{\Omega}\int_\Omega \dot{U}(y)e^{-i\xi y}dy\right] \tag{2.65}$$

$$\sigma(x) = \langle\sigma\rangle + \sum_{\xi\neq 0} e^{i\xi x}\left[A(\xi)\frac{1}{\Omega}\int_\Omega \Sigma(y)e^{-i\xi y}dy + \frac{B(\xi)}{\omega D^0}\frac{1}{\Omega}\int_\Omega \dot{U}(y)e^{-i\xi y}dy\right] \tag{2.66}$$

To calculate $\langle\Sigma\rangle$ and $\langle\dot{U}\rangle$ the unit cell is divided into $\bar{\alpha}$ subregions, Ω_α, and we average the periodic parts over each subregion

$$\langle\sigma^p\rangle_{\Omega_\alpha} = \sigma^{p\alpha} = \frac{1}{\Omega_\alpha}\int_{\Omega_\alpha}\sigma^p \mathrm{d}x$$
$$= \sum_{\xi\neq 0} g^\alpha(\xi)\left[A(\xi)\frac{1}{\Omega}\int_\Omega \Sigma(y)e^{-i\xi y}\mathrm{d}y + \frac{B(\xi)}{\omega D^0}\frac{1}{\Omega}\int_\Omega \dot{U}(y)e^{-i\xi y}dy\right] \tag{2.67}$$

$$\langle \dot{u}^p \rangle_{\Omega_\alpha} = \dot{u}^{p\alpha} = \frac{1}{\Omega_\alpha} \int_{\Omega_\alpha} \dot{u}^p \mathrm{d}x$$

$$= \sum_{\xi \neq 0} g^\alpha(\xi) \left[A(\xi) \frac{1}{\Omega} \int_\Omega \Sigma(y) e^{-i\xi y} dy \right.$$

$$\left. + \frac{B(\xi)}{\omega \rho^0} \frac{1}{\Omega} \int_\Omega \dot{U}(y) e^{-i\xi y} dy \right]$$

where $g^\alpha(\xi) = \frac{1}{\Omega_\alpha} \int_{\Omega_\alpha} e^{i\xi x} \mathrm{d}x$. The integrals in equations (2.67) are replaced by their equivalent finite sums as

$$\frac{1}{\Omega} \int_\Omega F(y) e^{-i\xi y} \mathrm{d}y \approx \sum_\beta f^\beta g^\beta(-\xi) F^\beta$$

$$f^\beta = \Omega_\beta / \Omega, \qquad F^\beta = \langle F \rangle_{\Omega_\beta} \tag{2.68}$$

Equations (2.67) then yield

$$\sigma^{p\alpha} = A_{\alpha\beta} \Sigma_\beta - \frac{1}{\omega D^0} B_{\alpha\beta} \dot{U}_\beta$$

$$\dot{u}^{p\alpha} = A_{\alpha\beta} \dot{U}_\beta - \frac{1}{\omega \rho^0} B_{\alpha\beta} \Sigma_\beta \tag{2.69}$$

where the coefficient matrices are given by

$$A_{\alpha\beta} = \sum_{\xi \neq 0} g^\alpha(\xi) f^\beta \, g^\beta(-\xi) A(\xi)$$

$$B_{\alpha\beta} = \sum_{\xi \neq 0} g^\alpha(\xi) f^\beta \, g^\beta(-\xi) B(\xi) \tag{2.70}$$

Averaging the consistency conditions over each subregion and using equations (2.69) we have

$$f^{\alpha}\langle\sigma\rangle = -\left[\bar{A}_{\alpha\beta} + \frac{f^{\alpha}D^{0}}{D^{\alpha}-D^{0}}\delta_{\alpha\beta}\right]\Sigma_{\beta} + \frac{1}{\omega D^{0}}\bar{B}_{\alpha\beta}\dot{U}_{\beta}$$
$$f^{\alpha}\langle\dot{u}\rangle = \frac{1}{\omega\rho^{0}}\bar{B}_{\alpha\beta}\Sigma_{\beta} - \left[\bar{A}_{\alpha\beta} + \frac{f^{\alpha}\rho^{0}}{\rho^{\alpha}-\rho^{0}}\delta_{\alpha\beta}\right]\dot{U}_{\beta} \tag{2.71}$$

where $\bar{A}_{\alpha\beta} = f^{\alpha}A_{\alpha\beta}$ and $\bar{B}_{\alpha\beta}$=$f^{\alpha}B_{\alpha\beta}$. Equations (2.71) can be rewritten in matrix form as

$$\{\boldsymbol{\Sigma}\} = \{\boldsymbol{\Phi}\}\langle\sigma\rangle + \frac{1}{D^{0}}\{\boldsymbol{\Psi}\}\langle\dot{u}\rangle$$
$$\{\dot{\boldsymbol{U}}\} = \frac{1}{\rho^{0}}\{\boldsymbol{\Theta}\}\langle\sigma\rangle + \{\boldsymbol{\Gamma}\}\langle\dot{u}\rangle \tag{2.72}$$

where the coefficient matrices can be expressed as

$$\{\boldsymbol{\Phi}\} = \left[-[\boldsymbol{A_D}] + \frac{1}{\nu^{2}}[\boldsymbol{B}]\left[\boldsymbol{A}_{\rho}\right]^{-1}[\boldsymbol{B}]\right]^{-1}\{f\}$$
$$\{\boldsymbol{\Psi}\} = \frac{1}{\omega}\left[-[\boldsymbol{A_D}] + \frac{1}{\nu^{2}}[\boldsymbol{B}]\left[\boldsymbol{A}_{\rho}\right]^{-1}[\boldsymbol{B}]\right]^{-1}[\boldsymbol{B}]\left[\boldsymbol{A}_{\rho}\right]^{-1}\{f\}$$
$$\{\boldsymbol{\Theta}\} = \frac{1}{\omega}\left[-\left[\boldsymbol{A_{\rho}}\right] + \frac{1}{\nu^{2}}[\boldsymbol{B}][\boldsymbol{A_D}]^{-1}[\boldsymbol{B}]\right]^{-1}[\boldsymbol{B}][\boldsymbol{A}_{D}]^{-1}\{f\} \tag{2.73}$$
$$\{\boldsymbol{\Gamma}\} = \left[-\left[\boldsymbol{A_{\rho}}\right] + \frac{1}{\nu^{2}}[\boldsymbol{B}][\boldsymbol{A_D}]^{-1}[\boldsymbol{B}]\right]^{-1}\{f\}$$

where

$$[\boldsymbol{A_D}]_{\alpha\beta} = \bar{A}_{\alpha\beta} + \frac{f^{\alpha} D^0}{D^{\alpha} - D^0}\delta_{\alpha\beta}$$
$$\left[\boldsymbol{A_\rho}\right]_{\alpha\beta} = \bar{A}_{\alpha\beta} + \frac{f^{\alpha} \rho^0}{\rho^{\alpha} - \rho^0}\delta_{\alpha\beta} \tag{2.74}$$

The average consistency equations (2.61) can be expressed as

$$\langle \varepsilon \rangle = \bar{D}\langle \sigma \rangle + \bar{S}^1\langle \dot{u} \rangle$$
$$\langle p \rangle = \bar{S}^2\langle \sigma \rangle + \bar{\rho}\langle \dot{u} \rangle \tag{2.75}$$

which are the final constitutive relations for the homogenized medium. The expression for the effective parameters can be given by

$$\bar{D} = -D^0[1 - \{f\}^T\{\boldsymbol{\Phi}\}]$$
$$\bar{S}^1 = -\{f\}^T\{\boldsymbol{\Psi}\}$$
$$\bar{S}^2 = -\{f\}^T\{\boldsymbol{\Theta}\} \tag{2.76}$$
$$\bar{\rho} = \rho^0[1 - \{f\}^T\{\boldsymbol{\Gamma}\}]$$

Now, consider an infinite homogenized elastic solid with layered microstructure, and seek conditions under which it supports Bloch type waves of the form

$$\langle \sigma \rangle(x) = \langle \sigma \rangle e^{iqx}$$
$$\langle \dot{u} \rangle(x) = \langle \dot{u} \rangle e^{iqx}$$
$$\langle \varepsilon \rangle(x) = \langle \varepsilon \rangle e^{iqx} \tag{2.77}$$
$$\langle p \rangle(x) = \langle p \rangle e^{iqx}$$

The overall field equations then become

$$\frac{d}{dx}\left(\langle\sigma\rangle e^{iqx}\right) = -i\omega\langle p\rangle e^{iqx}$$
$$\frac{d}{dx}\left(\langle\dot{u}\rangle e^{iqx}\right) = -i\omega\langle\varepsilon\rangle e^{iqx} \tag{2.78}$$

which yield

$$q\langle\sigma\rangle = -\omega\langle p\rangle$$
$$q\langle\dot{u}\rangle = -\omega\langle\varepsilon\rangle \tag{2.79}$$

These equations are combined with the constitutive equations (2.75) to get

$$K(q,\omega)\dot{u} = 0 \tag{2.80}$$

For nontrivial solutions to the above equation $K(q,\omega)$ should be equal to zero which produces the dispersion relation of the composite and it can be written as

$$\left(\frac{\omega}{q}\right)^2 = v_p^2 = \frac{(1+v_p\bar{S}^1)(1+v_p\bar{S}^2)}{\bar{D}\bar{\rho}} \tag{2.81}$$

where v_p is the phase velocity.

2.3.2. Two-dimensional periodic composites

The effective elastodynamic properties of two-dimensional PCs can be calculated through micromechanical modeling of a unit cell. The solution to the equations of motion for a two-dimensional elastic composite can be expressed as the sum of the volume average and a disturbation term due to heterogeneities in the unit cell as

$$\widehat{\boldsymbol{\phi}} = \boldsymbol{\phi}^0 + \boldsymbol{\phi}^d \tag{2.82}$$

where $\widehat{\boldsymbol{\phi}}$ represents any of the field variables, stress ($\widehat{\boldsymbol{\sigma}}$), strain ($\widehat{\boldsymbol{\varepsilon}}$), momentum ($\widehat{\boldsymbol{p}}$) or velocity ($\widehat{\boldsymbol{u}}$). For Bloch type waves the field variables can be written as

$$\hat{\phi}(\boldsymbol{x}, t) = Re[\phi(\boldsymbol{x})\, exp[i(\boldsymbol{q}.\boldsymbol{x} - \omega t)]] \tag{2.83}$$

where $\boldsymbol{\phi}$ represents the periodic parts of the field variables ($\boldsymbol{\sigma}, \boldsymbol{\varepsilon}, \boldsymbol{p}, \dot{\boldsymbol{u}}$). The local conservation and kinetic relations can be written in the following form

$$\begin{aligned} \tilde{\boldsymbol{\nabla}}.\boldsymbol{\sigma} &= -i\omega\boldsymbol{p} \\ \left(\tilde{\boldsymbol{\nabla}} \otimes \dot{\boldsymbol{u}}\right)_{\text{sym}} &= -i\omega\boldsymbol{\varepsilon} \end{aligned} \tag{2.84}$$

where $\tilde{\boldsymbol{\nabla}} \rightarrow \boldsymbol{\nabla} + i\mathbf{q}$. The local constitutive relations can be expressed as

$$\begin{aligned} \boldsymbol{\varepsilon} &= \mathbf{D}\colon\boldsymbol{\sigma} \\ \boldsymbol{p} &= \rho\dot{\boldsymbol{u}} \end{aligned} \tag{2.85}$$

where $\mathbf{D}(\mathbf{x})$ is the compliance tensor and $\rho(\mathbf{x})$ is the density. The heterogeneous unit cell is replaced by a homogenous one with uniform density ρ^0 and compliance $\mathbf{D}^0$. Eigenstrains, $\mathbf{E}(\mathbf{x})$, and eigenmomentums, $\mathbf{P}(\mathbf{x})$, are introduced such that the pointwise values of the field variables are the same as the original heterogeneous solid. Therefore, the consistency conditions can be expressed as

$$\begin{aligned} \boldsymbol{\varepsilon} &= \mathbf{D}\colon\boldsymbol{\sigma} = \mathbf{D^0}\colon\boldsymbol{\sigma} - \mathbf{E} \\ \boldsymbol{p} &= \rho\dot{\boldsymbol{u}} = \rho^0\dot{\boldsymbol{u}} - \mathbf{P} \end{aligned} \tag{2.86}$$

Using equations (2.85) and (2.86), equations (2.84) can be written as

$$\tilde{\boldsymbol{\nabla}}.\mathbf{C}^0\colon\left(\tilde{\boldsymbol{\nabla}} \otimes \dot{\boldsymbol{u}}\right)_{\text{sym}} + \omega^2\rho^0\dot{\boldsymbol{u}} = \omega^2\mathbf{P} + i\omega\left(\tilde{\boldsymbol{\nabla}}.\mathbf{C}^0\colon\mathbf{E}\right) \tag{2.87}$$

$$\mathbf{C}^0\colon\left[\tilde{\nabla}\otimes\left(\tilde{\nabla}.\boldsymbol{\sigma}\right)\right]_{\text{sym}}+\omega^2\rho^0\boldsymbol{\sigma}=\omega^2\rho^0\mathbf{C}^0\colon\mathbf{E}+i\omega\mathbf{C}^0\left(\tilde{\nabla}\otimes\mathbf{P}\right)_{\text{sym}}$$

Since the field variables, $\boldsymbol{\phi}$, are periodic they can be written in terms of Fourier series

$$\boldsymbol{\phi}(\boldsymbol{x})=\langle\boldsymbol{\phi}\rangle+\boldsymbol{\phi}^p=\langle\boldsymbol{\phi}\rangle+\sum_{\boldsymbol{\xi}\neq\mathbf{0}}\boldsymbol{\phi}(\boldsymbol{\xi})e^{i\boldsymbol{\xi}.\boldsymbol{x}} \tag{2.88}$$

$$\langle\boldsymbol{\phi}\rangle=\frac{1}{\Omega}\int_{\Omega}\boldsymbol{\phi}(\boldsymbol{x})\mathrm{d}A_x$$

$$\boldsymbol{\phi}(\boldsymbol{\xi})=\frac{1}{\Omega}\int_{\Omega}\boldsymbol{\phi}(\boldsymbol{x})e^{-i\boldsymbol{\xi}.\boldsymbol{x}}\mathrm{d}A \tag{2.89}$$

$$\Omega=4a_1a_2,\quad\boldsymbol{\xi}=\xi_i\boldsymbol{e}_i,\quad\xi_i=\frac{n_i\pi}{a_i},\ i=1,2,\ n_i\text{ integers}$$

where $\langle\boldsymbol{\phi}\rangle$ is the averaged value of the field variables over the unit cell and $\boldsymbol{\phi}^p$ is the local deviations from the average value. Using equation (2.88), equations (2.87) is written as

$$\begin{gathered}\boldsymbol{\zeta}.\mathbf{C}^0\colon(\boldsymbol{\zeta}\otimes\dot{\boldsymbol{u}})_{\text{sym}}+\omega^2\rho^0\dot{\boldsymbol{u}}=\omega^2\mathbf{P}+i\omega(\boldsymbol{\zeta}.\mathbf{C}^0\colon\mathbf{E})\\-\mathbf{C}^0\colon[\boldsymbol{\zeta}\otimes(\boldsymbol{\zeta}.\boldsymbol{\sigma})]_{\text{sym}}+\omega^2\rho^0\boldsymbol{\sigma}=\omega^2\rho^0\mathbf{C}^0\colon\mathbf{E}-\omega\mathbf{C}^0(\boldsymbol{\zeta}\otimes\mathbf{P})_{\text{sym}}\end{gathered} \tag{2.90}$$

where $\boldsymbol{\zeta}=\boldsymbol{\xi}+\boldsymbol{q}$. For the case of an isotropic reference material

$$C^0_{ijkl}=\lambda'_0\delta_{ij}\delta_{kl}+\mu_0\left(\delta_{ik}\delta_{jl}+\delta_{il}\delta_{jk}\right) \tag{2.91}$$

where μ_0 is the shear modulus and λ'_0 is defined as $\mu_0(3-\kappa_0)/(\kappa_0-1)$ in which $\kappa_0=3-4\nu_0$ for plane strain and $\kappa_0=(3-\nu_0)/(1+\nu_0)$ for plane stress. Using equation (2.91), Fourier coefficients for components of displacement and stress tensor can be written as

$$\dot{\boldsymbol{u}}(\boldsymbol{\xi}) = \boldsymbol{\Phi}(\boldsymbol{\zeta}).\mathbf{P}(\boldsymbol{\xi}) + \boldsymbol{\Theta}(\boldsymbol{\zeta}):\mathbf{E}(\boldsymbol{\xi})$$
$$\boldsymbol{\sigma}(\boldsymbol{\xi}) = \boldsymbol{\Psi}(\boldsymbol{\zeta}).\mathbf{P}(\boldsymbol{\xi}) + \boldsymbol{\Gamma}(\boldsymbol{\zeta}):\mathbf{E}(\boldsymbol{\xi}) \tag{2.92}$$

where the coefficient tensors $\boldsymbol{\Phi}$, $\boldsymbol{\Theta}$, $\boldsymbol{\Psi}$, and $\boldsymbol{\Gamma}$ are given in Appendix 2D. Using equations (2.92) the stress and velocity fields can be expressed as

$$\dot{\boldsymbol{u}}(\boldsymbol{x}) = \langle\dot{\boldsymbol{u}}\rangle + \sum_{\boldsymbol{\xi}\neq\mathbf{0}} e^{i\boldsymbol{\xi}.\boldsymbol{x}}\left[\boldsymbol{\Phi}(\boldsymbol{\zeta}).\frac{1}{\Omega}\int_{\Omega}\boldsymbol{P}(\boldsymbol{y})e^{-i\boldsymbol{\xi}.\boldsymbol{y}}\mathrm{d}A_y + \boldsymbol{\Theta}(\boldsymbol{\zeta}):\frac{1}{\Omega}\int_{\Omega}\boldsymbol{E}(\boldsymbol{y})e^{-i\boldsymbol{\xi}.\boldsymbol{y}}\mathrm{d}A_y\right]$$
$$\boldsymbol{\sigma}(\boldsymbol{x}) = \langle\boldsymbol{\sigma}\rangle + \sum_{\boldsymbol{\xi}\neq\mathbf{0}} e^{i\boldsymbol{\xi}.\boldsymbol{x}}\left[\boldsymbol{\Psi}(\boldsymbol{\zeta}).\frac{1}{\Omega}\int_{\Omega}\boldsymbol{P}(\boldsymbol{y})e^{-i\boldsymbol{\xi}.\boldsymbol{y}}\mathrm{d}A_y + \boldsymbol{\Gamma}(\boldsymbol{\zeta}):\frac{1}{\Omega}\int_{\Omega}\boldsymbol{E}(\boldsymbol{y})e^{-i\boldsymbol{\xi}.\boldsymbol{y}}\mathrm{d}A_y\right] \tag{2.93}$$

The consistency equations can therefore be written as

$$\boldsymbol{\varepsilon}(\boldsymbol{x}) = \mathbf{D}(\boldsymbol{x}):[\langle\boldsymbol{\sigma}\rangle + \boldsymbol{\sigma}^p] = \mathbf{D^0}:[\langle\boldsymbol{\sigma}\rangle + \boldsymbol{\sigma}^p] - \mathbf{E}$$
$$\boldsymbol{p}(\boldsymbol{x}) = \rho(\boldsymbol{x})[\langle\dot{\boldsymbol{u}}\rangle + \dot{\boldsymbol{u}}^p] = \rho^0[\langle\dot{\boldsymbol{u}}\rangle + \dot{\boldsymbol{u}}^p] - \mathbf{P} \tag{2.94}$$

Equations (2.94) are averaged over a unit cell and written as

$$\langle\boldsymbol{\varepsilon}\rangle = \mathbf{D^0}:\langle\boldsymbol{\sigma}\rangle - \langle\mathbf{E}\rangle$$
$$\langle\boldsymbol{p}\rangle = \rho^0\langle\dot{\boldsymbol{u}}\rangle - \langle\mathbf{P}\rangle \tag{2.95}$$

In order to calculate $\langle\mathbf{E}\rangle$ and $\langle\mathbf{P}\rangle$, the unit cell is divided into $\bar{\alpha}$ subregions, Ω_α, and the periodic part of the field variables are averaged over each subregion

$$\langle \boldsymbol{\sigma}^p \rangle_{\Omega_\alpha} = \boldsymbol{\sigma}^{p\alpha} = \frac{1}{\Omega_\alpha} \int_{\Omega_\alpha} \boldsymbol{\sigma}^p \mathrm{d}A_x$$

$$= \sum_{\boldsymbol{\xi} \neq \mathbf{0}} g^\alpha(\boldsymbol{\xi}) \left[\boldsymbol{\Psi}(\boldsymbol{\zeta}) . \frac{1}{\Omega} \int_\Omega \boldsymbol{P}(\boldsymbol{y}) e^{-i\boldsymbol{\xi}.\boldsymbol{y}} \mathrm{d}A_y \right.$$

$$\left. + \boldsymbol{\Gamma}(\boldsymbol{\zeta}) : \frac{1}{\Omega} \int_\Omega \boldsymbol{E}(\boldsymbol{y}) e^{-i\boldsymbol{\xi}.\boldsymbol{y}} \mathrm{d}A_y \right] \tag{2.96}$$

$$\langle \dot{\boldsymbol{u}}^p \rangle_{\Omega_\alpha} = \dot{\boldsymbol{u}}^{p\alpha} = \frac{1}{\Omega_\alpha} \int_{\Omega_\alpha} \dot{\boldsymbol{u}}^p \mathrm{d}A_x$$

$$= \sum_{\boldsymbol{\xi} \neq \mathbf{0}} g^\alpha(\boldsymbol{\xi}) \left[\boldsymbol{\Phi}(\boldsymbol{\zeta}) . \frac{1}{\Omega} \int_\Omega \boldsymbol{P}(\boldsymbol{y}) e^{-i\boldsymbol{\xi}.\boldsymbol{y}} \mathrm{d}A_y \right.$$

$$\left. + \boldsymbol{\Theta}(\boldsymbol{\zeta}) : \frac{1}{\Omega} \int_\Omega \boldsymbol{E}(\boldsymbol{y}) e^{-i\boldsymbol{\xi}.\boldsymbol{y}} \mathrm{d}A_y \right]$$

where $g^\alpha(\boldsymbol{\xi}) = \frac{1}{\Omega_\alpha} \int_{\Omega_\alpha} e^{i\boldsymbol{\xi}.\boldsymbol{x}} \mathrm{d}A_x$. The integrals in equations (2.96) are replaced by their equivalent finite sums as

$$\frac{1}{\Omega} \int_\Omega \boldsymbol{F}(\boldsymbol{y}) e^{-i\boldsymbol{\xi}.\boldsymbol{y}} \mathrm{d}A_y \approx \sum_\beta f^\beta g^\beta(-\boldsymbol{\xi}) \boldsymbol{F}^\beta$$

$$f^\beta = \Omega_\alpha / \Omega, \qquad \boldsymbol{F}^\beta = \langle \boldsymbol{F} \rangle_{\Omega_\beta} \tag{2.97}$$

which is used to write equations (2.96) as

$$\boldsymbol{\sigma}^{p\alpha} = \frac{1}{f^\alpha} \left[\boldsymbol{\Psi}^{\alpha\beta} . \mathbf{P}^\beta + \boldsymbol{\Gamma}^{\alpha\beta} : \mathbf{E}^\beta \right]$$

$$\dot{\boldsymbol{u}}^{p\alpha} = \frac{1}{f^\alpha} \left[\boldsymbol{\Phi}^{\alpha\beta} . \mathbf{P}^\beta + \boldsymbol{\Theta}^{\alpha\beta} : \mathbf{E}^\beta \right] \tag{2.98}$$

where the coefficient tensors in these equations are defined by

$$\mathbf{M}^{\alpha\beta}=\sum_{\boldsymbol{\xi}\neq\mathbf{0}} f^{\alpha} g^{\alpha}(\boldsymbol{\xi}) f^{\beta}\, g^{\beta}(-\boldsymbol{\xi})\mathbf{M}(\boldsymbol{\zeta}) \tag{2.99}$$

Using equations (2.98) and averaging the consistency conditions over each subregion we get

$$\begin{aligned} f^{\alpha}\langle\boldsymbol{\sigma}\rangle &= -\bar{\boldsymbol{\Gamma}}^{\alpha\beta}\colon \mathbf{E}^{\beta} - \boldsymbol{\Psi}^{\alpha\beta}.\,\mathbf{P}^{\beta} \\ f^{\alpha}\langle\dot{\boldsymbol{u}}\rangle &= -\bar{\boldsymbol{\Phi}}^{\alpha\beta}.\,\mathbf{P}^{\beta} - \boldsymbol{\Theta}^{\alpha\beta}\colon \mathbf{E}^{\beta} \\ \bar{\boldsymbol{\Gamma}}^{\alpha\beta} &= \left[\boldsymbol{\Gamma}^{\alpha\beta} + \delta^{\alpha\beta} f^{\alpha}(\mathbf{D}^{\alpha} - \mathbf{D}^{0})^{-1}\colon \mathbf{D}^{0}\right] \\ \bar{\boldsymbol{\Phi}}^{\alpha\beta} &= \left[\boldsymbol{\Phi}^{\alpha\beta} + \mathbf{1}^{(2)}\frac{\rho^{0}}{\rho^{\alpha}-\rho^{0}}\delta^{\alpha\beta} f^{\alpha}\right] \end{aligned} \tag{2.100}$$

Equations (2.98) can be averaged and inverted to write the averaged eigenfields in terms of average velocity and stress tensors

$$\begin{aligned} \langle\mathbf{E}\rangle &= \boldsymbol{\Delta}\colon\langle\boldsymbol{\sigma}\rangle + \boldsymbol{\Lambda}.\langle\dot{\boldsymbol{u}}\rangle \\ \langle\mathbf{P}\rangle &= \boldsymbol{\Xi}\colon\langle\boldsymbol{\sigma}\rangle + \boldsymbol{\Omega}.\langle\mathbf{P}\rangle \end{aligned} \tag{2.101}$$

where the expressions for matrices $\boldsymbol{\Delta}, \boldsymbol{\Lambda}, \boldsymbol{\Xi}$, and $\boldsymbol{\Omega}$ are given in appendix B. The averaged consistency conditions (2.95) can now be expressed as

$$\begin{aligned} \langle\boldsymbol{\varepsilon}\rangle &= \bar{\mathbf{D}}\colon\langle\boldsymbol{\sigma}\rangle + \bar{\boldsymbol{S}}^{\mathbf{1}}.\langle\dot{\boldsymbol{u}}\rangle \\ \langle\boldsymbol{p}\rangle &= \bar{\boldsymbol{S}}^{\mathbf{2}}\colon\langle\boldsymbol{\sigma}\rangle + \bar{\boldsymbol{\rho}}.\langle\dot{\boldsymbol{u}}\rangle \end{aligned} \tag{2.102}$$

where

$$\begin{aligned} \bar{\mathbf{D}} &= \mathbf{D}^{0} - \langle\boldsymbol{\Delta}\rangle \\ \bar{\boldsymbol{S}}^{\mathbf{1}} &= -\langle\boldsymbol{\Lambda}\rangle \end{aligned} \tag{2.103}$$

$$\overline{\boldsymbol{S}}^{\boldsymbol{2}} = -\langle \boldsymbol{\Xi} \rangle$$

$$\overline{\boldsymbol{\rho}} = \rho^0 \mathbf{1} - \langle \boldsymbol{\Omega} \rangle$$

where $\overline{\mathbf{D}}$ and $\overline{\boldsymbol{\rho}}$ are the overall effective compliance and density of the composite; and $\overline{\boldsymbol{S}}^{\boldsymbol{1}}$ and $\overline{\boldsymbol{S}}^{\boldsymbol{2}}$ are the coupling terms.

Consider an infinite homogenized elastic solid with periodic microstructure, and seek conditions under which it supports Bloch waves of the following form

$$\begin{aligned} \langle \boldsymbol{\sigma} \rangle(\boldsymbol{x}) &= \langle \boldsymbol{\sigma} \rangle e^{i\boldsymbol{q}.\boldsymbol{x}} \\ \langle \dot{\boldsymbol{u}} \rangle(\boldsymbol{x}) &= \langle \dot{\boldsymbol{u}} \rangle e^{i\boldsymbol{q}.\boldsymbol{x}} \\ \langle \boldsymbol{\varepsilon} \rangle(\boldsymbol{x}) &= \langle \boldsymbol{\varepsilon} \rangle e^{i\boldsymbol{q}.\boldsymbol{x}} \\ \langle \boldsymbol{p} \rangle(\boldsymbol{x}) &= \langle \boldsymbol{p} \rangle e^{i\boldsymbol{q}.\boldsymbol{x}} \end{aligned} \tag{2.104}$$

The averaged field equations can be expressed as

$$\begin{aligned} \boldsymbol{q}.\langle \boldsymbol{\sigma} \rangle &= -\omega \langle \boldsymbol{p} \rangle \\ \boldsymbol{q} \otimes \langle \dot{\boldsymbol{u}} \rangle &= -\omega \langle \boldsymbol{\varepsilon} \rangle \end{aligned} \tag{2.105}$$

These equations are combined with the constitutive equations (2.102) to get

$$\boldsymbol{K}(\boldsymbol{q}, \omega).\langle \dot{\boldsymbol{u}} \rangle = 0 \tag{2.106}$$

For nontrivial solutions to the above equation, the determinant of matrix $\boldsymbol{K}$ should be set equal to zero which produces the dispersion relation of the composite.

Appendix 2A

For a one-dimensional PC the coefficient matrices **Ω, Φ,** and $\boldsymbol{H}$ in equation (2.13) can be expressed as

$$\boldsymbol{\Omega} = \omega^2 \begin{bmatrix} \bar{\rho} & \Delta\rho \dfrac{\sin(\frac{\pi b}{a})}{\pi} & \Delta\rho \dfrac{\sin(\frac{2\pi b}{a})}{2\pi} & \cdots \\ \Delta\rho \dfrac{\sin(\frac{\pi b}{a})}{\pi} & \bar{\rho} & \Delta\rho \dfrac{\sin(\frac{\pi b}{a})}{\pi} & \\ \Delta\rho \dfrac{\sin(\frac{2\pi b}{a})}{2\pi} & \Delta\rho \dfrac{\sin(\frac{\pi b}{a})}{\pi} & \bar{\rho} & \\ \vdots & & & \ddots \end{bmatrix} \tag{2.107}$$

$$\boldsymbol{H} = diag \frac{i}{a}\{Q - 2\pi N, Q - 2\pi(N-1), \dots, Q, \dots, Q + 2\pi N\} \tag{2.108}$$

Matrix **Φ** can be obtained by replacing $\omega^2\bar{\rho}$ in the matrix **Ω** by $\bar{D}$ and $\omega^2\Delta\rho$ by ΔD, respectively. Also the following notation is used

$$\begin{gathered} \Delta\rho = \rho_2 - \rho_1, \quad \Delta D = D_2 - D_1 \\ \bar{\rho} = n_1\rho_1 + n_2\rho_2, \quad \bar{D} = n_1 D_1 + n_2 D_2 \\ n_1 = \tfrac{a-b}{a}, \quad n_2 = \tfrac{b}{a} \end{gathered} \tag{2.109}$$

where ρ_1, ρ_2, D_1, and D_2 are the density and compliance of the first and second phase, respectively.

Appendix 2B

For a two-dimensional PC, the coefficient matrices **Ω, H**, and **Φ** in characteristic equation (2.13) can be expressed as follows. Define

$$I_1 = (\alpha + 1 + M) + (\beta + M)(2M + 1),$$

$$J_1 = (\gamma + 1 + M) + (\delta + M)(2M + 1), \tag{2.110}$$

$$I_2 = I_1 + (2M + 1)^2, \quad J_2 = J_1 + (2M + 1)^2.$$

where $\alpha, \beta, \gamma, \delta = 0, \pm 1, \ldots, \pm M$. The matrix $\mathbf{\Omega}$ can be given as

$$\Omega(I_1, J_1) = \frac{\nu^2}{d} \begin{cases} \dfrac{\theta - 1}{\bar{n}_1 + \bar{n}_2 \theta} \dfrac{m_2 J_1(R)}{2\sqrt{R}} & \text{if } \alpha \neq \gamma \text{ and/or } \beta \neq \delta \\ 1 & \text{if } \alpha = \gamma, \beta = \delta \end{cases} \tag{2.111}$$

$$\Omega(I_2, J_2) = \Omega(I_1, J_1), \quad \Omega(I_1, J_2) = \Omega(I_2, J_1) = 0$$

The matrix $\mathbf{H} = -\bar{\mathbf{H}}^T$ can be expressed as

$$\bar{\mathrm{H}}(I_1, J_1) = -i \begin{cases} Q_1 + 2\pi\gamma & if\ \alpha = \gamma\ and\ \beta = \delta \\ 0 & if\ \alpha \neq \gamma\ or\ \beta \neq \delta \end{cases}$$

$$\bar{\mathrm{H}}(I_2, J_1) = -i \begin{cases} Q_2 + 2\pi\delta n_0 & if\ \alpha = \gamma\ and\ \beta = \delta \\ 0 & if\ \alpha \neq \gamma\ or\ \beta \neq \delta \end{cases} \tag{2.112}$$

$$\bar{H}(I_2, J_2) = \bar{H}(I_1, J_1), \quad \bar{H}(I_3, J_2) = \bar{H}(I_2, J_1), \ \bar{H}(I_1, J_2) = \bar{H}(I_3, J_1) = 0$$

The matrix $\mathbf{\Phi}$ is defined as follows: $\Phi(I_1, J_1)$ can be obtained from equation (2.111) if one replaces $(\theta - 1)/(\bar{n}_1 + \bar{n}_2\theta)$ by $(\gamma_{1111} - 1)/(\bar{n}_1 + \bar{n}_2\gamma_{1111})$ and omits ν^2/d; $\Phi(I_2, J_2)$ can be found from equation (2.111) if one replaces $(\nu^2/d)(\theta - 1)/(\bar{n}_1 + \bar{n}_2\theta)$ by $4(\gamma_{1212} - 1)R_{1212}/(\bar{n}_1 + \bar{n}_2\gamma_{1111})$; $\Phi(I_1, J_3)$ can be obtained from $\Phi(I_2, J_2)$ if one replaces in the latter $4R_{1212}$ and γ_{1212} by R_{1122} and γ_{1122}, respectively; for the other components of matrix $\mathbf{\Phi}$ one has

$$\Phi(I_3, J_1) = \Phi(I_1, J_3) \tag{2.113}$$

$$\Phi(I_3, J_3) = \Phi(I_1, J_1) = \Phi(I_2, J_3) = \Phi(I_3, J_2) = 0.$$

where the following notation is used

$$\nu^2 = \frac{\omega^2 a_1^2 \bar{\rho}}{\bar{C}_{1111}}$$

$$\bar{\rho} = \rho^{(1)}\bar{n}_1 + \rho^{(2)}\bar{n}_2, \quad \bar{C}_{1111} = C_{1111}^{(1)}\bar{n}_1 + C_{1111}^{(2)}\bar{n}_2$$

$$\bar{n}_1 = 1 - \bar{n}_2,\ \bar{n}_2 = \frac{\pi}{4}\frac{b_1 b_2}{a_1 a_2},\ \ \theta = \frac{\rho^{(2)}}{\rho^{(1)}}$$

$$n_2 = \frac{b_1}{a_1},\ m_2 = \frac{b_2}{a_2},\ n_0 = \frac{a_1}{a_2},\ d = \frac{1}{\bar{C}_{1111}\bar{D}_{1111}} \tag{2.114}$$

$$\gamma_{jklm} = \frac{D_{jklm}^{(2)}}{D_{jklm}^{(1)}},\ \ R_{jklm} = \frac{D_{jklm}^{(1)}}{D_{1111}^{(1)}}$$

$$P = (\alpha - \gamma)^2 + \left[(\beta - \delta)\frac{m_2}{n_2}\right]^2$$

$$\bar{D}_{1111} = D_{1111}^{(1)}\bar{n}_1 + D_{1111}^{(2)}\bar{n}_2$$

where, the superscript $^{(i)}$ over a quantity indicates the corresponding value for the material number i (i=1, 2); with i=1 indicating the matrix and i=2 indicating the inclusion.

Appendix 2C

For a three-dimensional PC, the coefficient matrices $\mathbf{\Omega}, \mathbf{H}$, and $\mathbf{\Phi}$ in characteristic equation (2.13) can be expressed as

$$\boldsymbol{H} = \begin{bmatrix} \mathcal{H}_1 & \mathcal{H}_2 & \mathcal{H}_3 & 0 & 0 & 0 \\ 0 & \mathcal{H}_1 & 0 & \mathcal{H}_2 & \mathcal{H}_3 & 0 \\ 0 & 0 & \mathcal{H}_1 & 0 & \mathcal{H}_2 & \mathcal{H}_3 \end{bmatrix} \tag{2.115}$$

where $\mathcal{H}_1$, $\mathcal{H}_2$ and $\mathcal{H}_3$ are $(2M+1)^3 \times (2M+1)^3$ matrices defined as: for $\alpha = \delta, \beta = \mu$ and $\gamma = \tau$, and with $Q_j = q_j a_j$,

$$\begin{gathered} \mathcal{H}_1(I_1, J_1) = -i(Q_1 + 2\pi\alpha), \;\; \mathcal{H}_2(I_1, J_1) = -i(Q_2 + 2\pi\beta)n_0 \\ \mathcal{H}_3(I_1, J_1) = -i(Q_3 + 2\pi\gamma)m_0 \end{gathered} \tag{2.116}$$

For $\alpha \neq \delta, \beta \neq \mu$ and $\gamma \neq \tau$

$$\mathcal{H}_1(I_1, J_1) = \mathcal{H}_2(I_1, J_1) = \mathcal{H}_3(I_1, J_1) = 0 \tag{2.117}$$

where $I_1 = (\alpha + 1 + M') + (\beta + M)(2M+1) + (\gamma + M)(2M+1)^2; \;\; \delta, \mu, \tau = 0, \pm 1, \pm 2, \ldots, , \pm M$. Also, matrices $\boldsymbol{\Omega}$ and $\boldsymbol{\Phi}$ can be given by

$$\boldsymbol{\Omega} = \begin{bmatrix} \overline{\boldsymbol{\Omega}} & 0 & 0 \\ 0 & \overline{\boldsymbol{\Omega}} & 0 \\ 0 & 0 & \overline{\boldsymbol{\Omega}} \end{bmatrix} \tag{2.118}$$

and

$$\boldsymbol{\Phi} = \begin{bmatrix} \boldsymbol{\Delta}_{1111} & \mathbf{0} & \mathbf{0} & \boldsymbol{\Delta}_{1122} & \mathbf{0} & \boldsymbol{\Delta}_{1133} \\ \mathbf{0} & 4\boldsymbol{\Delta}_{1212} & \mathbf{0} & \mathbf{0} & \mathbf{0} & \mathbf{0} \\ \mathbf{0} & \mathbf{0} & 4\boldsymbol{\Delta}_{1313} & \mathbf{0} & \mathbf{0} & \mathbf{0} \\ \boldsymbol{\Delta}_{1122} & \mathbf{0} & \mathbf{0} & \boldsymbol{\Delta}_{2222} & \mathbf{0} & \boldsymbol{\Delta}_{2233} \\ \mathbf{0} & \mathbf{0} & \mathbf{0} & \mathbf{0} & 4\boldsymbol{\Delta}_{2323} & \mathbf{0} \\ \boldsymbol{\Delta}_{1133} & \mathbf{0} & \mathbf{0} & \boldsymbol{\Delta}_{2233} & \mathbf{0} & \boldsymbol{\Delta}_{3333} \end{bmatrix} \tag{2.119}$$

where $\overline{\boldsymbol{\Omega}}$ and $\boldsymbol{\Delta}_{ijkl}$ are $(2M+1)^3 \times (2M+1)^3$ matrices defined in the following manner for composites with ellipsoidal inclusions

$$\bar{\mathbf{\Omega}}(I_1,J_1)=\begin{cases}1 & if\ \ \alpha=\delta,\beta=\mu,\gamma=\tau;\\ \left(\frac{\pi}{2}\right)^{3/2}\frac{\theta-1}{\bar{n}_1+\bar{n}_2\theta}\frac{n_2m_2l_2J_{3/2}(R)}{R^{3/2}} & \text{otherwise}\end{cases} \tag{2.120}$$

where $J_{3/2}$ is a Bessel function of the first kind of order 3/2 and its argument R is given by

$$R=\pi\left[{n_2}^2(\alpha-\delta)^2+{m_2}^2(\beta-\mu)^2+{l_2}^2(\gamma-\tau)^2\right]^{1/2} \tag{2.121}$$

For $I_1\neq J_1$, $\mathbf{\Delta}_{ijkl}$ is obtained if one substitutes $(\gamma_{ijkl}-1)R_{ijkl}/(\bar{n}_1+\bar{n}_2\theta\gamma_{1111})$ for $(\theta-1)/(\bar{n}_1+\bar{n}_2\theta)$ in the expression for $\bar{\mathbf{\Omega}}(I_1,J_1)$, and for $I_1=J_1$ one has

$$\mathbf{\Delta}_{ijkl}=\frac{(\bar{n}_1+\bar{n}_2\theta\gamma_{ijkl})R_{ijkl}}{(\bar{n}_1+\bar{n}_2\theta\gamma_{1111})} \tag{2.122}$$

The following notation is used in the above expressions

$$\begin{gathered}\nu^2=\frac{\omega^2{a_1}^2\bar{\rho}}{\bar{C}_{1111}},\ \ \bar{\rho}=\rho^{(1)}\bar{n}_1+\rho^{(2)}\bar{n}_2,\qquad \bar{C}_{1111}=C^{(1)}_{1111}\bar{n}_1+C^{(2)}_{1111}\bar{n}_2\\ \bar{n}_1=1-\bar{n}_2,\ \ \bar{n}_2=\frac{\pi b_1b_2b_3}{6a_1a_2a_3},\ \ \theta=\frac{\rho^{(2)}}{\rho^{(1)}},\ \ n_2=\frac{b_1}{a_1},\quad m_2=\frac{b_2}{a_2}\\ l_2=\frac{b_3}{a_3},\quad n_0=\frac{a_1}{a_2},\quad m_0=\frac{a_1}{a_3},\ \ \gamma_{jklm}=\frac{D^{(2)}_{jklm}}{D^{(1)}_{jklm}}\\ R_{jklm}=\frac{D^{(1)}_{jklm}}{D^{(1)}_{1111}},\ \ d=\frac{1}{\bar{C}_{1111}\bar{D}_{1111}},\bar{D}_{1111}=D^{(1)}_{1111}\bar{n}_1+D^{(2)}_{1111}\bar{n}_2\end{gathered} \tag{2.123}$$

Appendix 2D

For a two-dimensional PC the coefficient tensors $\boldsymbol{\Phi}$, $\boldsymbol{\Theta}$, $\boldsymbol{\Psi}$, and $\boldsymbol{\Gamma}$ in equation (2.92) can be given in component form as

$$\Phi_{pj} = \frac{\omega^2}{\rho^0}\left[\frac{c_1^2 - c_2^2}{(\omega^2 - c_1^2\zeta^2)(\omega^2 - c_2^2\zeta^2)}\zeta_p\zeta_j + \frac{1}{\omega^2 - c_2^2\zeta^2}\delta_{pj}\right]$$

$$\Theta_{pij} = \frac{-\omega}{2}\left[\frac{2c_2^2(c_1^2 - c_2^2)}{(\omega^2 - c_1^2\zeta^2)(\omega^2 - c_2^2\zeta^2)}\zeta_i\zeta_p\zeta_j + \frac{c_1^2 - 2c_2^2}{\omega^2 - c_1^2\zeta^2}\delta_{ij}\zeta_p + \frac{c_2^2}{\omega^2 - c_2^2\zeta^2}(\delta_{pj}\zeta_i + \delta_{pi}\zeta_j)\right]$$

$$\Psi_{ijp} = \frac{-\omega}{2}\left[\frac{2c_2^2(c_1^2 - c_2^2)}{(\omega^2 - c_1^2\zeta^2)(\omega^2 - c_2^2\zeta^2)}\zeta_i\zeta_p\zeta_j + \frac{c_1^2 - 2c_2^2}{\omega^2 - c_1^2\zeta^2}\delta_{ij}\zeta_p + \frac{c_2^2}{\omega^2 - c_2^2\zeta^2}(\delta_{pj}\zeta_i + \delta_{pi}\zeta_j)\right] \tag{2.124}$$

$$\Gamma_{ijpq} = C^0_{ijmn}S_{mnkl}C^0_{klpq}$$

$$S_{mnkl} = \frac{1}{\rho^0}\left[\frac{1}{(\omega^2 - c_2^2\zeta^2)}(\delta_{nk}\zeta_m\zeta_l + \delta_{nl}\zeta_m\zeta_k + \delta_{ml}\zeta_n\zeta_k + \delta_{mk}\zeta_n\zeta_l) - \frac{c_1^2 - 2c_2^2}{2c_2^2(3c_1^2 - 4c_2^2)}\delta_{mn}\delta_{kl} + \frac{c_1^2 - c_2^2}{(\omega^2 - c_1^2\zeta^2)(\omega^2 - c_2^2\zeta^2)}\zeta_m\zeta_k\zeta_n\zeta_l + \frac{1}{4c_2^2}(\delta_{mk}\delta_{nl} + \delta_{ml}\delta_{nk})\right]$$

where $c_1 = \sqrt{(\lambda_0' + 2\mu_0)/\rho^0}$ is the longitudinal wave velocity and $c_2 = \sqrt{\mu_0/\rho^0}$ is the shear wave velocity.

Chapter 3

Experimental verification of band-gap in periodic elastic composites

3.1. Introduction

Propagation of stress waves in PCs is prohibited within band-gaps, where incoming stress waves get effectively reflected. This feature can be used to design acoustic filters, noise insulators, and vibrationless environments. In this chapter, band-gap in one- and two-dimensional PCs is investigated experimentally. Mixed variational formulation is used to design samples with band-gaps at frequencies convenient to conduct experiment. Samples are fabricated and their transmission coefficient is measured. Experimental data are compared with theoretical results for verification of the band structure. In addition, controlling the band structure of PCs by changing the ambient temperature is studied. The essential idea is to fabricate a PC with constituent materials which has temperature dependent material properties. As temperature is changed, such a composite exhibits a band structure which changes with the change in temperature. Ultrasound measurements are performed over a range of frequency at different

temperatures. Experimental transmission spectrum at each temperature is compared with the theoretical band structure for verification.

In the recent years, there have been many efforts for tuning the band structure of PCs. Ruzzene and Baz [46] used shape memory alloys to make a one-dimensional PC and showed that by changing the thermal activation of a shape memory alloy, the width and location of the band-gaps can be modified. Goffaux and Vigneron [47] tuned the band-gaps of a two-dimensional PC made of square rods by changing the geometry of the system. They showed that by increasing the rotation angle of the square rods with respect to the lattice orientation, band-gaps can be widened. Zou et al. [48] showed that band-gaps of two-dimensional PCs consisting of rectangular piezoelectric ceramics placed in epoxy matrix can be controlled with changing the filling fraction and the length to width ratio of the rods. Wu et al. [49] used dielectric elastomer layers in a one-dimensional periodic composite consisting of layers of aluminum and PMMA to make a tunable acoustic filter. They showed that the band structure of the composite can be controlled by changing the applied electric voltage on the dielectric layers. Zou et al. [50] showed that in-plane band-gaps in two-dimensional PCs made of piezoelectric inclusions can be tuned by controlling the propagation of out-of-plane elastic waves. They realized that the width and starting frequency of band-gaps at high frequency range can be controlled by the filling fraction and the composite's piezoelectricity.

3.2. Ultrasonic setup

Figure 3-1(a, b) show a schematic drawing and a photograph of the ultrasonic setup used in this study. A wave packet envelop made of 10 sine waves at the carrier

frequency, f, multiplied by a half-period of another sinusoidal of 1/20 carrier frequency is generated through the wave generator and is sent to the amplifier [51] (see Figure 3-1 (c))

$$u(0,t) = Asin(2\pi ft)sin(2\pi ft/20) \quad \text{where } 0 < t < 10/f \tag{3.1}$$

The amplified signal is sent through a contact piezoelectric transducer to the sample and is received by a similar transducer on the other side. The transmitted signal is received and stored by oscilloscope. Couplant is used between the transducers and the sample for better transmission of the signal at the interfaces. The transducers used in this study and their specifications are shown in Table 3-1.

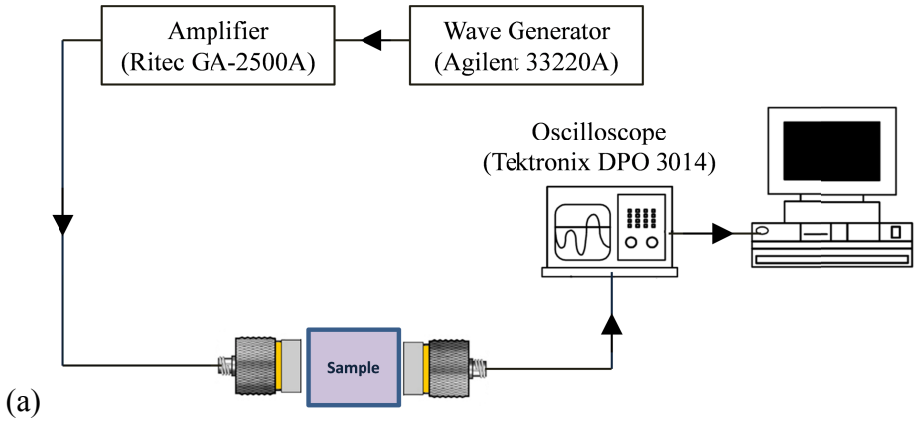

Figure 3-1: (a) Schematic drawing and (b) photograpgh of the ultrasonic setup, and (c) the shape of the incident wave packet

Table 3-1: Transducers used in the ultrasonic measurements

	Type	Frequency (MHz)	Diameter (inch)
Panametric V103	Longitudinal	1.0	0.5
Panametric V153	Shear	1.0	0.5
NDT CHRFO18	Longitudinal	1.0	1.0

In order to design a PC, the wave velocity and attenuation in each constituent material is measured experimentally. Two tests are performed on two samples with different thicknesses as shown in Figure 3-2(a). Assume the arrival time of the signals transmitted through each sample is t_1 and t_2 with their amplitudes being A_1 and A_2, respectively, as shown in Figure 3-2(b). The longitudinal wave velocity, c_L, and attenuation coefficient per unit thickness, α, can be calculated as

$$c_L = \frac{d_2 - d_1}{\Delta t} \tag{3.2}$$

$$\alpha = \frac{1}{d_2 - d_1} \ln\left(\frac{A_1}{A_2}\right) \tag{3.3}$$

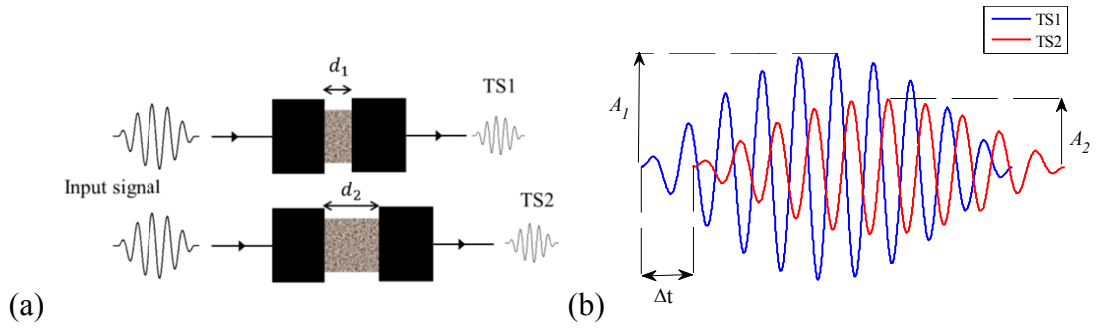

Figure 3-2: (a) Two samples with different thicknesses between transducers and (b) transmitted signals through the samples

where $\Delta t = t_2 - t_1$ is the difference between the arrival time of the signals through the samples with thickness d_1 and d_2. It can be shown that for a homogenous linear viscoelastic material the real and imaginary parts of the complex modulus can be expressed as [52]

$$E' = \frac{\rho c_L^2 (1 - r^2)}{(1 + r^2)^2} \tag{3.4}$$

$$E'' = \frac{2\rho c_L^2 r}{(1 + r^2)^2} \tag{3.5}$$

where the dimensionless parameter *r* is given by:

$$r = \frac{\alpha c_L}{\omega} \tag{3.6}$$

3.3. One-dimensional steel/polyurea periodic composite

3.3.1. Sample

A one-dimensional PC made of periodic layers of steel and polyurea (PU) is designed and fabricated. The thicknesses of the steel and polyurea layers are given by $t_{st} = 1.15$ mm and $t_{PU} = 1$ mm, respectively. The properties of the constituent materials are given by $c_{st} = 5130\, m/s$, $\rho_{\text{st}} = 7820\ \text{kg}/m^3$, $c_{PU} = 1693\, m/s$, and $\rho_{\text{PU}} = 1100\ \text{kg}/m^3$ for the wave velocity and density of steel and polyurea (at 20 ^{o}C), respectively. A sample made of two unit cells of the steel/PU PC is fabricated. The frequency of the incident wave is changed to sweep over a range of frequency and the transmitted signal is measured. Figure 3-3 show a drawing of the steel/PU sample.

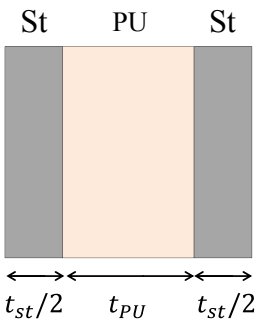

Figure 3-3: Unit cell of the one-dimensional steel/PU sample

3.3.2. Results

Figure 3-4 shows the theoretical band structure of the steel/PU sample at 20 ^{o}C. It can be seen that the first two band-gaps of the composite occur at 251-811 kHz and 892-1588 kHz, respectively. Figure 3-5 shows the normalized amplitude of the transmitted longitudinal wave through the sample. Experimental results are normalized with respect to amplitude of the transmitted wave in a transducer to transducer test. It can be seen that the theoretical and experimental data are in good agreement. However, it is observed that the pass bands are slightly wider than the theoretical calculations. For example the theoretical second pass band occurs at 811-892 kHz, while the experimentally observed second pass band occurs at 797-907 kHz. There are at least two possibilities for this difference between the theoretical calculations and experimental results (i) material properties of the constituents slightly change with frequency and (ii) the sample is in cylindrical shape which results in dispersion while the one-dimensional calculations do not take this into account.

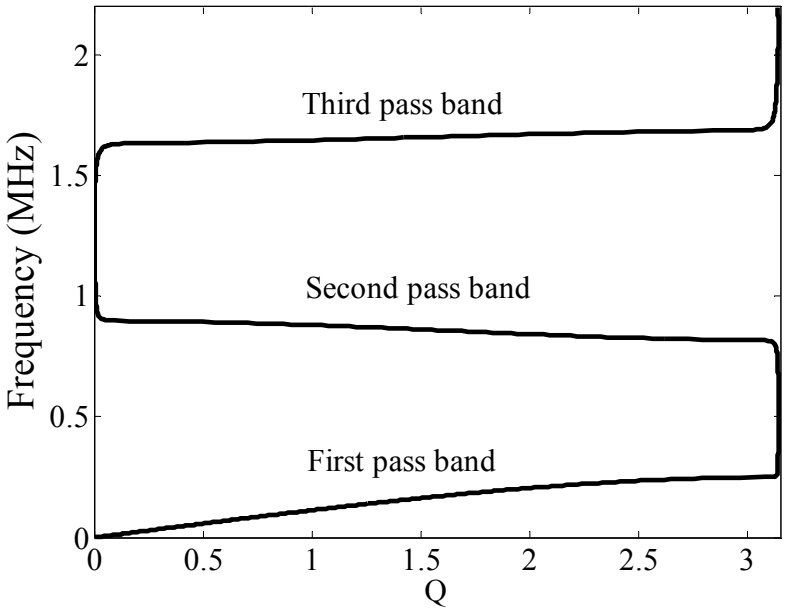

Figure 3-4: Theoretical dispersion curve for the one-dimensional steel/PU sample

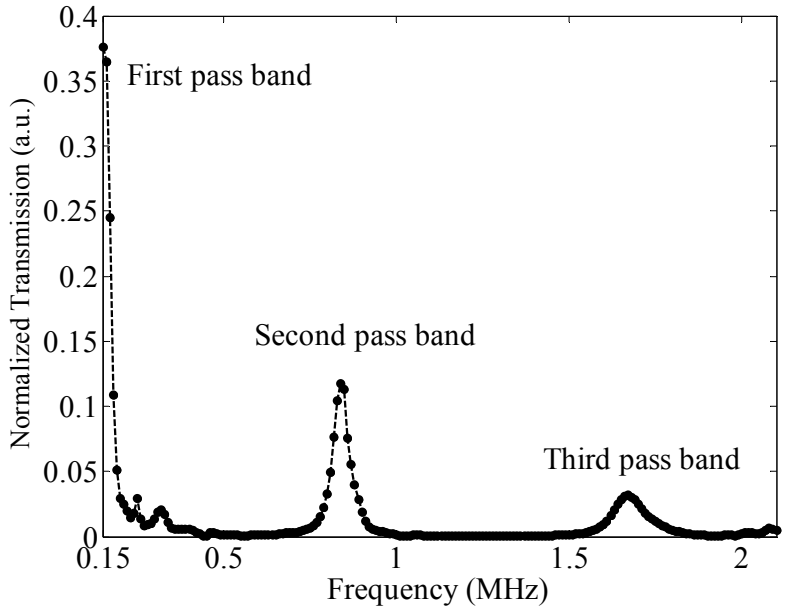

Figure 3-5: Normalized transmission through the one-dimensional steel/PU sample

3.4. Two-dimensional brass/epoxy periodic composite

3.4.1. Sample

A two-dimensional PC made of periodic arrays of cylindrical brass rods embedded in the epoxy matrix is designed and fabricated. The unit cell of the sample is square with sides being a=1.5 mm long and diameter of the rods being d=0.8 mm (see Figure 3-6(a)). The Young modulus, Poisson ratio, and density of epoxy and brass are given by $E_{ep} = 5.1\,GPa, \nu_{\text{ep}} = 0.35,\ \rho_{\text{ep}} = 1090\ kg/m^3,\ E_{br} = 110\,GPa,\ \nu_{br} = 0.35,\ \rho_{br} = 8500\ kg/m^3$, respectively. Figure 3-6(b) shows a photograph of 4 unit cells of the sample.

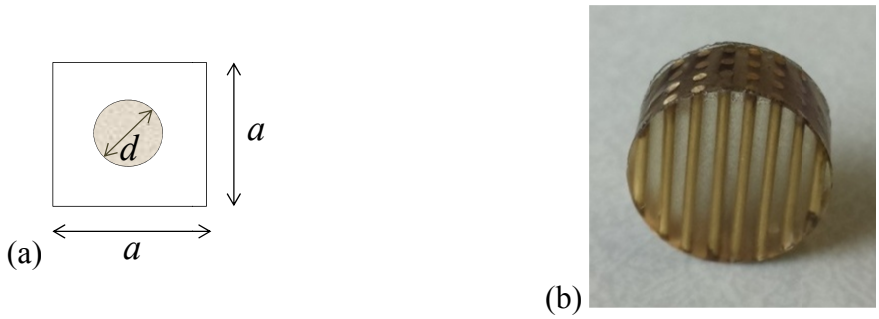

Figure 3-6: (a) Unit cell of the two-dimensional brass/epoxy periodic composite and (b) a photograph of the sample

3.4.2. Results

Figure 3-7 shows the theoretical band structure for the two-dimensional brass/epoxy sample. Figure 3-8 and Figure 3-9 show the mode shapes for the first mode, acoustic SV-mode, and the second mode, acoustic P-mode, at Q=(1, 0), respectively. Third and fourth modes are quasi-shear; while fifth and sixth modes are longitudinal and quasi-longitudinal modes, respectively. It can be seen that there is a longitudinal band-

gap at 442-763 kHz; while for the SV-waves, the first band-gap occurs at 242-434 kHz and the second band-gap occurs at 535-761 kHz.

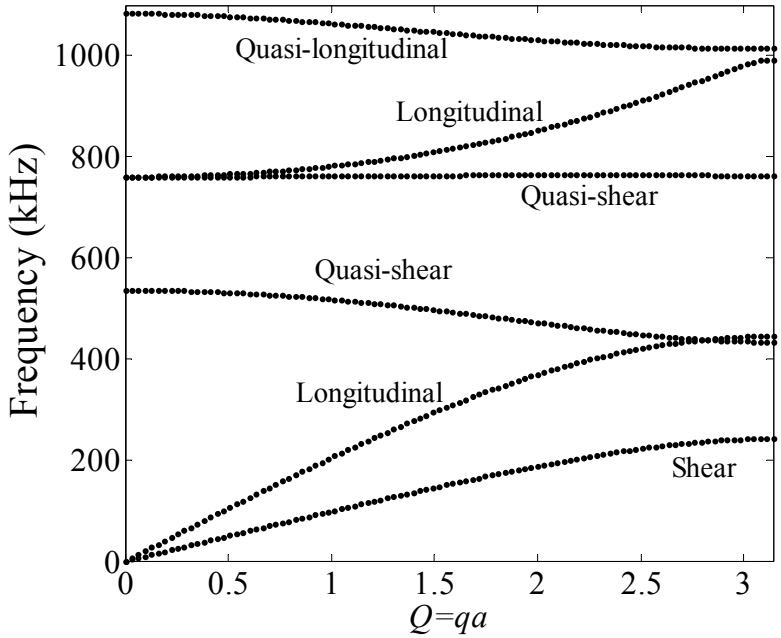

Figure 3-7: Theoretical dispersion curve for the two-dimensional brass/epoxy sample

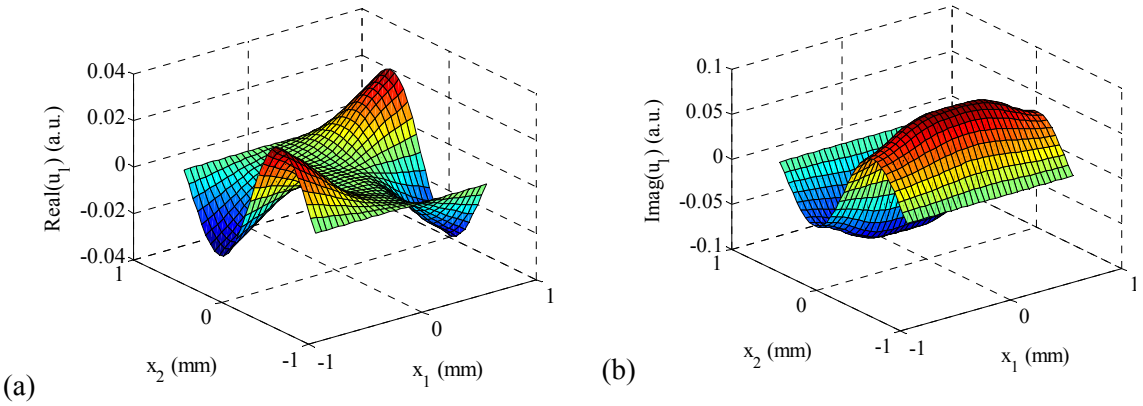

(a) (b)

Figure 3-8: Displacement mode shapes of the two-dimensional brass/epoxy PC for acoustic SV-mode at Q=(1,0) (a) $real(u_1)$, (b) $imag(u_1)$

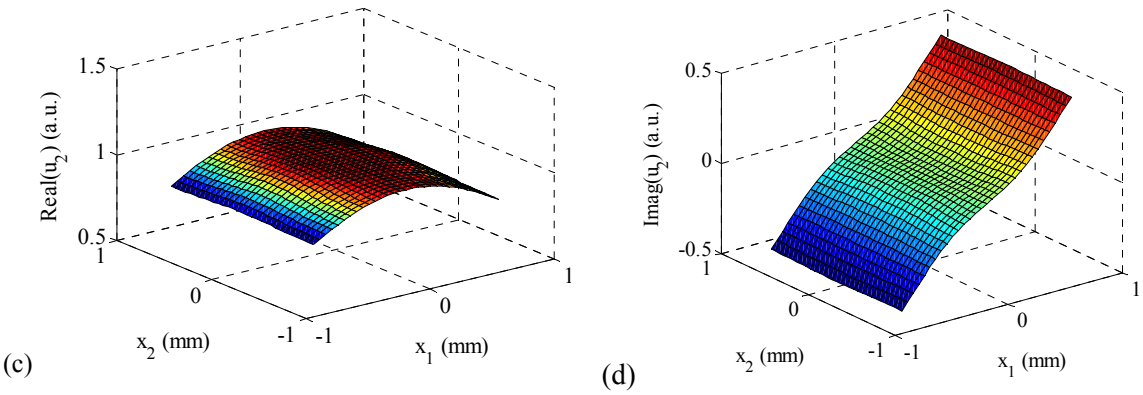

Figure 3-8: Displacement mode shapes of the two-dimensional brass/epoxy PC for acoustic SV-mode at Q=(1,0), continued (c) $real(u_2)$, (d) $imag(u_2)$

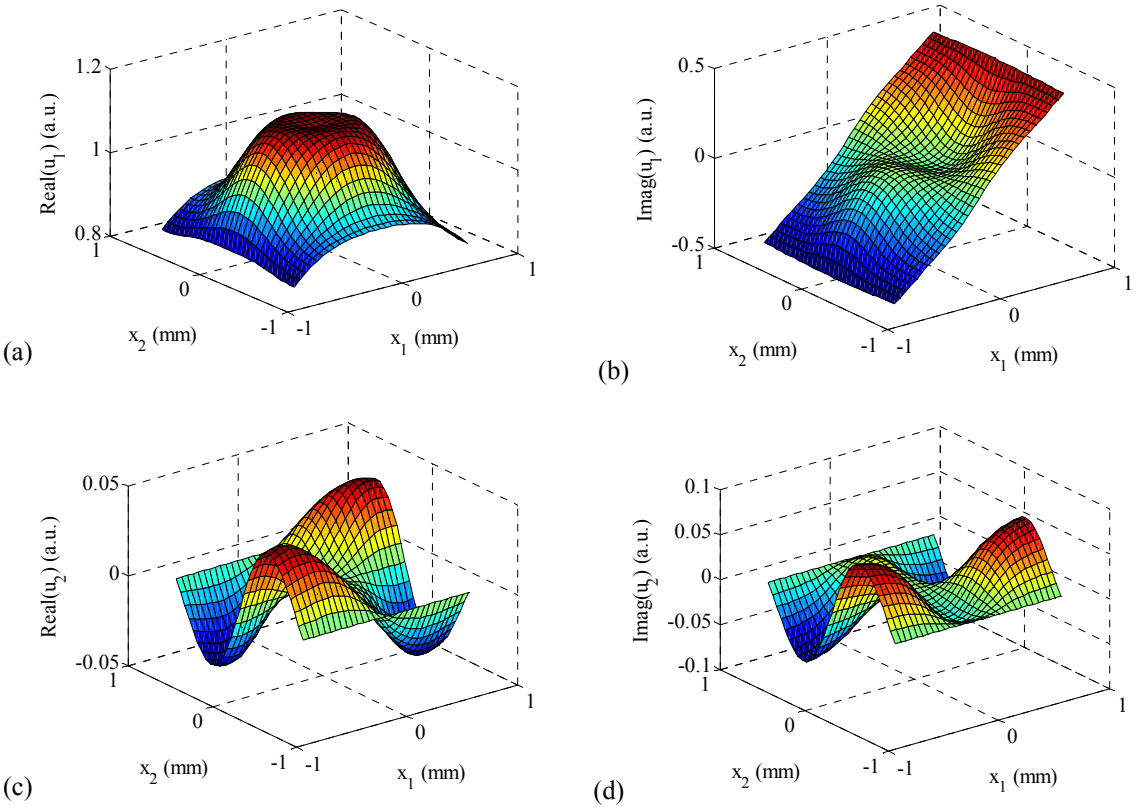

Figure 3-9: Displacement mode shapes of the two-dimensional brass/epoxy PC for acoustic P-mode at Q=(1,0) (a) $real(u_1)$, (d) $imag(u_1)$, (c) $real(u_2)$, and (d) $imag(u_2)$

Normalized amplitude of the transmitted wave as a function of frequency is shown in Figure 3-10(a) and Figure 3-11(a) for P-wave and SV-wave, respectively. The

attenuation in the sample is also calculated and shown in Figure 3-10(b) and Figure 3-11(b) for P-wave and SV-wave, respectively. It can be observed that there is a longitudinal band-gap at 423-695 kHz which is in close agreement with theoretical prediction. For the shear waves, the first and second band-gaps are observed at 222-347 kHz and 481-634 kHz, respectively. Although, the location of the first SV band-gap is in good agreement with theoretical calculations, due to higher dissipation of shear waves in the epoxy at high frequencies, the transmitted SV-wave is small above 600 kHz and it is difficult to make any meaningful observation. Several local peaks are observed in Figure 3-11 above 600 kHz which could probably be due to the mixed modes. Also, it can be observed that for both longitudinal and shear waves the beginning of the band-gaps are slightly shifted to lower frequencies. Although, the bandwidth of the P-wave band-gap matches the theoretical calculations, for the SV-wave the experimental first band-gap bandwidth is slightly less than the theoretical prediction. There are at least two possibilities for this difference between the theoretical calculations and experimental results (i) material properties of the constituents slightly change with frequency and (ii) the sample is in cylindrical shape which results in dispersion in propagation of the waves while theoretical calculations do not take this into account.

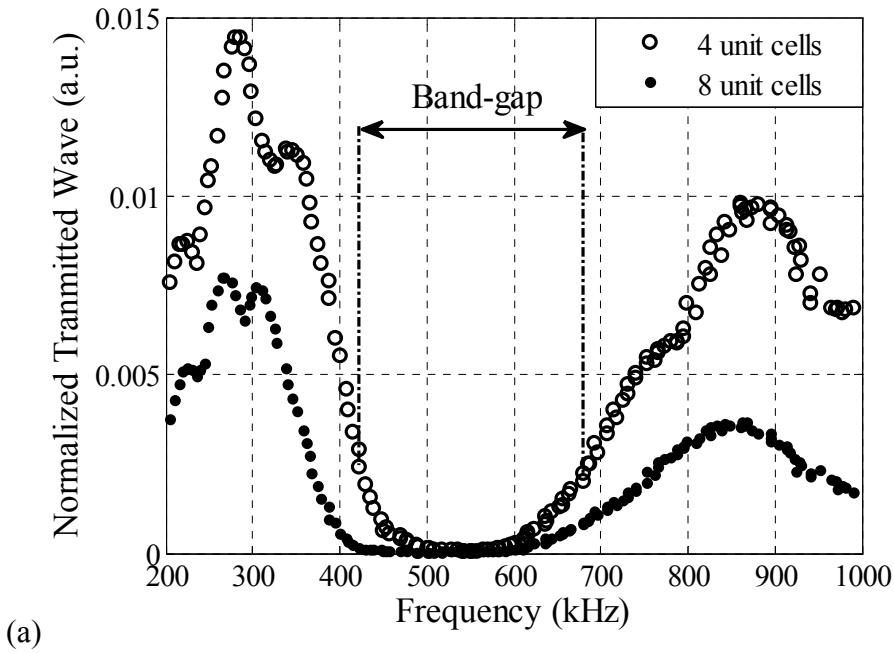

(a)

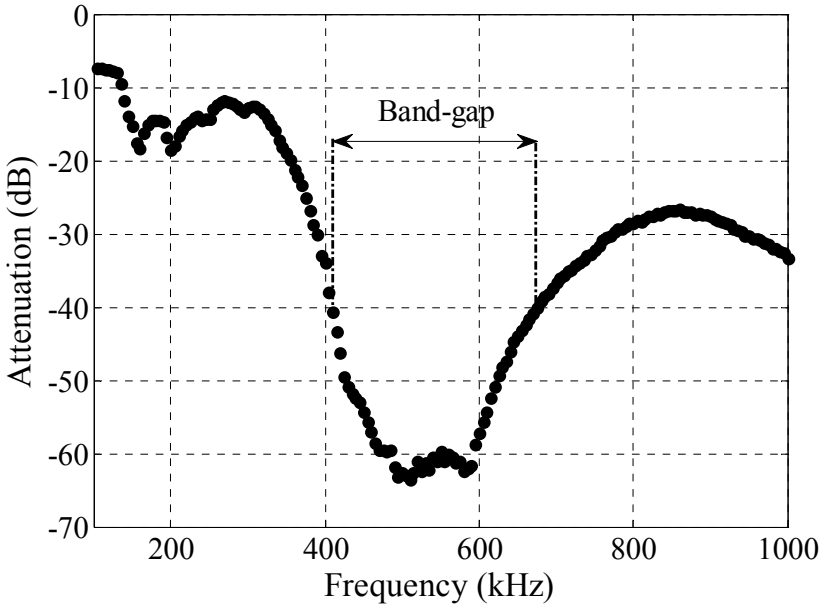

(b)

Figure 3-10: (a) Normalized transmission and (b) attenuation of the P-wave through the two-dimensional brass/epoxy sample

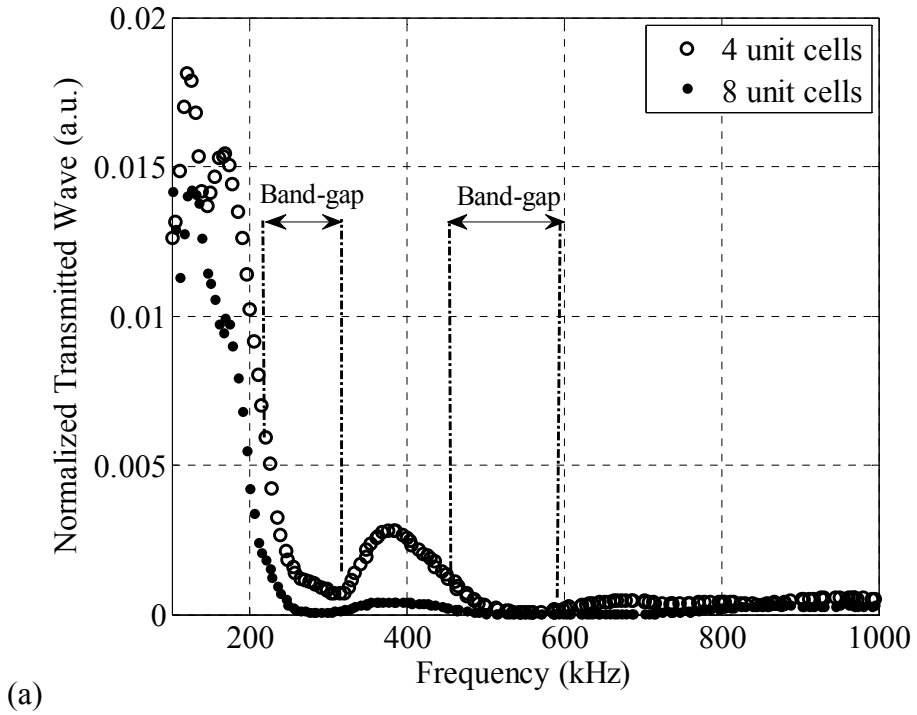

(a)

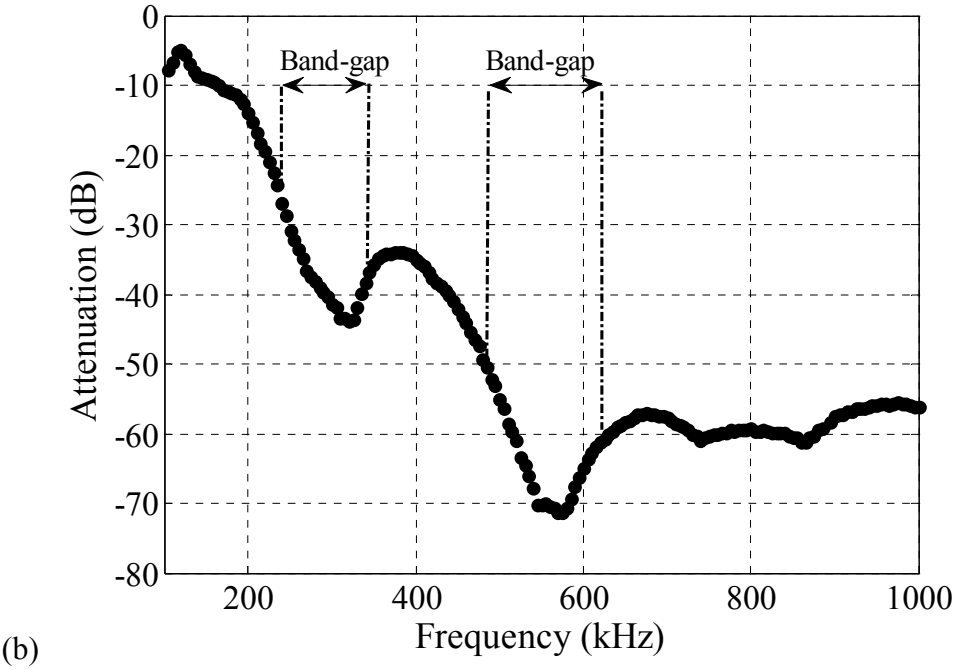

(b)

Figure 3-11: (a) Normalized transmission and (b) attenuation of the SV-wave through the two-dimensional brass/epoxy sample

3.5. Temperature tuning of band structure of PCs

Controlling the band structure of PCs by changing the ambient temperature is investigated experimentally. The essential idea is to fabricate a periodic composite with constituent materials which have temperature dependent material properties. As temperature is changed, such a composite exhibits a band structure which changes with the change in temperature. A two-phase composite with periodic layers of polyurea and steel is designed and fabricated. Measurements are performed over a range of frequency at different temperatures. Experimental transmission spectrum at each temperature is compared with the theoretical band structure for verification.

3.5.1. Test procedure and results

The sample designed for this study is a one-dimensional PC made of steel and polyurea with dimensions and properties given in section 3.3.1. The longitudinal wave velocity of polyurea changes with temperature which is measured experimentally. The sample and transducers are placed in a temperature control chamber to keep their temperature constant during the measurements. The transducers used here are CHRFO18 NDT Systems transducers with nominal diameter of 1 in and nominal center frequency 1.0 MHz. Figure 3-12 shows the longitudinal wave velocity and attenuation coefficient of polyurea as a function of temperature at 1.0 MHz. The real and imaginary parts of the modulus of polyurea are calculated and used to calculate the theoretical band structure of the steel/PU sample at each temperature. In order to study the changes in the band structure, the sample is tested at different temperatures from -20 ^{o}C to 60 ^{o}C with a step size of 20 ^{o}C. At each step the system is left for 15 minutes to reach the state of thermal

equilibrium. At each temperature, ultrasonic measurements are performed over the frequency range from 0.15 to 2.2 MHz and the transmitted signal is recorded.

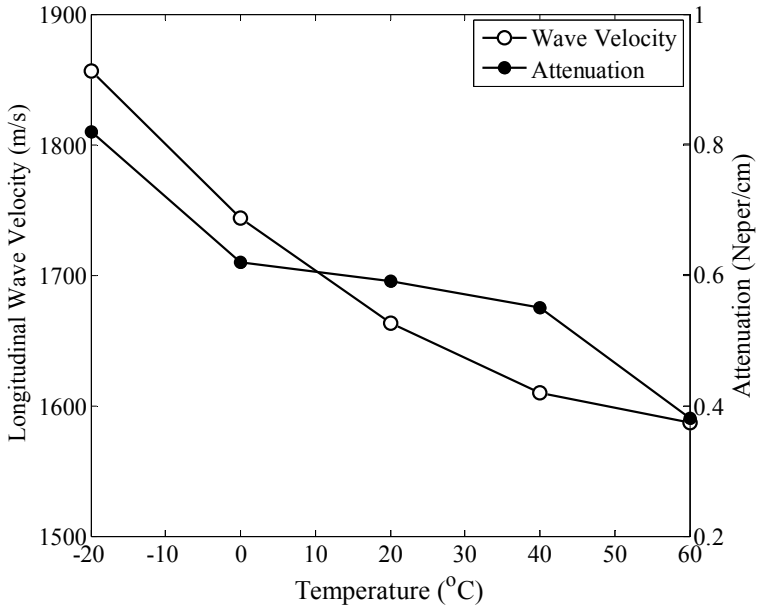

Figure 3-12: Longitudinal wave velocity and attenuation coefficient per unit thickness of polyurea as a function of temperature at 1.0 MHz

Figure 3-13 shows the normalized amplitude of the transmitted waves as a function of frequency through two unit cells of the sample at different temperatures. In the frequency range that measurements are done, the first three pass bands of the composite are captured. It is observed that as the temperature is changed from -20 ^{o}C to 60 ^{o}C the band structure changes significantly. Figure 3-14 shows the comparison of temperature dependent experimental and theoretical frequencies at the beginning of the first pass band (f_1^{ex}, f_1^{th}) as well as experimental and theoretical frequencies at the center of the second and third pass bands ($f_2^{ex}, f_2^{th}, f_3^{ex}, f_3^{th}$). It can be seen that the experimental results match well with the theoretical calculations. Furthermore, it is

observed that the value of the transmitted signal at higher pass bands is smaller compared to lower pass bands, which is due to higher viscous dissipation at higher frequencies. Also, the first three modes move to lower frequencies when the temperature is increased. This is attributed to the reduction in the elastic stiffness of polyurea as the temperature is increased. It can be seen that the difference between the theoretical and experimental results is more significant at higher frequencies compared to lower frequencies. The main reason for this difference is possibly due to higher dispersion at higher frequencies.

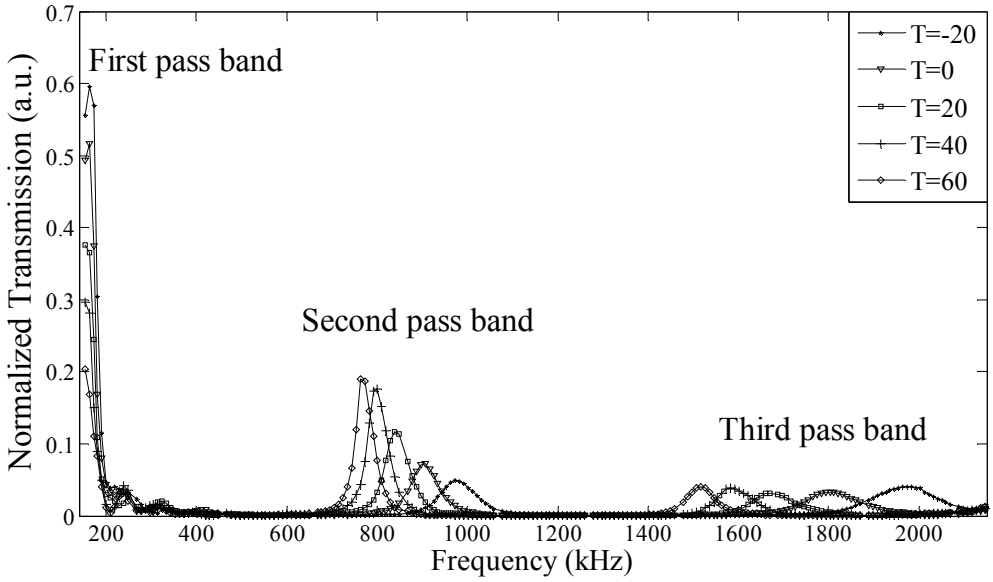

Figure 3-13: Normalized amplitude of transmitted wave through 2 unit cells of the PU/steel sample as a function of frequency at different temperatures

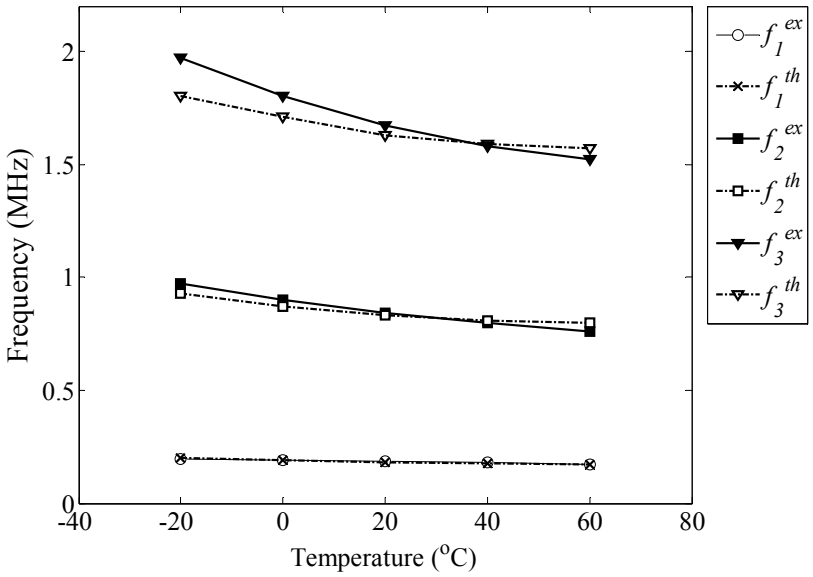

Figure 3-14: Comparison of the experimental and theoretical frequency at the end of the first pass band as well as at the center of the second and third pass bands in the PU/steel sample at different temperatures

3.6. Summary

Band-gap in one- and two-dimensional periodic elastic composites is investigated experimentally. Mixed variational formulation is used to design samples with band-gaps at frequencies convenient to conduct experiment. A one-dimensional PC made of layers of polyurea and steel is fabricated and longitudinal ultrasound measurements are performed. The transmission coefficient is measured and the results are compared with theoretical band structure. Furthermore, a two-dimensional PC made of epoxy matrix with brass rod inclusions is fabricated and longitudinal and shear ultrasound test are performed. The transmission coefficients are measured and the results are compared with theoretical band structure and good agreement is observed.

Furthermore, controlling the band structure of PCs by changing the ambient temperature is studied. Ultrasonic measurements are performed at different temperatures on a sample made of periodic layers of steel and polyurea. Temperature dependent elastic properties of polyurea are measured experimentally and used to calculate the band structure of the steel/PU sample. It is observed that the calculated band structures are in good agreement with the experimental results at different temperatures. This shows tunable acoustic filters can be designed at a target frequency with a desired bandwidth through reverse engineering once the corresponding properties are identified using here proposed experimental tool.

Chapter 4

Design and experimental evaluation of PCs with minimal reflection and maximal attenuation

4.1. Introduction

Stress waves can be manipulated through microstructural design of PCs to achieve a desired elastodynamic response. In this chapter, dynamic homogenization is used to design the microstructure of a one-dimensional PC to match its acoustic impedance with impedance of a homogenous medium. As a result, the reflection of stress waves at the interface of the two impedance matched media becomes zero. For experimental verification, samples are fabricated and ultrasound tests are performed to measure the reflection coefficient. Theoretical reflection coefficient is compared with the experimental values for evaluation of the theoretical calculations. In addition, a one-dimensional metamaterial is designed in order to make a composite with both high stiffness-to-density ratio and high attenuation coefficient. Samples are fabricated and

attenuation coefficients are measured at different frequencies. The experimental attenuation coefficient is compared with theoretical values for verification.

Acoustic impedance matching in ultrasonic transducers has been of great interest due to the importance of efficient power transmission from the transducer to sample [53, 54]. When the acoustic impedance of two adjacent media is matched, the reflection of incoming acoustic waves at their interface becomes zero. Different techniques have been used to design materials for acoustic impedance matching [53, 54, 55, 56]. Quarter wavelength transformer has been conventionally used to design ultrasonic transducers for better energy transmission to the sample [53]. In this method a matching layer with thickness equal to ¼ of its wavelength at the frequency of interest is designed to be placed between the piezoelectric element and the test sample. Tapered impedance matching [55, 56] was later developed for increasing acoustic energy transmission. In this method a composite is made from many closely packed microrods with smooth continuous transition of effective impedance which increases the energy transfer from the transducer and a test sample. A microstructured porous aluminum [57] was also developed for matching the acoustic impedance between the transducer active element and the test sample. Using this technique the microstructure of porous aluminum can be designed with varying the porosity of the layer to control its acoustic impedance.

Acoustic metamaterials are highly attenuative near the resonance frequency. This feature can be used to make materials with tunable attenuation coefficient. Liu et al [1] designed a three-dimensional sonic metamaterial and showed that near the resonance frequencies the metamaterial behaves like a medium with effective negative stiffness. Their experimental results show that at the resonance frequencies the transmission

coefficient is very small due to attenuation induced by local resonance. Ho et al. [27] used several locally resonant materials with different resonance frequencies and showed that each layer vibrates like an independent unit. Their results show significant drop in transmission coefficient at resonance frequencies. Cheng et al. [28] designed a one-dimensional ultrasonic metamaterial with both effective density and effective bulk modulus simultaneously negative. They found the transmission coefficient using acoustic transmission line method (ATLM), finite element method, and experimental measurement and observed a substantial drop in transmission spectrum around the resonance frequency.

Elastic/acoustic noise is undesirable in many applications and isolating mechanical systems from external noise is generally necessary for their robust performance. But, an inherent limitation in properties of existing engineering materials is that increase in the attenuation coefficient usually appears at the expense of decrease in their stiffness. For example, polymers have high attenuation coefficient while they have low stiffness; whereas, metals have high stiffness but low attenuation coefficient. Furthermore, at low frequencies (i.e. a few tens of kHz), the wavelength in materials can become very large and large structures are needed for stress wave attenuation. Therefore, design and development of stiff materials with high attenuation coefficient at low frequencies is an engineering challenge.

4.2. Acoustic impedance matching

Dynamic homogenization is used to design a one-dimensional PC which is impedance matched with aluminum at 300 kHz. To verify the calculations, five unit cells

of the composite sandwiched by two homogenous aluminum half-spaces are considered. Transfer matrix method is used to calculate the exact solution for the reflection coefficient. FE modeling and ultrasonic measurement are performed to find the reflection coefficient for verification.

4.2.1. Sample and test setup

The sample designed for this study is a one-dimensional composite made of periodic layers of steel and PMMA. The thickness of steel and PMMA layers are given by $t_{st} = 0.6\,mm$ and $t_{PMMA} = 0.2\,mm$, respectively. The longitudinal wave speed and density of steel, PMMA, and aluminum are given by $c_{st} = 5130\,m/s$, $\rho_{st} = 7820\ kg/m^3$, $c_{PMMA} = 2560\,m/s$, $\rho_{PMMA} = 1180\ kg/m^3$, $c_{Al} = 5100\,m/s$, and $\rho_{Al} = 2700\ kg/m^3$, respectively. Figure 4-1 shows the test fixture designed for this experiment together with the sample and the transducers. The fixture is designed to apply a precompression using a spring-nut system at the end of the fixture. Incident wave is sent through a piezoelectric transducer to the incident bar and is received by a similar transducer on the other end of the transmission bar. A piezoelectric sensor is attached to the surface of the incident aluminum bar in the middle to measure the incident and reflected waves.

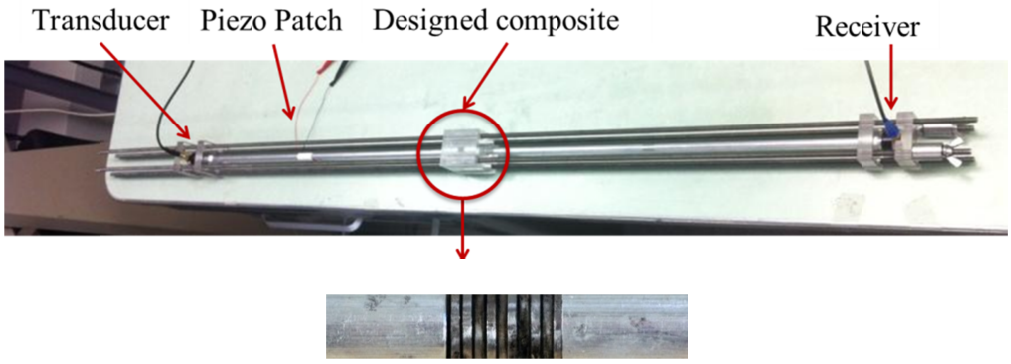

Figure 4-1: Test setup and the steel/PMMA sample sandwiched by two aluminum bars

4.2.2. Finite element simulation

Commercial FEM code, LS-DYNA, is used to perform three-dimensional finite element simulation of five unit cells of the steel/PMMA composite sandwiched by two aluminum bars. The geometry of the aluminum bars and the composite are same as described in the previous section. The boundary condition imposed on the left end of the incident bar is a prescribed displacement in the form of a wave packet with 10 sine waves at 300 kHz. The lateral sides and the right end of the transmission aluminum bar are traction free. The interfaces between each two adjacent layers are modeled as frictionless tied automatic contact interfaces. Linear elastic material model and standard 8-node solid brick elements are used. The mesh size is reduced until a mesh-independent solution is achieved. The time step is calculated by the smallest mesh size in the model to guarantee numerical stability.

4.2.3. Results

Figure 4-2 shows the theoretical band structure of the steel/PMMA composite. Figure 4-3 (a, b) show the effective compliance, effective density, and effective acoustic impedance of the composite over the first pass band. It can be seen that effective impedance of the composite is equal to impedance of aluminum ($Z_{Al} = 13.7$ MRayls) at 300 kHz. Due to the matched impedance of the composite and aluminum at 300 kHz, the reflection at their interface becomes zero.

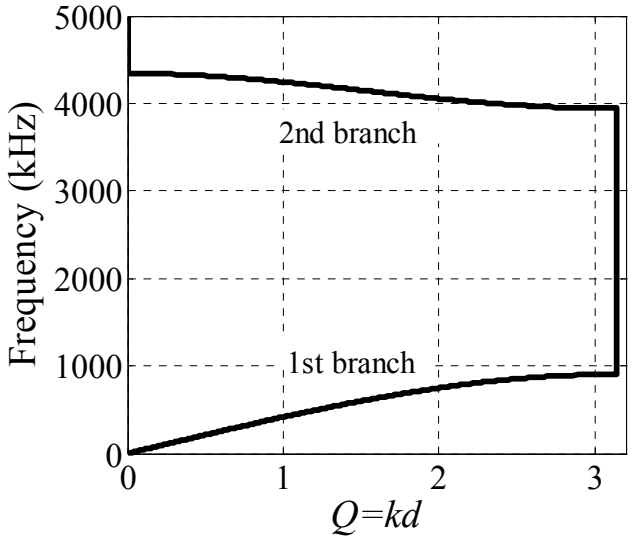

Figure 4-2: Theoretical band structure of the steel/PMMA sample

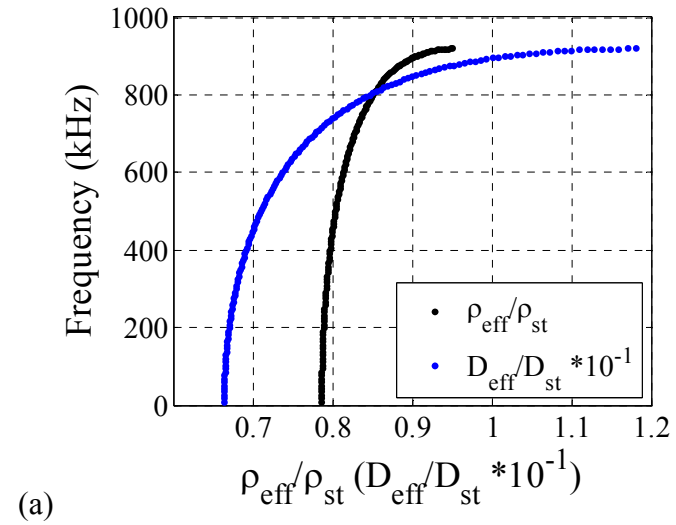

(a)

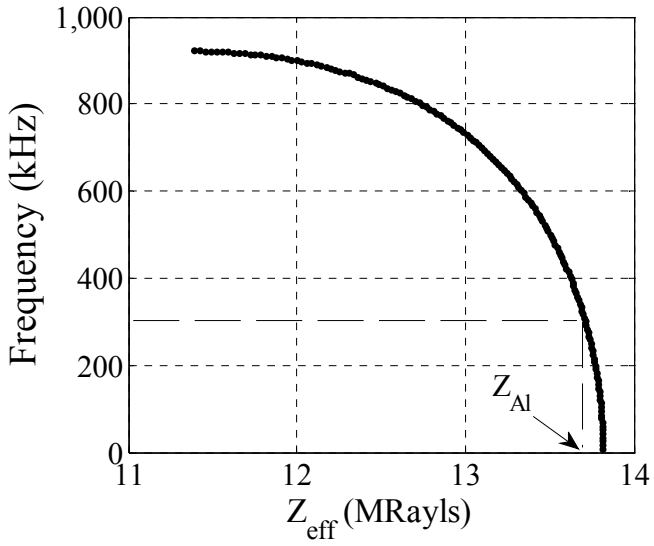

(b)

Figure 4-3: (a) Effective density and compliance and (b) effective acoustic impedance of the steel/PMMA sample over the first mode

Figure 4-4 shows the variation of the total energy in the aluminum bars at 300 kHz as a function of time obtained from the finite element simulation. The energy in the incident bar increases due to the work done by the external applied force at the left boundary, until it reaches a maximum value. The wave packet then travels inside the incident bar while its total energy remains constant. Then, it reaches the composite and

most of it gets transmitted to the transmission bar; while only 4.2% of its energy gets reflected. Although, transfer matrix calculation predicts zero reflection at 300 kHz, three-dimensional FE analysis gives slightly different results. This is mainly because the calculated effective impedance and reflection coefficient are based on one-dimensional assumption, while finite element analysis is a three-dimensional modeling of the system including the effect of dispersion.

Figure 4-5 shows the experimental reflection coefficient over 200-400 kHz which is compared to transfer matrix calculation. Although, the experimental reflection coefficient is small, the results are slightly different than the theoretical calculations. One of the main reasons for this difference is due to one-dimensional assumption in calculating the effective impedance and also the reflection coefficient through the transfer matrix method. Therefore, there are at least three possibilities for this difference (i) the sample is in cylindrical shape which results in dispersion, (ii) properties of the material constituents change with frequency, and (iii) the bonding at the interface of the layers and also at the interface of the piezoelectric sensor and the incident bar may not be perfect.

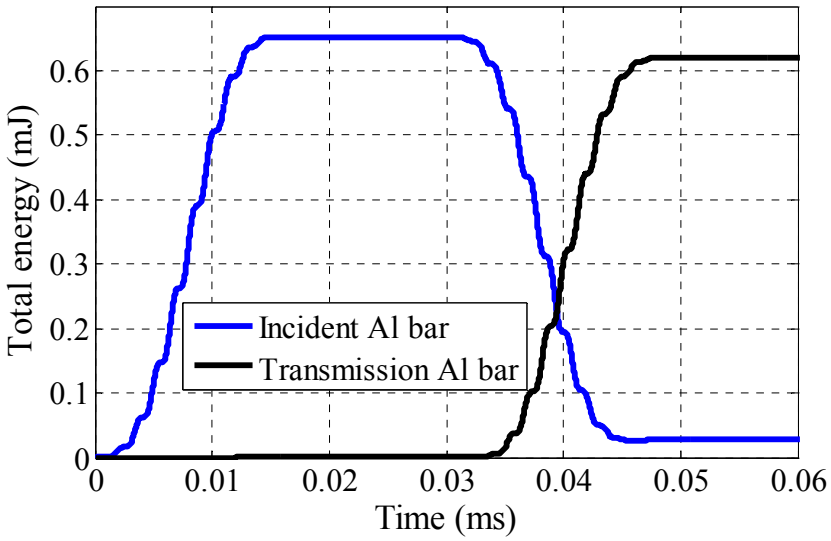

Figure 4-4: Total energy of the incident and transmission aluminum bars at 300 kHz calculated from finite element simulation

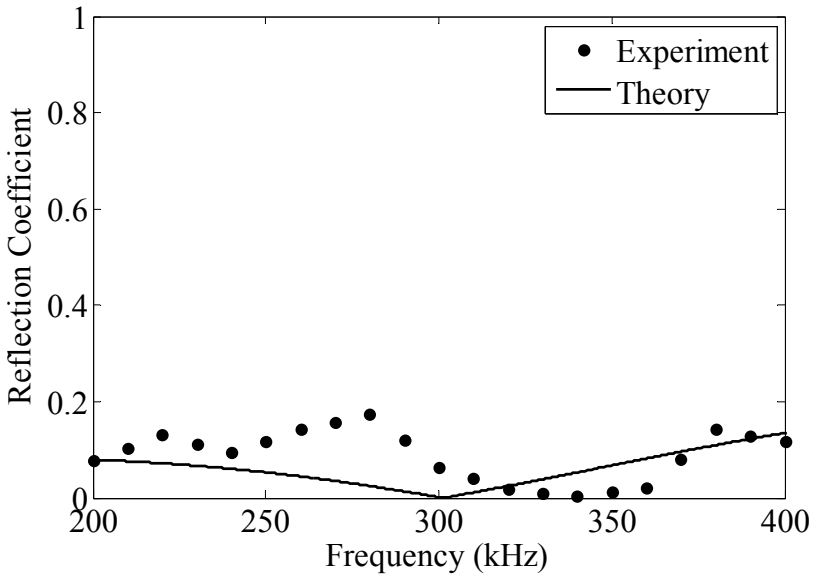

Figure 4-5: Comparison of reflection coefficient obtained from ultrasonic measurement and transfer matrix method for impedance matching verification

4.3. Metamaterial design for stress wave attenuation

A metamaterial is designed that attenuates stress waves effectively at low frequency range while it maintains high stiffness-to-density ratio. The essential idea is to design a one-dimensional metamaterial which has local resonance over its second mode, and also has a wide second band-gap. Dynamic homogenization is used to design a one-dimensional metamaterial and to calculate its effective elastodynamic properties. Transfer matrix method is used to calculate the attenuation coefficient of the composite. Samples are fabricated and their attenuation is measured experimentally and the data are compared with the theoretical results.

4.3.1. Sample geometry and composition

The sample designed for this study is a three-phase, one-dimensional composite which is made of periodic layers of carbon fiber reinforced polymer (CFRP), polyester foam, and steel. Figure 4-6 (a, b) show a schematic drawing and a photograph of one unit cell of the sample. The size of each layer is given by $t_1 = 7.0\,mm$, $t_2 = 3.2\,mm$, and $t_3 = 0.5\,mm$ for thickness of CFRP, foam, and steel, respectively. The through-thickness longitudinal wave speed and density of CFRP, polyester foam, and steel are given by $c_{CFRP} = 1980\,m/s$, $\rho_{CFRP} = 1530\ kg/m^3$, $c_{pf} = 230\,m/s$, $\rho_{pf} = 360\ kg/m^3$, $c_{st} = 5130\,m/s$, and $\rho_{st} = 7820\ kg/m^3$, respectively.

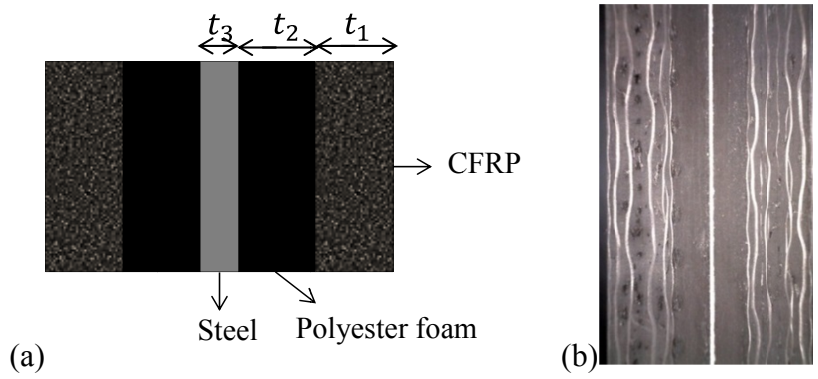

Figure 4-6: (a) Unit cell and (b) a photograph of the CFS metamaterial sample

4.3.2. Theoretical calculation

Figure 4-7 (a) shows the theoretical band structure for the CFRP/foam/steel (CFS) sample. In this figure the imaginary part of the normalized wave number represents the attenuation in the composite. It can be seen that the imaginary part of the wave number is small over 0 to 3.9 kHz; and therefore the wave propagates through the composite with small attenuation. However, from 3.9 to 20 kHz the imaginary part of the wave number is large and the wave attenuation in the composite is significant. Figure 4-7 (b, c) show the effective density and compliance of the composite over the first two pass bands. It can be seen that there is a discontinuity in the value of the effective density at 9.1 kHz which is due to presence of local resonance. This band structure is induced by the presence of the heavy central steel layer which is sandwiched between two soft foam layers and embedded in a CFRP matrix. With this microstructure it was possible to: (i) move the end of the first pass band to sonic frequency range, (ii) widen the second stop band, and (iii) create a local resonance over the second pass band.

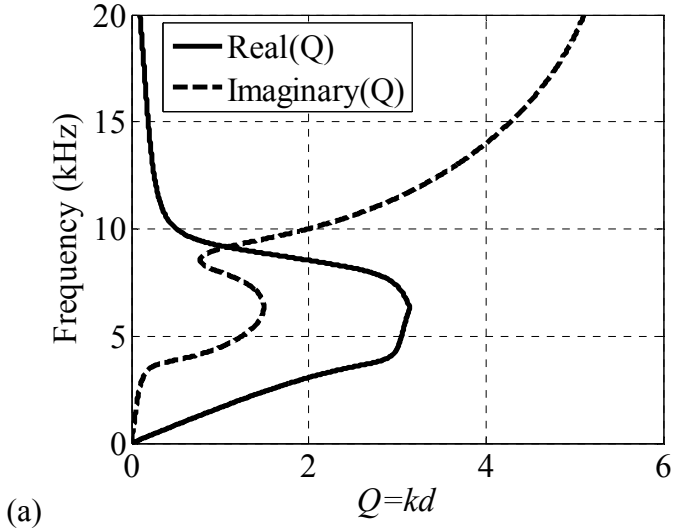

(a)

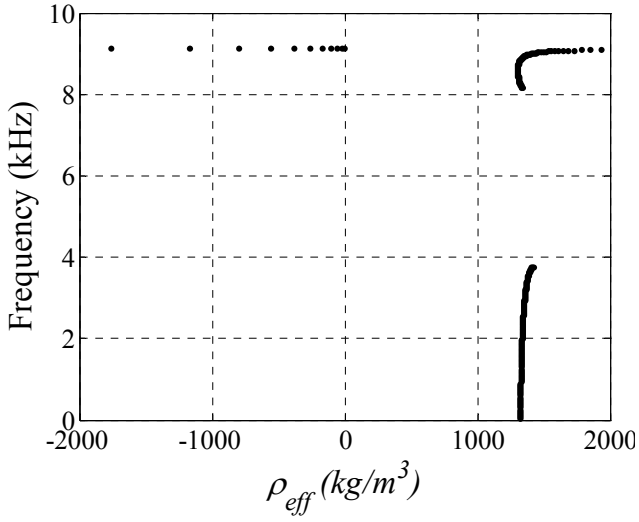

(b)

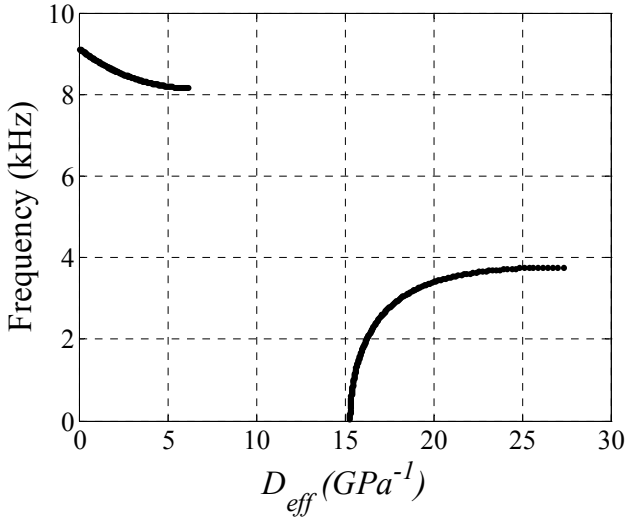

(c)

Figure 4-7: (a) Band structure, (b) effective density, and (c) effective compliance of the one-dimensional CFS metamaterial sample

4.3.3. Experimental results

Figure 4-8 shows the normalized transmission through 2 unit cells of the CFS sample. The experimental data are normalized with respect to transmitted amplitude in a transducer-to-transducer test. To show that the high attenuation coefficient in the sample is in fact due to the metamaterial response, the results for three different reference samples are also presented: (i) CF: the sample is made by removing the steel layer from the CFS sample, (ii) CS: the sample is made by removing the foam layers from the CFS sample, and (iii) C: the sample is made of CFRP with the same thickness as the CFS sample. It can be seen that the transmission through the CFS sample is significantly lower than C and CS samples over the entire frequency range. While up to 16 kHz the transmission in CFS and CF samples are close, above 16 kHz the transmission through CFS sample is significantly lower. Figure 4-9 shows the experimental attenuation per unit length in the CFS sample as a function of frequency. Theoretical attenuation is also shown in this figure for comparison. It is seen that the experimental results are in good agreement with the theoretical calculations. Also, it can be observed that above 4 kHz the attenuation per unit length is more than 500 dB/m and increases with increasing frequency. The difference between the theoretical and experimental data in Figure 4-9 stems mainly from the frequency dependence of the properties of the foam and the polymer components of the composite, and perhaps more significantly, from the sample geometry, i.e., the dispersion due to the cylindrical shape of the sample.

Figure 4-10 shows a dynamic Ashby chart, depicting attenuation coefficient vs. in-plane stiffness-to-density ratio, for various engineering materials, as well as that from the metamaterial design. Overall static in-plane stiffness-to-density ratio of the CFS

sample is calculated using the volume averages. In this figure it can be seen that polymers have high attenuation coefficient but small stiffness-to-density ratio, while metals have high stiffness-to-density ratio with small attenuation coefficient, whereas our metamaterial maintains both a large attenuation coefficient and also a large in-plane stiffness-to-density ratio. This kind of behavior cannot be achieved through any natural material at sonic frequency range which demonstrates the significance of the current metamaterial design.

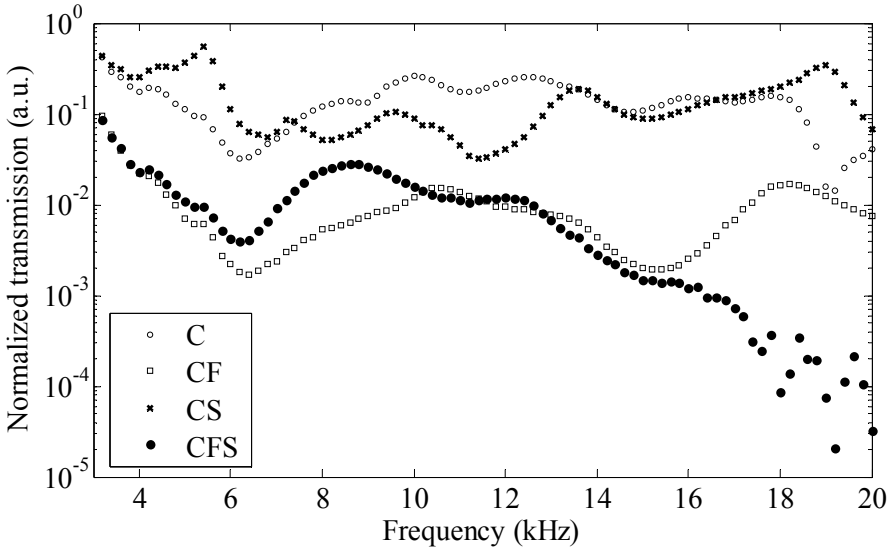

Figure 4-8: Normalized transmission through the metamaterials CFS sample as well as reference samples

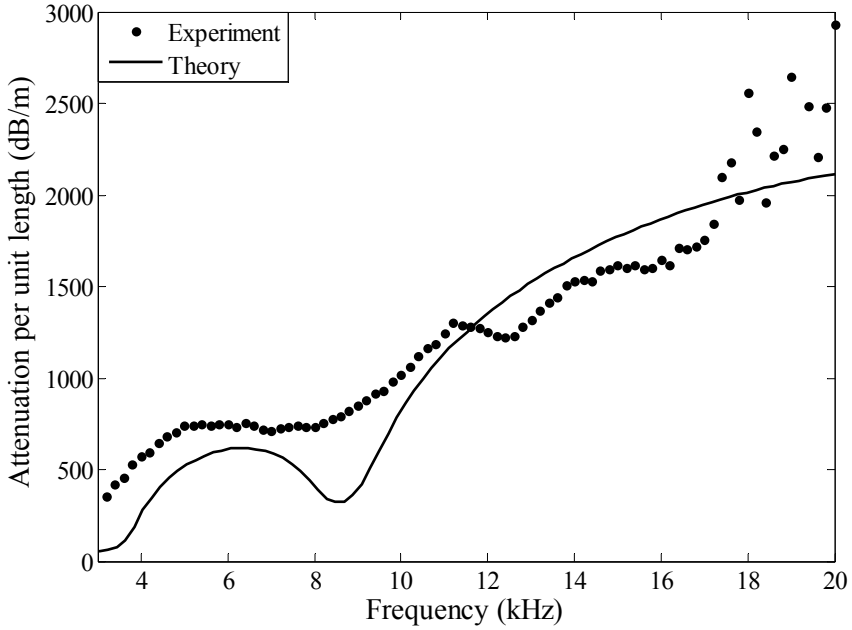

Figure 4-9: Theoretical vs. experimental attenuation in the metamaterial CFS sample

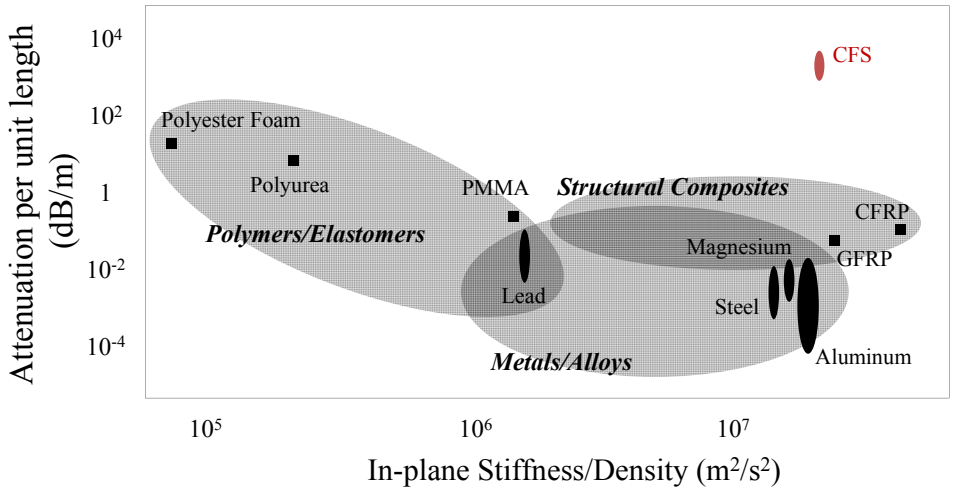

Figure 4-10: Dynamic Ashby chart for various engineering materials and comparison with optimally designed CFS (CFRP/foam/steel) sample (4-20kHz).

4.4. Summary

Dynamic homogenization is used to design a one-dimensional PC which is impedance matched with aluminum at 300 kHz. To verify the theoretical calculation, the reflection from five unit cells of the composite sandwiched by two homogenous aluminum half-spaces is studied. Transfer matrix method and finite element method are used to find the reflection coefficient theoretically. Samples are fabricated and ultrasonic tests are performed to measure the reflection coefficient experimentally. Experimental results are compared with theoretical calculations and reasonable agreement is observed. This approach can be used to design a layered composite with desired acoustic impedance serving as the matching layer in ultrasound transducers for efficient power transmission to test sample. In addition, a metamaterial is designed that attenuates stress waves effectively with a minimal thickness at low frequency range; while it maintains high stiffness-to-density ratio. Experimental measurements show that the attenuation per unit length in the metamaterial is in good agreement with theoretical calculations.

4.5. Acknowledgements

Chapter 4, in part, is reprint of the material as it appears in “Phononic layered composites for stress-wave attenuation”, Mechanics Research Communication, 2015, S. Nemat-Nasser, H. Sadeghi, A.V. Amirkhizi, and A. Srivastava, published by Elsevier. The dissertation author was the primary investigator of this paper.

Chapter 5

Experimental verification for design optimization of PCs

5.1. Introduction

When the microstructure of a periodic composite is known, its elastodynamic response can be directly calculated. However, finding the microstructure of a composite for a desired elastodynamic response is an inverse problem, which requires using optimization methods. In this chapter, optimization techniques are used together with mixed variational formulation and dynamic homogenization to make a computational platform for microstructural design of PCs. Constrained optimization problems are considered and a genetic algorithm is used to find the optimal design. Design optimization of one-, two-, and three-dimensional PCs with maximum band-gap bandwidth is first studied as an example. For evaluation of the computational platform, optimal design of PCs for shock wave mitigation is studied. The microstructure of a one-dimensional PC is designed which maximizes the band-gaps bandwidth in the frequency range of interest. To verify the theoretical calculation, a sample is fabricated and

Hopkinson bar experiments are performed. In addition, optimal design of one-dimensional PCs for minimum reflection and maximum attenuation is studied. Samples are fabricated and ultrasound measurements are performed for experimental verification.

In the recent years, there has been growing interest in using optimization techniques for microstructural design of PCs. Hussein et al. [58] used a genetic algorithm for design of one-dimensional PCs for an optimal frequency band structure. They illustrated examples which optimized the performance of layered PCs for acoustic filtering. Meng et al. [59] performed optimization to enhance the underwater sound absorption of an acoustic metamaterial slab. They illustrated the feasibility of combining several layers with different resonance frequencies to achieve a broadband underwater sound absorber. Wang et al. [60] studied the design of one-dimensional metamaterials to maximize the frequency range where a metamaterials exhibits negative effective elastodynamic properties. They used a genetic algorithm for optimization and illustrated that such an approach provides satisfactory results.

In the last few decades, there has been some interest to develop different techniques for sonar stealth; where an underwater object becomes invisible to sonar waves. The idea behind the passive sonar stealth is to cover the underwater object with a coating that absorbs most of incoming sonar waves. Therefore, the reflected waves off the surface of the object become small and it becomes difficult to detect the object. One of the most popular materials which has been used for this purpose is a synthetic rubber with specially designed micro voids. The issue with using this material is that the micro voids collapse in deep water due to high pressure. Here, designing a coating from PCs for sonar stealth of underwater objects is investigated. The idea is to design a PC which is

impedance matched with water to minimize the reflection at the interface of the surrounding water and the coating. The microstructure of the PC is then designed so that it has a high attenuation coefficient. Therefore most the waves transmitted to the PC coating are dissipated. Due to difficulties to perform underwater tests, aluminum is chosen here as the surrounding medium and experiments are performed to present as a proof of concept.

There have been several efforts to investigate the behavior of layered materials under shock loading. Zhuang et al. [61] investigated finite amplitude shock propagation in one-dimensional PCs experimentally. They observed that the shock speed in the composite is lower than the shock speed in its constituent materials. Chen and Chandra [62] considered the effect of heterogeneity in one-dimensional composites under impact loading. They studied the effect of impedance mismatch, thickness ratio, and interface density on the response of one-dimensional composites under impact loading. Luo et al. [63] studied stress wave propagation in two and three layer structures under an impulsive load. They showed that when an incident pulse passes through a one-dimensional structure, a reduced stress amplitude and elongated pulse duration can be obtained through the proper selection of materials and dimensions. Schimizze et al. [64] studied blast-induced shock wave mitigation in sandwich structures. They observed that the density and acoustic impedance mismatch are of primary importance in shock wave mitigation in sandwich structures.

5.2. Optimization

Consider an optimization problem of the form

$$\begin{aligned} &\text{Minimize } f(x) \\ &\text{Subject to } g_i(x) = 0 \quad (i = 1..m) \\ &\qquad\qquad h_j(x) > 0 \quad (j = 1..n) \end{aligned} \tag{5.1}$$

where $f(x)$ is the objective function, $g_i(x) = 0$ are equality constraints, and $h_j(x) > 0$ are inequality constraints. This constrained optimization problem can be reduced to the following unconstrained one using the quadratic penalty method and log barrier method [65]

$$\begin{aligned} &\text{Minimize } F_{\lambda_1,\lambda_1}(x) = f(x) + \lambda_1 \sum_{i=1}^{m} g_i(x)^2 - \lambda_2 \sum_{j=1}^{n} \log(h_j(x)) \\ &\qquad\qquad (i = 1..m, \quad j = 1..n) \end{aligned} \tag{5.2}$$

where $F_{\lambda_1,\lambda_2}$is the new objective function, and λ_1 and λ_2 are constant coefficient parameters. It can be shown that the global minimum of F_{λ_1,λ_1} is the solution of (5.1) as λ_1 goes to infinity and λ_2 goes to zero [65].

5.3. Genetic algorithm

Any global optimization method can be used to find the optimal solution of equation (5.2). Here genetic algorithm (GA) [66] is adopted which is a global optimization method and has been used successfully in several engineering problems. The GA begins by defining M arrays of N random variables within the design space. The value of objective function (cost) for each array is calculated and they are sorted from the lowest to highest cost. From the M designs, only the top M_{keep} are kept for mating and

the rest are discarded. Two designs (parent) out of the top M_{keep} designs are chosen based on a certain probability to mate, where the probability assigned to each design is inversely proportional to its cost (selection). Once the parents are chosen, their variables are swapped randomly to generate $M - M_{\text{keep}}$ new designs (crossover). Then, M_{mut} designs are chosen randomly and replaced with new random designs (mutation). The cost functions for the new designs are calculated and the process is repeated until convergence is achieved. Figure 5-1 shows a flow chart of the genetic algorithm used here. To increase the speed of calculations, computations are performed in parallel on different CPUs. GPUs are also used in matrix calculations when the dimensions of the matrices are large (typically above 2000x2000) to decrease the calculation time.

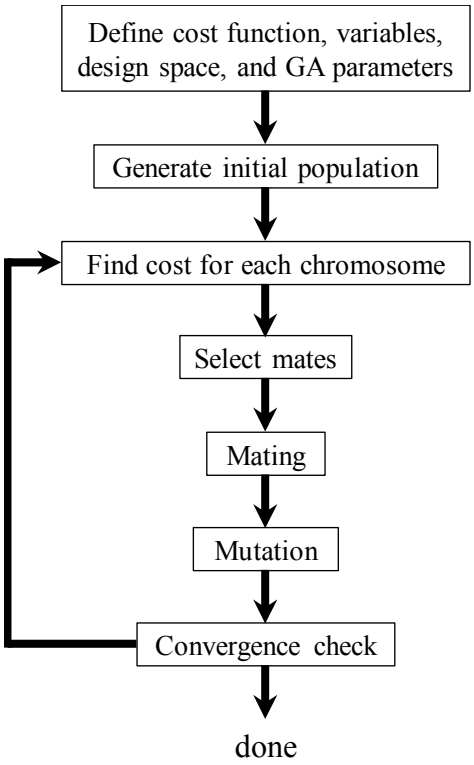

Figure 5-1: Flowchart of a genetic algorithm

5.4. Optimal design of elastic filters

As an example, GA is used to design the microstructure PCs with maximum band-gap bandwidth. One-, two-, and three-dimensional PCs with epoxy matrix and steel inclusions are considered. Figure 5-2 shows a unit cell of one-dimensional, two-dimensional, and three-dimensional PCs. For two- and three-dimensional PCs the inclusions are assumed to be in elliptical and ellipsoidal shapes, respectively. The Young modulus, Poisson ratio, and density of epoxy and steel are given by $E_{ep} = 5\ GPa, \nu_{\mathrm{ep}} = 0.35,\ \rho_{\mathrm{ep}} = 1200\ kg/m^3,\quad E_{st} = 200\ GPa,\quad \nu_{st} = 0.3,\quad$ and $\quad \rho_{st} = 8000\ kg/m^3$, respectively. The central frequency for the maximum band-gap is set to be 500 kHz which is applied as an equality constraint. The dimensions for the optimal one-dimensional design are given by $d_{\mathrm{ep}} = 1.26$ mm and $d_{\mathrm{st}} = 0.98$ mm for thickness of epoxy and steel, respectively. For the two-dimensional PCs, the dimensions of the optimal design are given by $a_1 = 2.21$ mm, $a_2 = 1.88$ mm, $b_1 = 1.83$ mm, and $b_2 = 1.51$ mm for the sides of epoxy and axes of steel inclusion, respectively. For three-dimensional case, the dimensions of the optimal design are given by $a_1 = 2.10$ mm, $a_2 = 2.02$ mm, $a_3 = 2.61$ mm, $b_1 = 1.82$ mm, $b_2 = 1.81$ mm, and $b_3 = 2.46$ mm for sides of epoxy and axes of steel inclusion, respectively. Figure 5-3 shows the optimal band structure for all three cases, where their corresponding normalized bandwidth, band-gap bandwidth over central frequency ratio, $\Delta f/f_0$, is 1.14, 0.62, and 0.43. It can be observed that by increasing the dimensions of the problem, from one- to three-dimensional, achieving higher bandwidth becomes more difficult due to the appearance of new modes at higher dimensions.

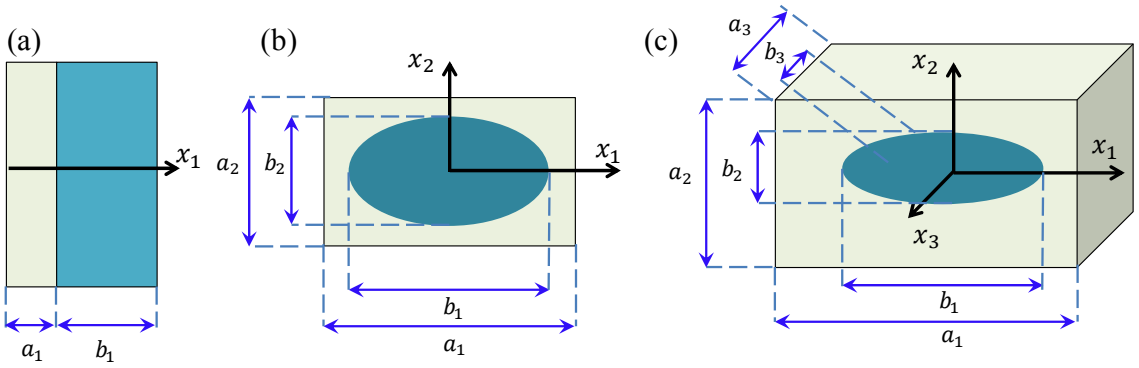

Figure 5-2: Unit cell of a (a) one-dimensional, (b) two-dimensional, and (c) three-dimensional PCs

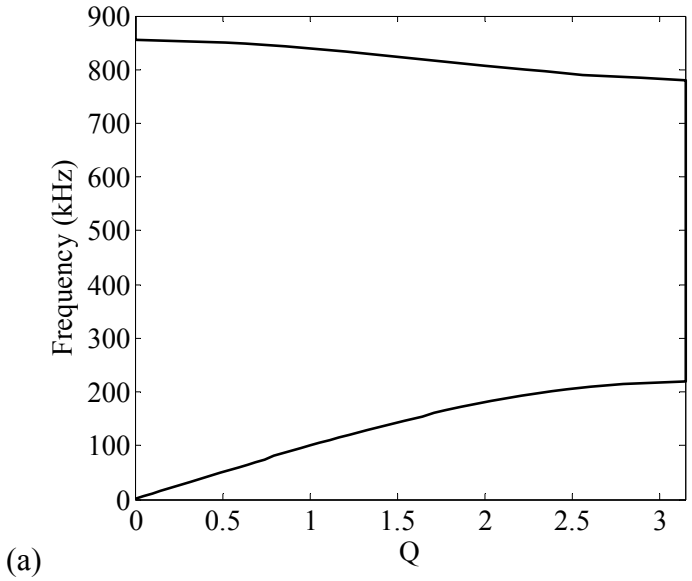

(a)

Figure 5-3: Band structure of (a) one-dimensional PC with maximum band-gap bandwidth (matrix: epoxy and inclusion: steel)

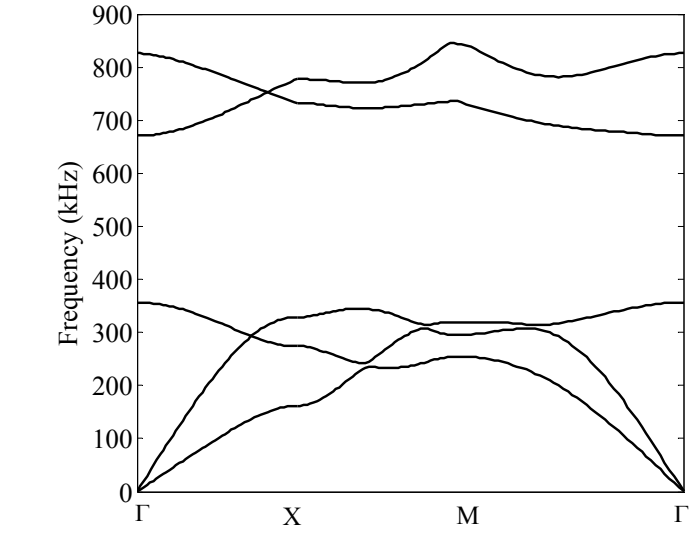

(b)

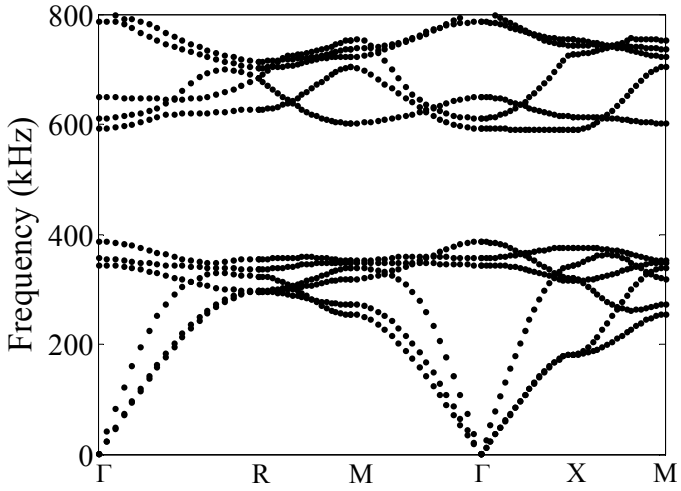

(c)

Figure 5-3: Band structure of (b) tow-dimensional and (c) three-dimensional PCs with maximum band-gap bandwidth (matrix: epoxy and inclusion: steel), continued

5.5. Optimal design of PCs for shock mitigation

Optimal design of PCs for shock wave mitigation is investigated experimentally. The frequency spectrum of a shock with a sharp rise-time is calculated, and the frequency range that carries the majority of the shock energy is identified as the target frequency

range. A genetic algorithm is used to design the microstructure of a one-dimensional PC for maximum band-gap bandwidth. A constraint is introduced into the optimization problem to limit the total thickness of the composite. To verify the theoretical calculation, samples are fabricated and Hopkinson bar experiments are performed.

5.5.1. Design optimization

The objective is to determine the microstructure of a one-dimensional PC which maximizes the band-gaps over a target frequency range, f_1' to f_2'. The band-gap ratio (BR) is defined as the ratio of sum of the band-gaps frequency ranges divided by the total frequency range

$$BR = \frac{\sum(f_2^{(i)} - f_1^{(i)})}{f_2' - f_1'} \tag{5.3}$$

where $f_1^{(i)}$ and $f_2^{(i)}$ are the frequencies where the i-th band-gap begins and ends, respectively. A constraint is introduced to limit the total unit cell size of the composite to be equal to a prescribed value, D. The objective function is defined as inverse of the band-gap ratio and the optimization problem is expressed as

$$\begin{gathered} \text{Minimize } \frac{f_2' - f_1'}{\sum(f_2^{(i)} - f_1^{(i)})} \\ \text{Subject to } \sum_{j=1}^{N} d^{(j)} = D \end{gathered} \tag{5.4}$$

In order to find the solution of (5.4) we define

$$F_\lambda(\boldsymbol{d}) = \frac{f_2' - f_1'}{\sum(f_2^{(i)} - f_1^{(i)})} + \lambda\left(\sum_{j=1}^{N} d^{(j)} - D\right)^2 \tag{5.5}$$

where F_λ is the new objective function and λ is a positive coefficient.

5.5.2. Hopkinson bar setup

Figure 5-4 and Figure 5-5 show a schematic representation and a photograph of the Hopkinson bar setup used in this study, respectively. A mini gas chamber is designed and fabricated for this experiment to better control the speed of the projectile in order to keep the stresses in the sample within elastic limit. The striker bar hits end A of the incident bar at a given velocity which produces a compressive pulse traveling along the incident bar. The sample is sandwiched between end B of the incident bar and end C of the transmission bar. When the pulse reaches the sample, a portion of the pulse is transmitted to the transmission bar, and a portion of it is reflected back into the incident bar. Strain gauges, S1 and S2, measure the strain, $\varepsilon(t)$, in the middle of the incident and transmission bars as a function of time. The incident, transmission, and striker bars are all made of steel with common diameter of 1.27 cm. The length of both the incident and transmission bars are 1.22 m, and the length of the striker bar is 10.16 cm. The particle velocity, $V(t)$, and axial stress, $\sigma(t)$, in the bars can be calculated as [67]

$$\begin{aligned} V(t) &= c_0 \varepsilon(t) \\ \sigma(t) &= \rho c_0 V(t) \end{aligned} \tag{5.6}$$

where c_0 and ρ are the wave speed and the density of the bars, respectively. The total energy carried by a pulse can be calculated as

$$E = e_0 \int_0^t V(\tau)^2 d\tau \tag{5.7}$$

where e_0 is a constant coefficient.

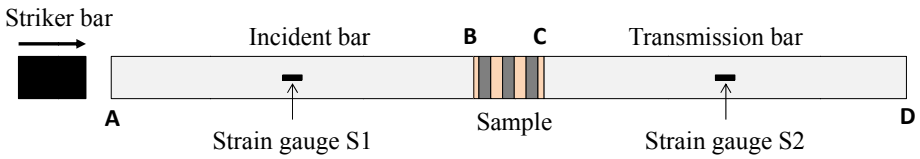

Figure 5-4: Schematic of the Hopkinson bar setup

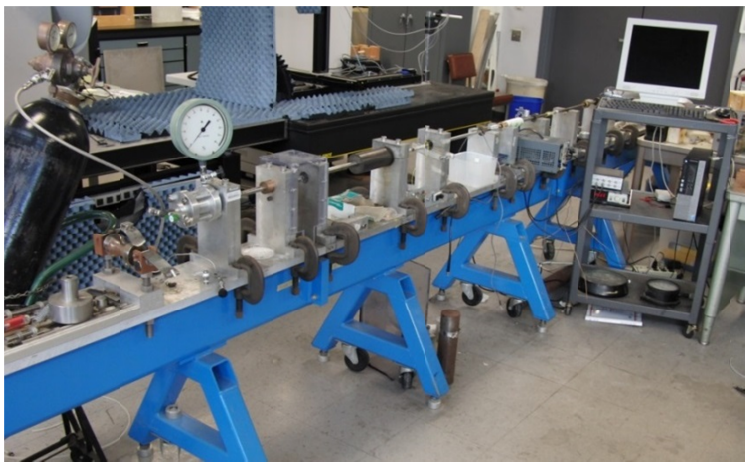

Figure 5-5: A photograph of the Hopkinson bar setup

5.5.3. Results

The incident bar is hit by the striker bar and the incident pulse is measured by strain gauge S1. Fast Fourier transform (FFT) of the incident pulse is calculated and it is observed that the majority of the pulse energy is carried by the pulse components with frequencies within 0 to 100 kHz; which is chosen as the target frequency range. The design space is chosen to be $0.1\ cm < d^{(j)} < 1\ cm$ for the thickness of each layer. The total unit cell size, D, is chosen to be $2\ cm$. Here two-phase PCs with periodic layers of polycarbonate and steel are considered and the number of layers in the unit cell, N, can vary (see Figure 5-6). Without loss of generality, it is assumed that the first layer in the unit cell is made of polycarbonate. The material properties of each phase are given by

$c_{st} = 5064\,m/s$, $\rho_{st} = 7810\ kg/m^3$, $c_{pc} = 2236\,m/s$, and $\rho_{pc} = 1193\ kg/m^3$ for the wave speed and density of steel and polycarbonate, respectively.

Table 5-1 shows the optimal design and band-gap ratio for different values of N. It can be seen that $N = 3$ yields the largest band-gap ratio and therefore is chosen as the optimal design. It is understood that in this problem increasing the number of layers does not necessarily produce wider band-gaps. Figure 5-7 (a) shows the corresponding band structure for the optimal design. It can be seen that there is a wide band-gap from 28 to 104 kHz. Figure 5-7(b) shows the transmission and reflection spectra of five unit cells of the composite sandwiched by two half-space steel bars. It can be seen that components of the pulse with frequency content over the band-gaps are completely reflected. Also, a significant portion of the wave energy with frequencies over the pass bands is reflected. It should be noted that part of the reflection is due to the impedance mismatch between the incident bar and the sample.

Table 5-1: Optimal design for shock wave mitigation (polycarbonate/steel)

N	$d^{(j)}$ $(j = 1..N)$ (mm)	$BR\%$
2	14.6, 5.4	59.5
3	4.0, 9.6, 6.4	73.2
4	1.1, 3.9, 8.7, 6.3	61.5
5	2.2, 7.3, 4.2, 1.1, 5.2	62.1

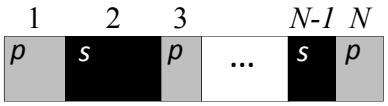

Figure 5-6: Unit cell of a two-phase, one-dimensional polycarbonate/steel PC

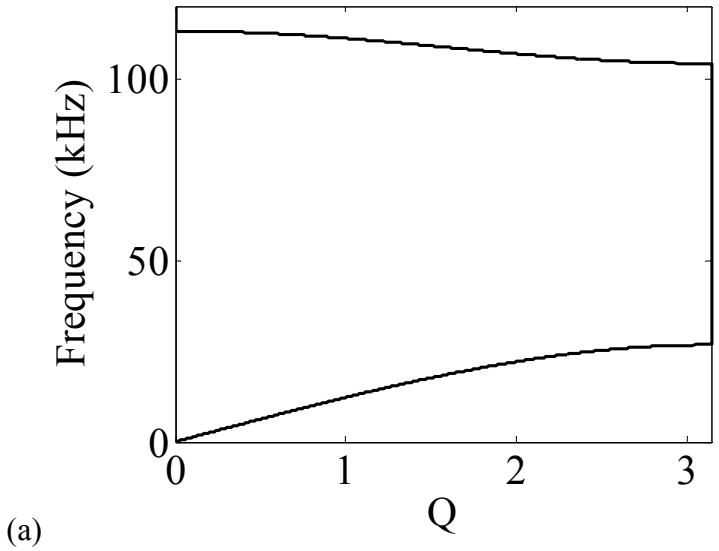

(a)

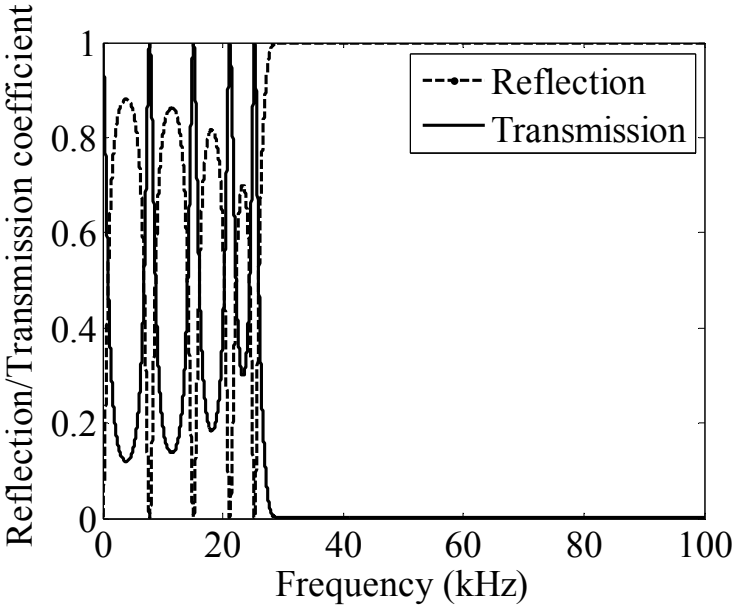

(b)

Figure 5-7: (a) Band structure of the polycarbonate/steel sample and (b) reflection and transmission spectra of the sample sandwiched by two steel half-spaces

Figure 5-8 (a) shows the experimentally measured transmitted and incident pulses (pulses are shifted in time for comparison purposes). It can be seen that the rise time of transmitted pulse is $\tau_{tr}^{*} = 62.5\ \mu s$, which is 4.3 times larger than the incident pulse rise time. Also, the maximum stress of the transmitted pulse is $\sigma_{tr}^{*} = 37.1\ MPa$, which is 3.4 times less than that of the incident pulse. Figure 5-8 (b) shows the FFT of the incident and transmitted pulses. It can be seen that the components of the incident pulse with frequencies above 28 kHz, which are within the band-gaps of the composite, are not transmitted. Furthermore, using the arrival time of the transmitted pule, the wave speed in the sample is measured to be $1538\ m/s$ which is 45.4% less than the wave speed in polycarbonate. The energy of the incident and transmitted pulses is calculated and it is observed that only 9.7% of the incident pulse energy gets transmitted. The increase in the rise time and the decrease in the maximum stress of the transmitted pulse compared to those of the incident pulse are mainly due to: (i) a significant portion of the incident pulse getting reflected over the stopbands, (ii) components of the pulse within the pass bands being dispersed due to multiple reflections occurring within the composite, (iii) viscous dissipation in polycarbonate, and (iv) reflections at the interface of the steel bars and the composite due to impedance mismatch. It is important to note that the first two attenuation mechanisms are absent in homogenous materials, which leads to higher attenuation in the sample. The in-plane quasi-static stiffness of the composite is calculated to be 99.1 GPa. This shows the significance of this design leading to both high in-plane stiffness and high attenuation simultaneously; which are essential for shock wave mitigation.

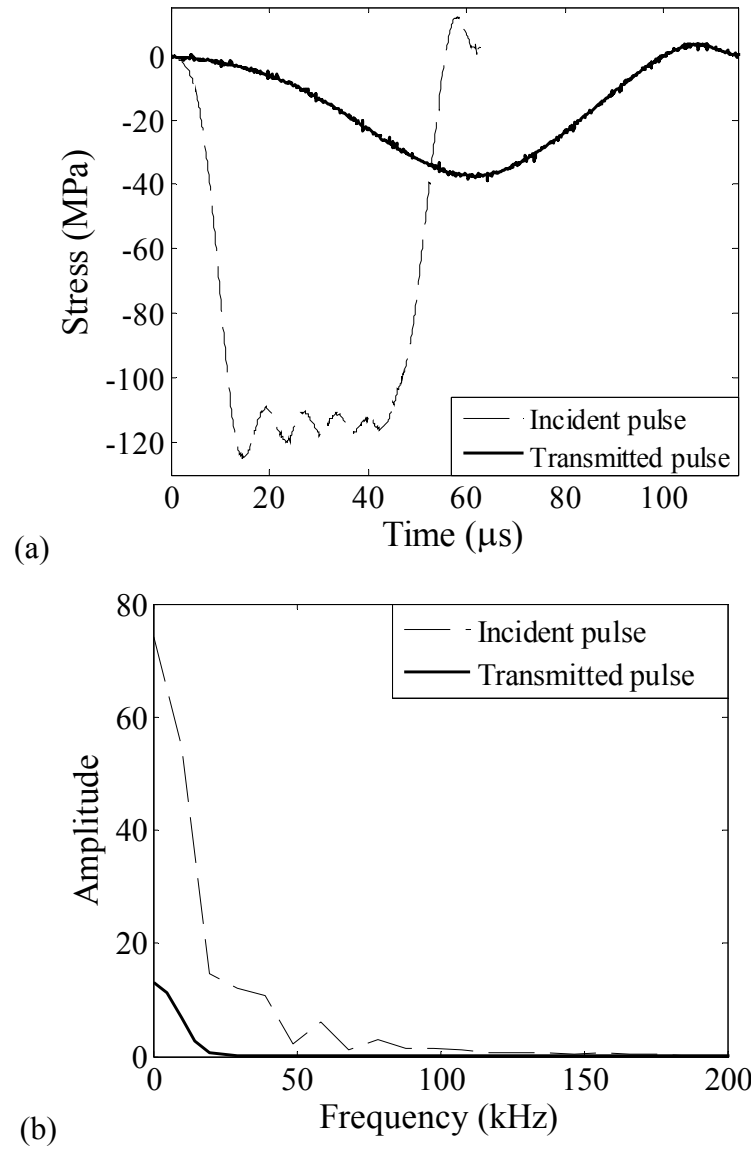

Figure 5-8: (a) Experimentally measured incident and transmitted pulses of the steel/polycarboate sample in Hopkinson bar test and (b) FFT of the incident and transmitted pulses

5.6. Microstructural design for minimum reflection and maximum attenuation

Consider a finite slab of a one-dimensional PC, sandwiched by two homogenous half-spaces as shown in Figure 5-9. The objective is to design the microstructure of the PC to minimize the reflected waves energy and maximize the attenuation in the

composite. The target frequency range is chosen to be from 0 to f_0. The objective function is defined as the inverse of the attenuation in the composite. In order to minimize the reflection over the target frequency range, the composite is impedance matched with the half-spaces over its first mode. To achieve this (i) the end of target frequency, f_0, should be within the first pass band and (ii) the effective impedance of composite, Z_{eff}, should not deviate from the impedance of the half-spaces, Z_0, within a certain acceptable percentage, p. These two conditions are formulated as inequality constraints: (i) $h_1(x) = f_1 - f_0 > 0$ and (ii) $h_2(\boldsymbol{x}) = pZ_0 - |Z_{eff} - Z_0| > 0$, respectively. See Figure 5-10(a, b) for graphical description of these constrains. The optimization problem can therefore be expressed as

$$\begin{aligned} &\text{Minimize } f(x) = 1/D \\ &\text{Subject to } h_1(x) = f_1 - f_0 > 0 \\ &h_2(x) = pZ_0 - |Z_{eff} - Z_0| > 0 \end{aligned} \tag{5.8}$$

where D is dissipation in the composite at f_0. This constrained optimization problem can be reduced to the following unconstrained one

$$\text{Minimize } F(\boldsymbol{x}) = 1/D - \lambda\big(\log(f_1 - f_0) + \log(pZ_0 - |Z_{eff} - Z_0|)\big) \tag{5.9}$$

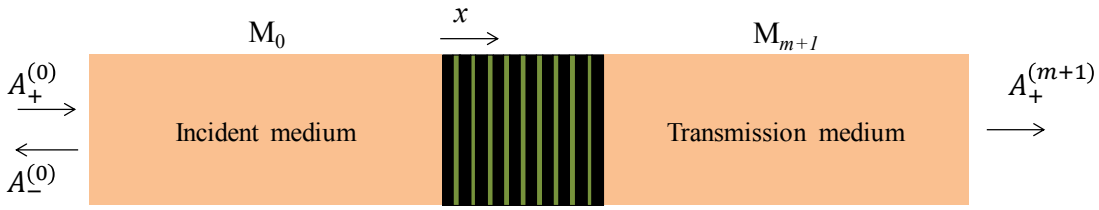

Figure 5-9: A one-dimensional PC sandwiched by two homogenous half-spaces

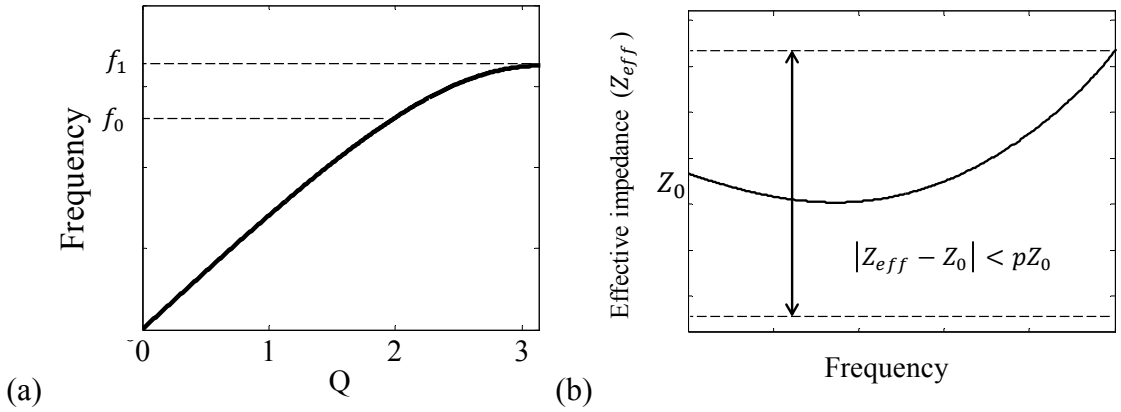

Figure 5-10: Graphical description of the constraints for impedance matching (a) band structure and (b) effective impedance over the first pass band

5.6.1. Sample

Here, three-phase, one-dimensional PCs are considered and the thicknesses of each phase are the design parameters. The target frequency is chosen to be f_0 =50 kHz, constant coefficient p to be %5, and the half-spaces are made of aluminum. The constituent materials of the three-phase composite are chosen to be brass, polycarbonate, and steel for the first, second, and third phases, respectively. Figure 5-11 shows a schematic photograph of the unit cell where t_1, t_2, and t_3 are the thicknesses of brass, polycarbonate, and steel, respectively. The design space is chosen to be $0.1\,mm < t_i < 5\,mm$ for thickness of each phase. The material properties for each phase are given by $c_1 = 4021\ m/s$, $\rho_1 = 8476\,kg/m^3$, $c_2 = 2224\,m/s$, $\rho_2 = 1193\,kg/m^3$, $c_3 = 5173\ m/s$, and $\rho_3 = 7830\,kg/m^3$ for the wave velocity and density of brass, polycarbonate, and steel, respectively. The loss tangent for polycarbonate is measured to be $\tan(\delta_2) = 3.3\%$, while the loss in the other two constituent materials is negligible. The effect of the constant coefficient λ_2 is studied and it is observed that as λ_2 increases,

the constraints are imposed more strictly, which results in less reflected energy. This comes at the expense of lowering the dissipation. It is observed that $\lambda = 0.1/\log(f_0)$ yields reasonable results in terms of both maximizing the attenuation and minimizing the reflection, and therefore is selected as the optimal parameter. In order to evaluate the performance of the optimal design, two reference samples with the same unit cell size and the same constituent materials but different microstructures are fabricated. Table 5-2 shows the microstructure of the optimal design (design 1) together with the two reference samples (design 2 and 3).

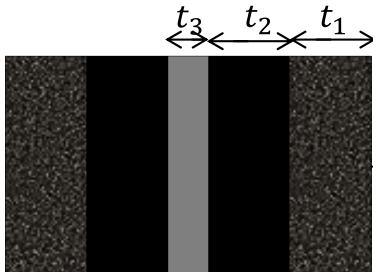

Figure 5-11: Unit cell of a three-phase, one-dimensional PC

Table 5-2: Optimal design (design 1) and two reference designs with the same unit cell size for mininum reflection and maximum attenuation

	Design 1	Design 2	Design 3
(t_1, t_2, t_3)	(1.22, 0.74, 4.05)	(0.50, 1.46, 4.05)	(1.72, 1.24, 2.05)

5.6.2. Test procedure and results

Figure 5-12 shows the experimental setup designed for this experiment. The sample is sandwiched by two 4 ft long aluminum bars. Stress waves are sent from the left end of the incident bar using a piezoelectric transducer. The waves travel through the incident bar and reach the sample; where parts of them get transmitted to the transmission

bar. The transmitted wave is received by another transducer at the right end of the transmission bar. The receiving transducer is connected to a spring-nut system to apply a precompression, required for good transmission of the stress waves through the interfaces. A semiconductor strain gauge is attached to the surface of the incident bar to measure the incident and reflected waves. The setup is calibrated performing a test with no sample in between the incident and transmission aluminum bars.

Figure 5-13 shows the reflection and transmission coefficients of the samples. It can be observed that the dissipation in the optimal design is higher than the other two samples over the entire frequency range. Also, it can be seen that the reflection coefficient of the optimal design is significantly lower than that of sample 3. Although, the reflection of the optimal design is slightly more than the reflection coefficient of sample 2 in some frequencies, the difference between their values is negligible. This shows that the optimal design has superior response over the two reference samples both in terms of minimizing the reflection and maximizing the dissipation.

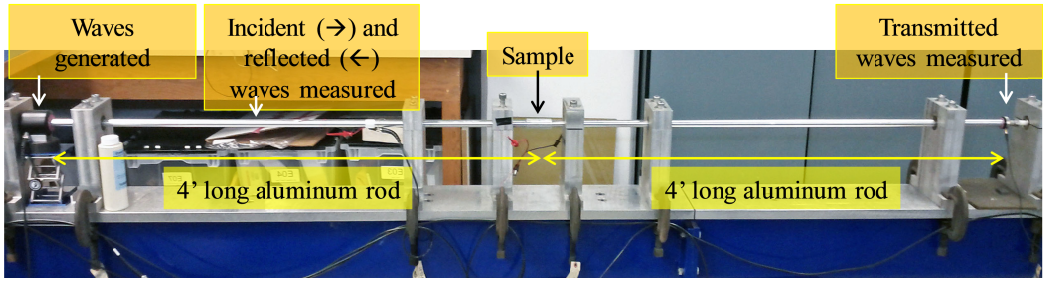

Figure 5-12: Experimental setup used for measurement of reflection and transmission

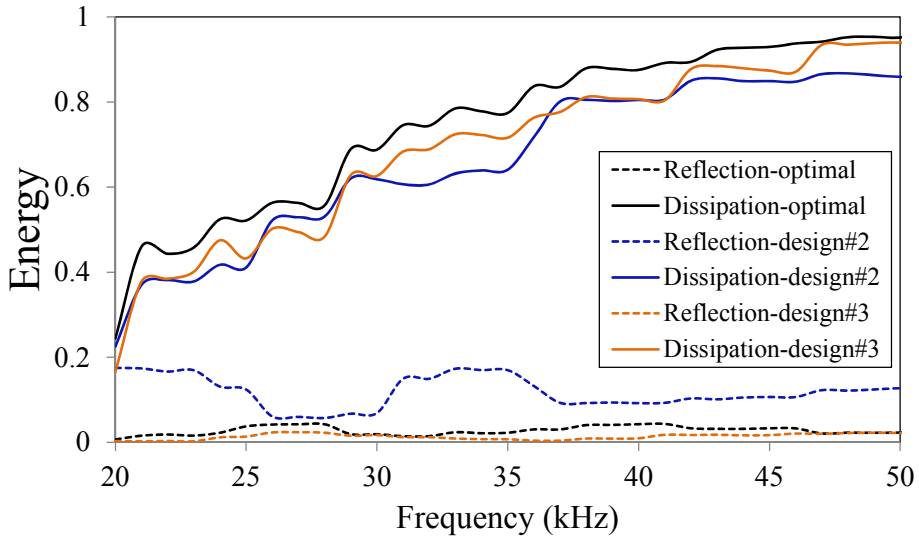

Figure 5-13: Experimental reflection and attenuation spectra of the samples for minimal refelction and maximum dissipation

5.7. Summary

Design optimization of PCs for a desired elastodynamic response is studied. Optimal design of one-, two-, and three-dimensional PCs with maximum band-gap bandwidth is first studied as an example. It is observed that by increasing the dimension of the problem, i.e. from one- to three-dimensional, achieving high bandwidth becomes more difficult. In addition, optimal design of one-dimensional PCs for shock wave mitigation is studied. A genetic algorithm is used to design the microstructure of a one-dimensional PC for maximum band-gap bandwidth. To verify the theoretical calculations, samples are fabricated and Hopkinson bar experiments are performed. It is observed that only a small portion of energy of the incident pulse gets transmitted and the maximum stress of the transmitted pulse drops significantly. In addition, optimal design of one-dimensional PCs for minimum reflection and maximum attenuation of stress waves is investigated. Two reference samples with the same unit cell size and same constituent

materials but different microstructures are fabricated for comparison. It is observed that the optimal design exhibits superior performance over the two reference samples, both in terms of minimizing the reflection and maximizing the attenuation.

Chapter 6

Energy refraction in two-dimensional periodic composites

6.1. Introduction

Microstructure of a PC can be designed to achieve negative energy refraction at the interface of the PC and a homogenous medium at certain frequency ranges. This feature can be used to focus stress waves in a focal point in order to make flat acoustic lens for applications like ultrasound imaging. Furthermore, due to recent advances in transformational acoustics, which makes acoustic cloaking achievable [43], dynamic homogenization has become a powerful tool for microstructural design of the cloak [44]. This demands further understanding of dynamic homogenization techniques and their limitations. In this chapter, mixed variational formulation is used together with dynamic homogenization to study energy refraction in two-dimensional PCs. Equifrequency surfaces (EFS) of a two-dimensional PC made of epoxy matrix with steel inclusions are calculated. Frequency-dependent overall elastodynamic properties of the PC are obtained

through dynamic homogenization. Vectors of group velocity are studied and energy refraction at the interface of a homogenous half-space and the PC is investigated.

In the recent years, there have been many efforts to study negative energy refraction behavior in PCs. Yang et al. [68] presented a combined experimental and theoretical study of negative refraction in three-dimensional PCs. They showed that three-dimensional PCs can be used to focus a diverging ultrasound beam into a narrow focal spot. Li et al. [23] used the multiple scattering technique and studied the negative energy refraction of acoustic waves in two-dimensional phononic crystals. They showed that local resonance mechanism brings on a group of flat bands in low frequency region which provides two EFS's close to circular leading to negative refraction. Croenne et al. [24] presented experimental evidence of negative refraction of longitudinal waves in two-dimensional PCs with a solid matrix. They fabricated a PC made of triangular arrangements of steel rods embedded in epoxy and carried out an experiment on a prism-shaped PC inside an epoxy block and observed negative refraction experimentally. Nemat-Nasser [25, 26] studied anti-plane shear wave propagation in one- and two-dimensional PCs using a mixed variational formulation. He showed that negative energy refraction can be accompanied by positive phase-velocity refraction, and positive energy refraction can be accompanied by negative phase-velocity refraction.

6.2. Unit cell properties

Consider a two-dimensional PC with square unit cell and dimensions given by $a_1 = a_2 = 3\ cm$, and square inclusions with dimensions $b_1 = b_2 = 1\ cm$, as shown in Figure 6-1. The matrix is made of epoxy and the inclusions are made of steel with

material properties given by $E_m = 3\,GPa$, $\nu_m = 0.35$, $\rho_m = 1100\ kg/m^3$, $E_i = 200\,GPa$, $\nu_i = 0.3$, and $\rho_i = 8000\ kg/m^3$ for the Young's modulus, Poisson ratio, and density of epoxy and steel, respectively.

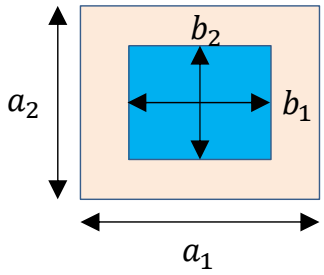

Figure 6-1: Unit cell of the epoxy/steel two-dimensional PC

6.3. Frequency band structure

Mixed variational method, described in chapter 2, is used to calculate the frequency band structure of the two-dimensional epoxy/steel PC for plane stress condition. Figure 6-2 (a, b) show the band structure of the epoxy/steel PC and a three-dimensional plot of the first three eigenmodes, respectively. In this figure, the lower two modes are acoustic shear vertical mode (SV-mode) and acoustic longitudinal mode (L-mode), respectively. It can be seen that the first three modes of the PC have no intersection which makes it possible to study each mode separately.

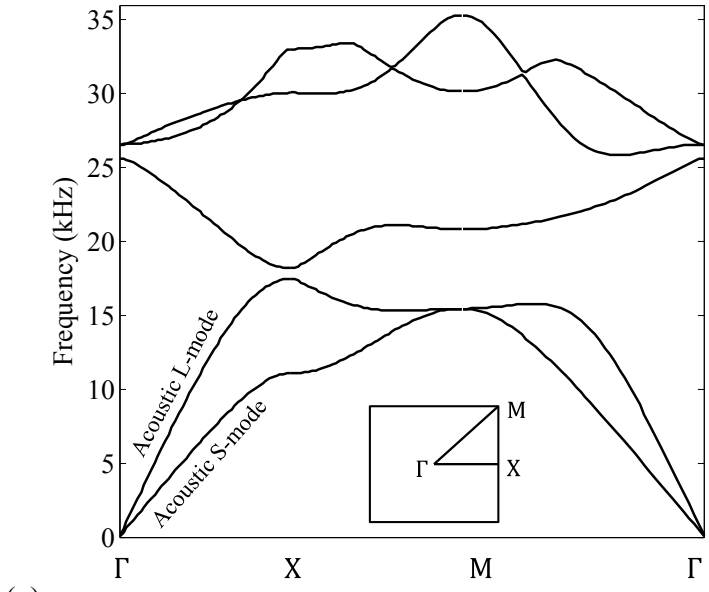

(a)

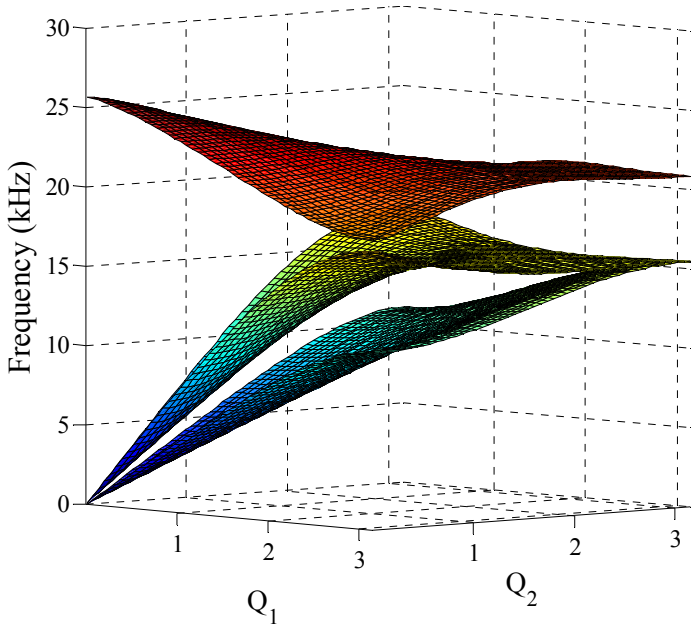

(b)

Figure 6-2: (a) Frequency band structure and (c) three-dimensional eigenmodes of the two-dimensional epoxy/steel PC

6.4. Dynamic homogenization

The micromechanical method, described in chapter 2, is used to calculate the effective elastodynamic properties of the two-dimensional epoxy/steel PC. Figure 6-3 shows the comparison between the band structures calculated from the mixed variational formulation as well as from the micromechanical method as a function of Q_1 for a fixed value of $Q_2 = 2$. In this figure, $10^2 - 1$ Fourier expansion terms and 10^2 subdomains are used in micromechanical calculations. Also, 9^2 Fourier expansion terms are used for calculating the band structure using mixed variational method. It can be seen that the band structures obtained from these two methods are in good agreement. Also, it is observed that as the frequency increases, the difference between the results obtained from these two methods increases. For example, while the first two modes are in very close agreement, the third and fourth modes obtained from micromechanical method are slightly different than the results obtained from variational method.

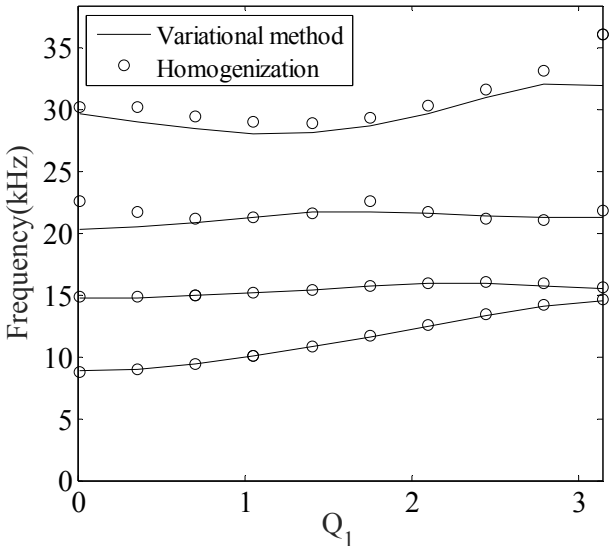

Figure 6-3: Comparison between the band structure calculated from mixed variational formulation as well as from the micromechanical method for the epoxy/steel PC

6.4.1. Acoustic shear mode

Figure 6-4 (a) shows the equifrequency surfaces (EFS) of the epoxy/steel PC in kHz for the acoustic SV-mode together with vectors of group velocity in the (Q_1, Q_2)-space. It can be seen that the components of group velocity vectors along the x_1- and x_2-axes are in the same direction as those of the phase velocity's. Figure 6-4 (b-h) show the non-zero effective properties of the PC in the (Q_1, Q_2)-space. The values of effective density, effective compliance, and coupling terms are given in terms of kg/m^3, $(Pa^{-1}) \times 10^{-11}$, and $(s/m) \times 10^{-5}$, respectively. The values of $\bar{\rho}_{22}$, $\bar{D}_{22}$, $\bar{D}_{21}$, $\bar{S}^1_{22}$, $\bar{S}^1_{21}$, and $\bar{S}^1_{32}$ are transpose of $\bar{\rho}_{11}$, $\bar{D}_{11}$, $\bar{D}_{12}$, $\bar{S}^1_{11}$, $\bar{S}^1_{12}$, and $\bar{S}^1_{31}$ in the (Q_1, Q_2)-space, respectively, and are not shown here for the sake of brevity. It can be seen that all the effective properties are continuous over the first BZ for the acoustic S-mode.

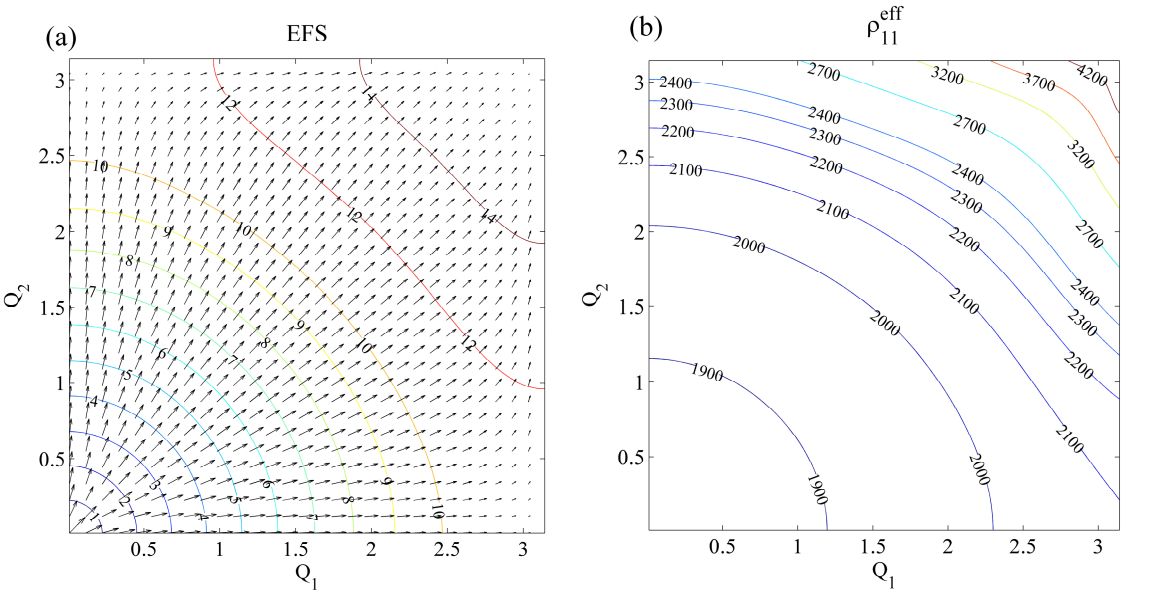

Figure 6-4: Contours of (a) EFS and (b) $\bar{\rho}_{11}$ over the acoustic SV-mode for the two-dimensional epoxy/steel PC

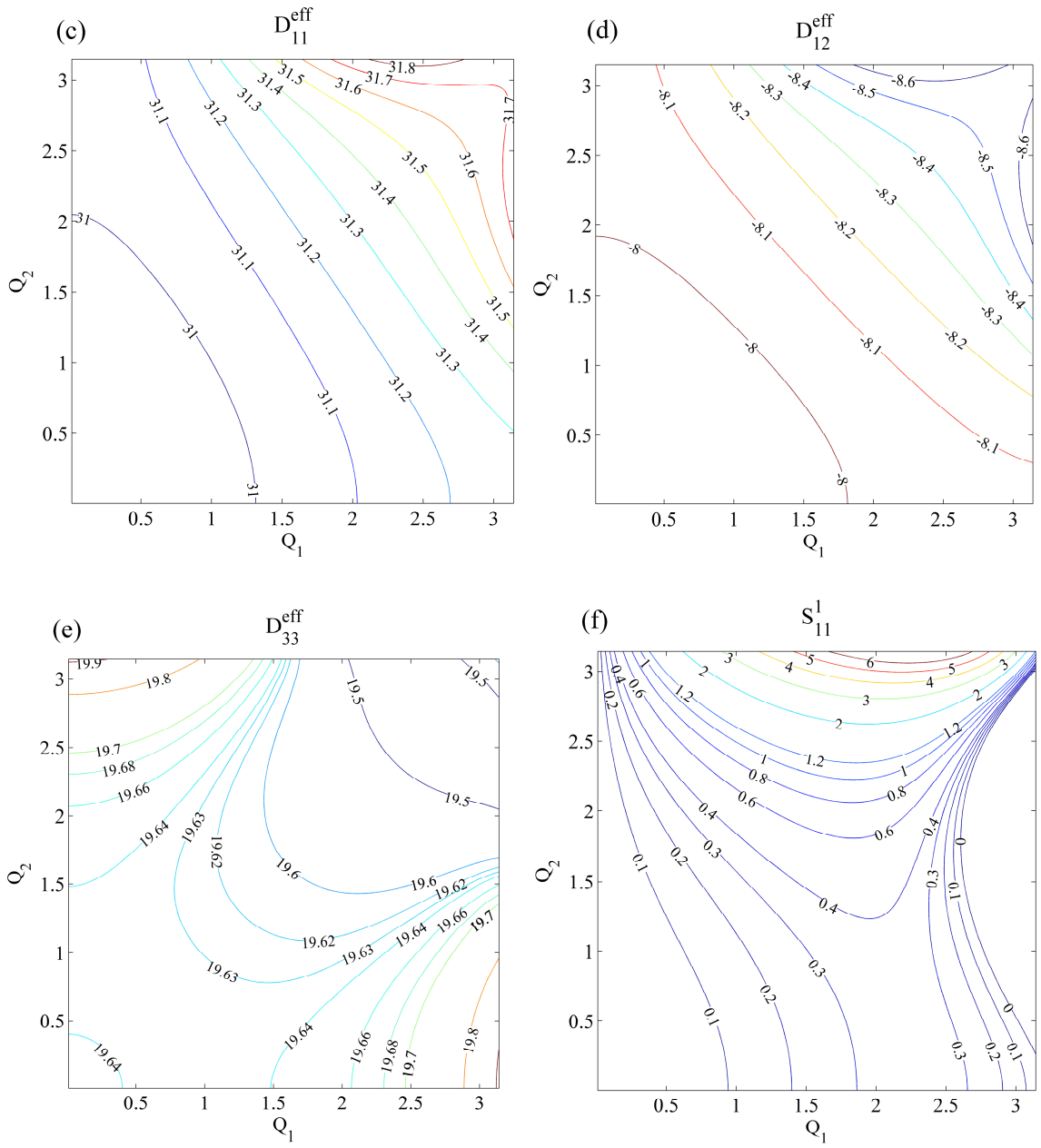

Figure 6-4: Contours of, continued (c) $\overline{D}_{11}$, (d) $\overline{D}_{12}$, (e) $\overline{D}_{33}$, and (f) $\overline{S}_{11}^{1}$ over the acoustic SV-mode for the two-dimensional epoxy/steel PC

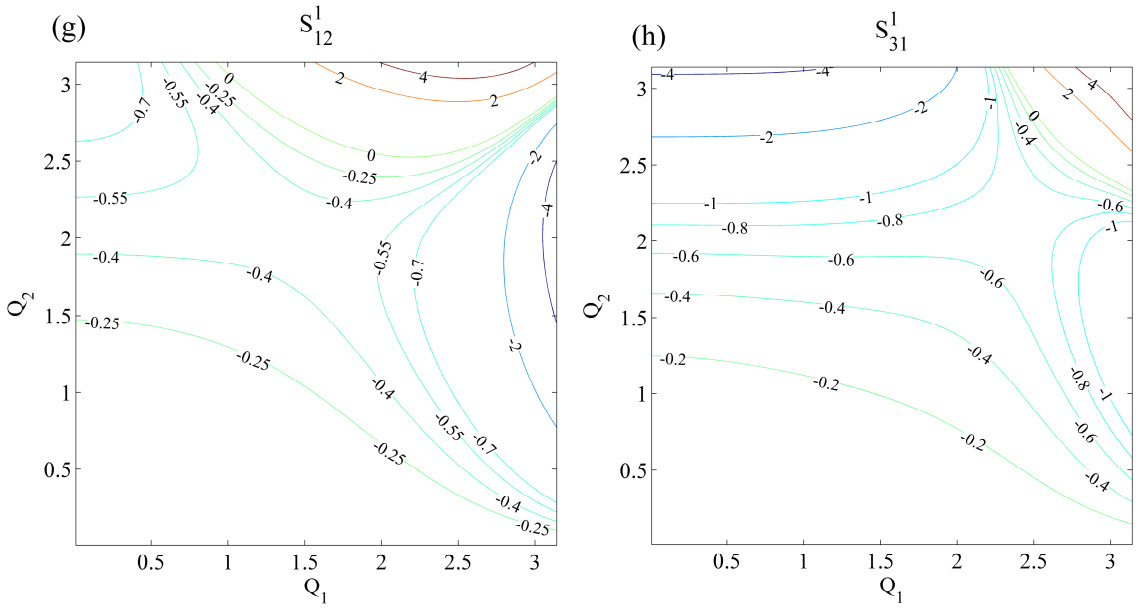

Figure 6-4: Contours of, continued (g) $\bar{S}_{12}^1$ and (h) $\bar{S}_{31}^1$ over the acoustic SV-mode for the two-dimensional epoxy/steel PC

6.4.2. Acoustic longitudinal mode

Figure 6-5 (a) shows the EFS contours of the epoxy/steel PC for the acoustic L-mode together with the corresponding group velocity vectors. It can be seen that depending on the value of (Q_1, Q_2), components of group velocity vectors along the x_1- and x_2-axes can be parallel or antiparallel to those of the phase velocity's. For example, at $\boldsymbol{Q}_A$=(2.307, 2.307) the EFS contour is quasi-circular with anti-parallel phase and group velocities resulting in negative energy refraction. Figure 6-5 (b-h) show the non-zero effective properties of the PC for the acoustic L-mode. In these figures, there are certain regions where the effective properties become singular. For better demonstration of the singularities, values of $\bar{\rho}_{11}$, $\bar{D}_{11}$, and $\bar{S}_{11}^1$ along the Q_1-axis are shown in Figure 6-6 for a fixed value of Q_2= 2.7. In addition, it can be seen that $\bar{\rho}_{11}$ achieves negative values in the

vicinity of the singularity. For example, at $\boldsymbol{Q}$=(1, 2.79) the value of effective density along the x_1-direction becomes $\bar{\rho}_{11} = -3916.9\ kg/m^3$. Furthermore, it is observed that even though the unit cell and inclusions are square and symmetric, the homogenized medium is anisotropic leading to different effective properties along the x_1- and x_2-directions. For example, at $\boldsymbol{Q}$=(2.730, 0) the anisotropy ratio for the effective density is $\bar{\rho}_{11}/\bar{\rho}_{22} = 26.77$. This feature could be used for design of the cloak for acoustic cloaking where unit cells with high anisotropy are essential [43, 44].

Comparing EFS contours with contours of effective properties, it is understood that negative energy refraction can be accompanied by either positive or negative effective properties. For example, at both $\boldsymbol{Q}_B$=(0.214, 2.827) and $\boldsymbol{Q}_C$=(0.513, 2.717), the x_1 component of phase and group velocities are in opposite directions (negative energy refraction). While at $\boldsymbol{Q}_B$ all the effective properties are positive, the effective density at $\boldsymbol{Q}_C$ is negative. Figure 6-7 shows a schematic diagram for negative energy refraction at the interface of a homogenous half-space solid with a two-dimensional PC. In this figure $\boldsymbol{k}_L^{in}$, $\boldsymbol{k}_L^{ref}$, $\boldsymbol{k}_S^{ref}$, $\boldsymbol{v}_L^g$, and $\boldsymbol{v}_L^p$ are vectors of incident longitudinal wave, reflected longitudinal wave, reflected shear wave, transmitted longitudinal group velocity, and transmitted longitudinal phase velocity, respectively. In should be noted that at $\boldsymbol{Q}_A$, $\boldsymbol{Q}_B$, and $\boldsymbol{Q}_C$ the eigenfrequencies are 15.76 kHz, 17.02 kHz, and 16.46 kHz, respectively, which are within the shear wave band-gap regime and therefore no SV-wave can propagate. This feature can be used to focus acoustic/pressure waves in a focal point in order to make flat acoustic lens for applications like ultrasound imaging; or to focus high intensity ultrasound acoustic/pressure waves for cancer treatment.

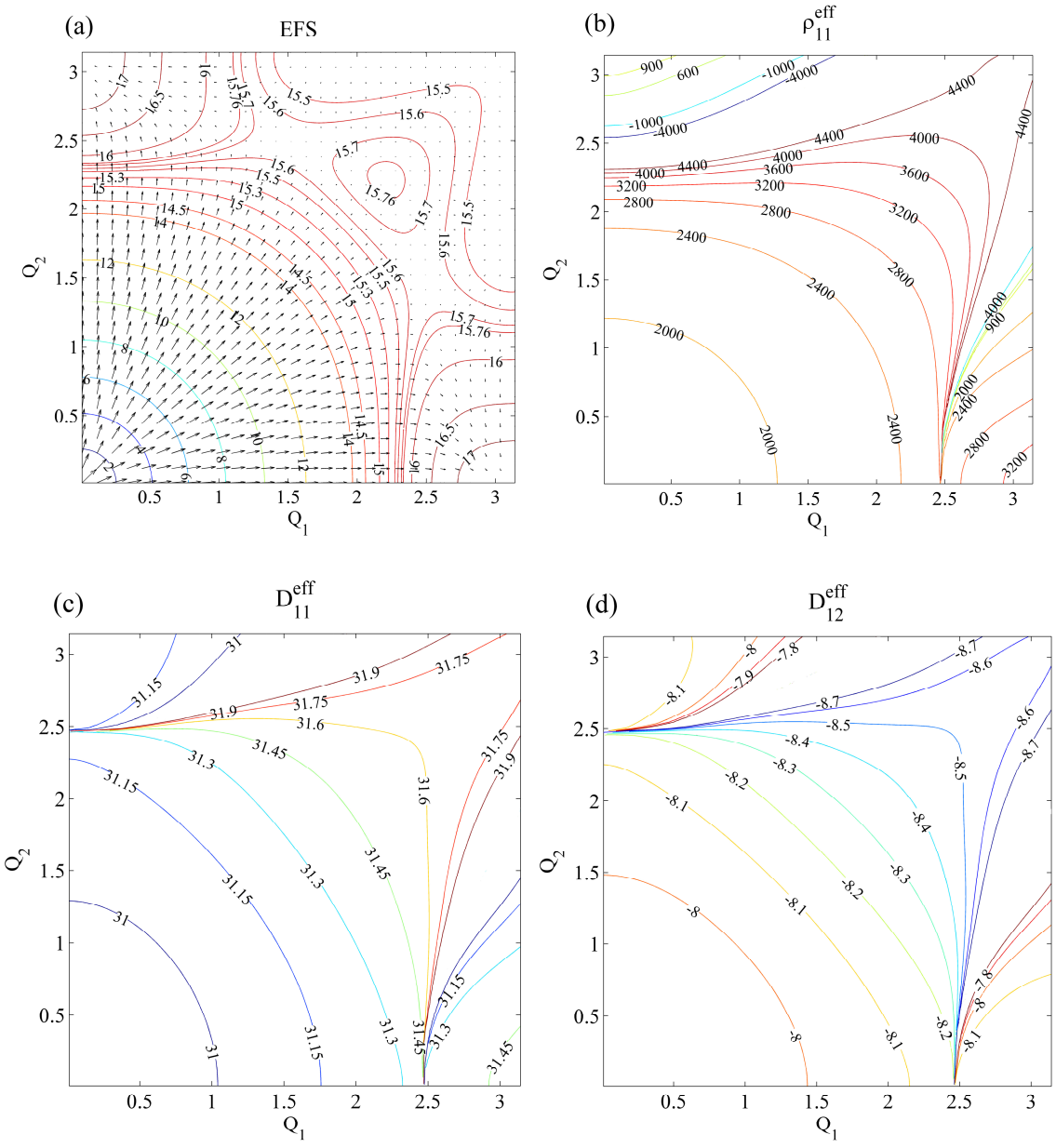

Figure 6-5: Contours of (a) EFS, (b) $\bar{\rho}_{11}$, (c) $\overline{D}_{11}$, and (d) $\overline{D}_{12}$ over acoustic L-mode for the two-dimensional epoxy/steel PC

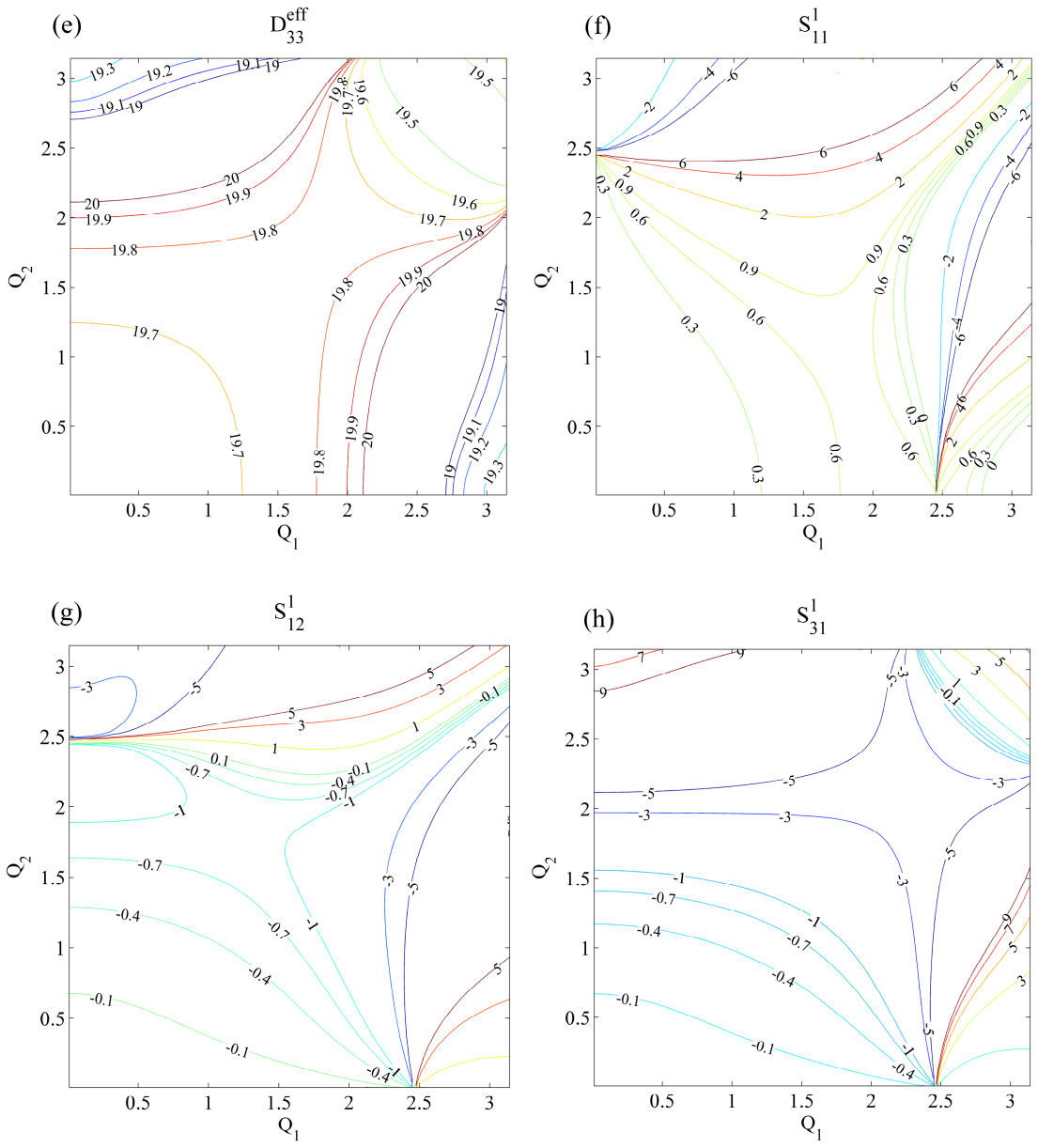

Figure 6-5: Contours of, continued (e) $\bar{D}_{33}$, (f) $\bar{S}_{11}^{1}$, (g) $\bar{S}_{12}^{1}$, and (h) $\bar{S}_{31}^{1}$ over acoustic L-mode for the two-dimensional epoxy/steel PC

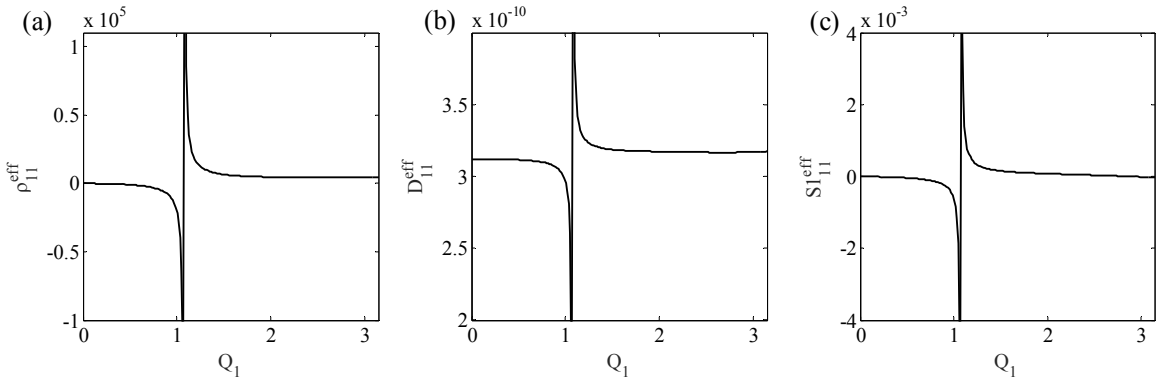

Figure 6-6: Values of (a) $\bar{\rho}_{11}$, (b) $\bar{D}_{11}$, and (c) $\bar{S}^1_{11}$ along the Q_1-axis for a fixed value of Q_2= 2.7 over the acoustic L-mode for the two-dimensional epoxy/steel PC

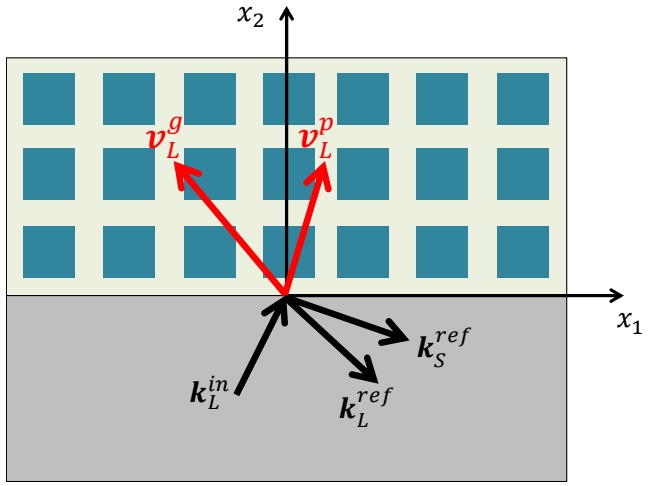

Figure 6-7: Negative refraction at the interface of a homogenous solid and a two-dimensional PC

6.5. Summary

Mixed variational formulation is used together with dynamic homogenization to study elastic wave propagation in two-dimensional PCs. Numerical results for a two-dimensional PC made of epoxy matrix with steel inclusions are presented. It is observed that over the acoustic longitudinal mode components of the effective density and effective compliance tensors can become singular and achieve negative values near the

singularities. In addition, vectors of group velocity are studied and it is observed that negative energy refraction can occur at some frequencies over the acoustic longitudinal mode; which can be accompanied by either positive or negative effective properties. This feature can be used to focus longitudinal stress waves in a focal point in order to make flat acoustic lens for applications like ultrasound imaging. Furthermore, it is observed that the PC exhibits a high anisotropy ratio for the effective density at some frequencies over the acoustic longitudinal mode; which could be used for design of cloak for acoustic cloaking where unit cells with high anisotropy are essential.

References

[1] Z. Liu, X. Zhang, Y. Mao, Y. Zhu, Z. Yang, C. Chan and P. Sheng, "Locally resonant sonic materials," *Science,* vol. 289, no. 5485, pp. 1734-1736, 2000.

[2] J. Li and C. Chan, "Double-negative acoustic metamaterial," *Physical Review E,* vol. 70, no. 5, p. 055602, 2004.

[3] N. Fang, D. Xi, J. Xu, M. Ambati, W. Srituravanich, C. Sun and X. Zhang, "Ultrasonic metamaterials with negative modulus," *Nature materials,* vol. 5, no. 6, pp. 452-456, 2006.

[4] S. Rytov, "Acoustical properties of a thinly laminated medium," *Soviet Physics Acoustics,* vol. 2, pp. 68-80, 1956.

[5] S. Nemat-Nasser, "General variational methods for waves in elastic composites," *Journal of Elasticity,* vol. 2, no. 2, pp. 73-90, 1972.

[6] S. Nemat-Nasser and S. Minagawa, "Harmonic waves in layered composites: comparison among several schemes," *Journal of Applied Mechanics,* vol. 42, p. 699, 1975.

[7] S. Nemat-Nasser and M. Yamada, "Harmonic waves in layered transversely isotropic composites," *Journal of Sound and Vibration,* vol. 79, no. 2, pp. 161-170, 1981.

[8] S. Nemat-Nasser, F. Fu and S. Minagawa, "Harmonic waves in one-, two-and three-dimensional composites: Bounds for eigenfrequencies," *International Journal of Solids and Structures,* vol. 11, no. 5, pp. 617-642, 1975.

[9] S. Minagawa and S. Nemat-Nasser, "Harmonic waves in three-dimensional elastic composites," *International Journal of Solids and Structures,* vol. 12, no. 11, pp. 769-777, 1976.

[10] S. Minagawa, S. Nemat-Nasser and M. Yamada, "Dispersion of waves in two-dimensional layered, fiber-reinforced, and other elastic composites," *Computers & Structures,* vol. 19, no. 1-2, pp. 119-128, 1984.

[11] S. Minagawa, S. Nemat-Nasser and M. Yamada, "Finite element analysis of harmonic waves in layered and fibre-reinforced composites," *International Journal for Numerical Methods in Engineering,* vol. 17, no. 9, pp. 1335-1353, 1981.

[12] M. S. Kushwaha, P. Halevi, L. Dobrzynski and B. Djafari-Rouhani, "Acoustic band structure of periodic elastic composites," *Physical Review Letters,* vol. 71, no. 13, p. 2022, 1993.

[13] M. Kushwaha, P. Halevi, G. Martinez, L. Dobrzynski and B. Djafari-Rouhani, "Theory of acoustic band structure of periodic elastic composites," *Physical Review B,* vol. 49, no. 4, p. 2313, 1994.

[14] J. Vasseur, P. Deymier, G. Frantziskonis, G. Hong, B. Djafari-Rouhani and L. Dobrzynski, "Experimental evidence for the existence of absolute acoustic band gaps in two-dimensional periodic composite media," *Journal of Physics: Condensed Matter,* vol. 10, no. 27, p. 6051, 1998.

[15] J. Mei, Z. Liu, J. Shi and D. Tian, "Theory for elastic wave scattering by a two-dimensional periodical array of cylinders: An ideal approach for band-structure calculations," *Physical Review B,* vol. 67, no. 24, p. 245107, 2003.

[16] M. Kafesaki and E. Economou, "Multiple-scattering theory for three-dimensional periodic acoustic composites," *Physical Review B,* vol. 60, no. 17, p. 11993, 1999.

[17] Z. Liu, C. Chan, P. Sheng, A. Goertzen and J. Page, "Elastic wave scattering by periodic structures of spherical objects: Theory and experiment," *Physical Review B,* vol. 62, no. 4, p. 2446, 2000.

[18] M. Ke, Z. Liu, C. Qiu, W. Wang, J. Shi, W. Wen and P. Sheng, "Negative-refraction imaging with two-dimensional phononic crystals," *Physical Review B,* vol. 72, no. 6, p. 064306, 2005.

[19] D. Torrent, Y. Pennec and B. Djafari-Rouhani, "Resonant and nonlocal properties of phononic metasolids," *Physical Review B,* vol. 92, no. 17, p. 174110, 2015.

[20] V. Fokin, M. Ambati, C. Sun and X. Zhang, "Method for retrieving effective properties of locally resonant acoustic metamaterials," *Physical Review B,* vol. 76, no. 14, p. 144302, 2007.

[21] R. Zhu, X. Liu, G. Hu, C. Sun and G. Huang, "Negative refraction of elastic waves at the deep-subwavelength scale in a single-phase metamaterial," *Nature communications,* vol. 5, p. 1111, 2014.

[22] Y. Xie, B.-I. Popa, L. Zigoneanu and S. A. Cummer, "Measurement of a broadband negative index with space-coiling acoustic metamaterials," *Physical review letters,* vol. 110, no. 17, p. 175501, 2013.

[23] J. Li, Z. Liu and C. Qiu, "Negative refraction imaging of solid acoustic waves by two-dimensional three-component phononic crystal," *Physics Letters A,* vol. 372, no. 21, pp. 3861-3867, 2008.

[24] C. Croenne, E. Manga, B. Morvan, A. Tinel, B. Dubus, J. Vasseur and A. Hladky-Hennion, "Negative refraction of longitudinal waves in a two-dimensional solid-solid phononic crystal," *Physical Review B,* vol. 83, no. 5, p. 054301, 2011.

[25] S. Nemat-Nasser, "Anti-plane shear waves in periodic elastic composites: band structure and anomalous wave refraction," *Proc. R. Soc. A,* vol. 471, no. 20150152, 2015.

[26] S. Nemat-Nasser, "Refraction characteristics of phononic crystals," *Acta Mechanica Sinica,* vol. 31, no. 4, p. 481–493, 2015.

[27] K. M. Ho, C. K. Cheng, Z. Yang, X. Zhang and P. Sheng, "Broadband locally resonant sonic shields," *Applied physics letters,* vol. 83, no. 26, pp. 5566-5568, 2003.

[28] Y. Cheng, J. Xu and X. Liu, "One-dimensional structured ultrasonic metamaterials with simultaneously negative dynamic density and modulus," *Physical Review B,* vol. 77, no. 4, p. 045134, 2008.

[29] G. Wang, D. Yu, J. Wen, Y. Liu and X. Wen, "One-dimensional phononic crystals with locally resonant structures," *Physics Letters A,* vol. 327, no. 5, pp. 512-521, 2004.

[30] S. Nemat-Nasser and A. Srivastava, "Negative effective dynamic mass-density and stiffness: Micro-architecture and phononic transport in periodic composites," *AIP Advances,* vol. 1, p. 041502, 2011.

[31] M. I. Hussein, M. J. Leamy and M. Ruzzene, "Dynamics of phononic materials and structures: Historical origins, recent progress, and future outlook," *Applied Mechanics Reviews,* vol. 66, no. 4, p. 040802, 2014.

[32] A. Srivastava, "Elastic metamaterials and dynamic homogenization: a review," *International Journal of Smart and Nano Materials,* vol. 6, no. 1, pp. 41-60, 2015.

[33] T. Antonakakis, R. Craster and S. Guenneau, "Homogenisation for elastic photonic crystals and dynamic anisotropy," *Journal of the Mechanics and Physics of Solids,*

vol. 71, pp. 84-96, 2014.

[34] L. Joseph and R. Craster, "Reflection from a semi-infinite stack of layers using homogenization," *Wave Motion,* vol. 54, pp. 145-156, 2015.

[35] A. B. Movchan and L. I. Slepyan, "Resonant waves in elastic structured media: dynamic homogenisation versus Green's functions," *International Journal of Solids and Structures,* vol. 51, no. 13, pp. 2254-2260, 2014.

[36] S. Nemat-Nasser and A. Srivastava, "Bounds on effective dynamic properties of elastic composites," *Journal of the Mechanics and Physics of Solids,* vol. 61, no. 1, pp. 254-264, 2013.

[37] A. Wautier and B. B. Guzina, "On the second-order homogenization of wave motion in periodic media and the sound of a chessboard," *Journal of the Mechanics and Physics of Solids,* vol. 78, pp. 382-414, 2015.

[38] J. Willis, "Exact effective relations for dynamics of a laminated body," *Mechanics of Materials,* vol. 41, no. 4, pp. 385-393, 2009.

[39] S. Nemat-Nasser, J. Willis, A. Srivastava and A. Amirkhizi, "Homogenization of periodic elastic composites and locally resonant sonic materials," *Physical Review B,* vol. 83, no. 10, p. 104103, 2011.

[40] S. Nemat-Nasser and A. Srivastava, "Overall dynamic constitutive relations of layered elastic composites," *Journal of the Mechanics and Physics of Solids,* vol. 59, no. 10, pp. 1953-1965, 2011.

[41] A. Srivastava and S. Nemat-Nasser, "Overall dynamic properties of three-dimensional periodic elastic composites," *Proceedings of the Royal Society A: Mathematical, Physical and Engineering Science,* vol. 468, no. 2137, pp. 269-287, 2012.

[42] S. Nemat-Nasser and A. Srivastava, "Negative effective dynamic mass-density and stiffness: Micro-architecture and phononic transport in periodic composites," *AIP Advances,* vol. 1, no. 4, p. 041502, 2011.

[43] G. W. Milton, M. Briane and J. R. Willis, "On cloaking for elasticity and physical equations with a transformation invariant form," *New Journal of Physics,* vol. 8, no. 10, p. 248, 2006.

[44] D. Torrent and J. Sanchez-Dehesa, "Acoustic cloaking in two dimensions: a feasible approach," *New Journal of Physics,* vol. 10, no. 6, p. 063015, 2008.

[45] R. Esquivel-Sirvent and G. Cocoletzi, "Band structure for the propagation of elastic waves in superlattices," *The Journal of the Acoustical Society of America,* vol. 95, p. 86, 1994.

[46] M. Ruzzene and A. M. Baz, "Attenuation and localization of wave propagation in periodic rods using shape memory inserts," in *International Society for Optics and Photonics*, 2000.

[47] C. Goffaux and J. Vigneron, "Theoretical study of a tunable phononic band gap system," *Physical Review B,* vol. 64, no. 7, p. 075118, 2001.

[48] X.-Y. Zou, Q. Chen, B. Liang and J.-C. Cheng, "Control of the elastic wave bandgaps in two-dimensional piezoelectric periodic structures," *Smart Materials and Structures,* vol. 17, no. 1, p. 015008, 2008.

[49] L.-Y. Wu, M.-L. Wu and L.-W. Chen, "The narrow pass band filter of tunable 1D phononic crystals with a dielectric elastomer layer," *Smart Materials and Structures,* vol. 18, no. 1, p. 015011, 2009.

[50] X.-Y. Zou, S.-Z. Xu, B. Liang and J.-C. Cheng, "Modulation of the bandgaps of in-plane elastic waves by out-of-plane wavenumber in the piezoelectric composite structures," *Smart Materials and Structures,* vol. 20, no. 3, p. 035009, 2011.

[51] A. V. Amirkhizi and S. Nemat-Nasser, "Experimental verification of stree-wave bands and negative phase velocity in layered media," *Theoretical Applied Mechanics,* vol. 38, no. 4, pp. 299-319, 2011.

[52] J. Qiao, A. V. Amirkhizi, K. Schaaf and S. Nemat-Nasser, "Dynamic mechanical analysis of fly ash filled polyurea elastomer," *Mechanics of Materials,* vol. 43, no. 10, pp. 598-607, 2011.

[53] C. Desilets, J. Fraser and G. Kino, "The design of efficient broad-band piezoelectric transducers," *Sonics and Ultrasonics, IEEE Transactions on,* vol. 25, no. 3, pp. 115-125, 1978.

[54] R. Gerlach, O. Kraus, J. Fricke, P. Eccardt, N. Kroemer and V. Magori, "Modified SiO2 aerogels as acoustic impedance matching layers in ultrasonic devices," *Journal of non-crystalline solids,* vol. 145, pp. 227-232, 1992.

[55] M. Haller and B. Khuri-Yakub, "Tapered acoustic matching layers," in *Ultrasonics Symposium*, 1993.

[56] D. Wu, P. Harris and R. Young, "A taper microstructure for impedance matching,"

in *Ultrasonics Symposium*, 2010.

[57] A. Dawson, G. Gouws, P. Harris and R. Young, "Acoustic impedance matching with porous aluminium," in *IEEE Sensors*, 2009.

[58] M. I. Hussein, K. Hamza, G. M. Hulbert, R. A. Scott and K. Saitou, "Multiobjective evolutionary optimization of periodic layered materials for desired wave dispersion characteristics," *Structural and Multidisciplinary Optimization,* vol. 31, no. 1, pp. 60-75, 2006.

[59] H. Meng, J. Wen, H. Zhao and X. Wen, "Optimization of locally resonant acoustic metamaterials on underwater sound absorption characteristics," *Journal of Sound and Vibration,* vol. 331, no. 20, pp. 4406-4416, 2012.

[60] W. Wang and T. Yang, "Multi-Objective Optimization of Layered Elastic Metamaterials With Multiphase Microstructures," *Journal of Vibration and Acoustics,* vol. 135, no. 4, p. 041010, 2013.

[61] S. Zhuang, G. Ravichandran and D. E. Grady, "An experimental investigation of shock wave propagation in periodically layered composites," *Journal of the Mechanics and Physics of Solids,* vol. 51, no. 2, pp. 245-265, 2003.

[62] X. Chen and N. Chandra, "The effect of heterogeneity on plane wave propagation through layered composites," *Composites science and technology,* vol. 64, no. 10, pp. 1477-1493, 2004.

[63] X. Luo, A. J. Aref and G. F. Dargush, "Analysis and optimal design of layered structures subjected to impulsive loading," *Computers & Structures,* vol. 87, no. 9, pp. 543-551, 2009.

[64] B. Schimizze, S. F. Son, R. Goel, A. P. Vechart and L. Young, "An experimental and numerical study of blast induced shock wave mitigation in sandwich structures," *Applied Acoustics,* vol. 74, no. 1, pp. 1-9, 2013.

[65] D. G. Luenberger, Introduction to linear and nonlinear programming, vol. 28, Addison-Wesley Reading, MA, 1973.

[66] R. L. Haupt and S. E. Haupt, Practical genetic algorithms, John Wiley & Sons, 2004.

[67] S. Nemat-Nasser, J. B. Isaacs and J. E. Starrett, "Hopkinson techniques for dynamic recovery experiments," *Proceedings of the Royal Society of London. Series A: Mathematical and Physical Sciences,* vol. 435, no. 1894, pp. 371-391, 1991.

[68] S. Yang, J. Page, Z. Liu, M. Cowan, C. Chan and P. Sheng, "Focusing of sound in a 3D phononic crystal," *Physical review letters,* vol. 93, no. 2, p. 24301, 2004.